1323

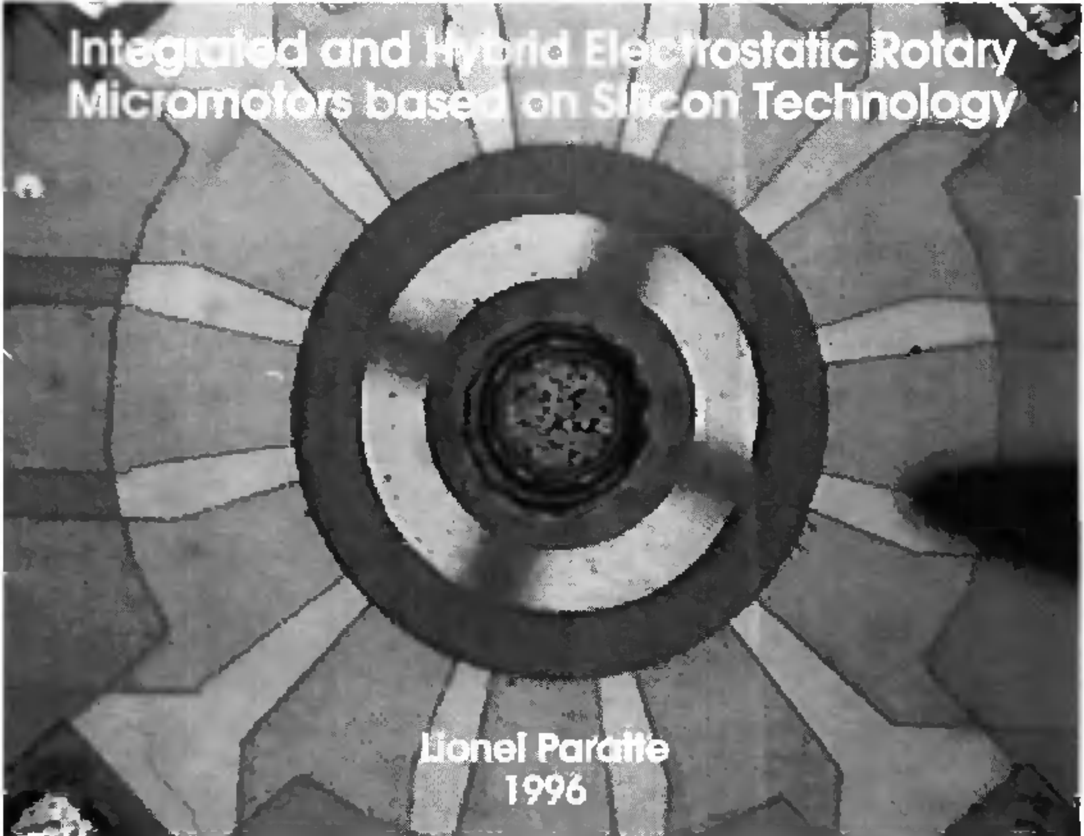

Integrated and Hybrid Electrostatic Rotary Micromotors based on Silicon Technology

Philosophical Dissertation

submitted to the Faculty of Sciences of the University of Neuchâtel
to obtain the degree of Doctor of Sciences

by

Lionel Paratte
Dipl. Eng. Microtechnology EPFL

Institute of Microtechnology
University of Neuchâtel
Rue A.-L. Breguet 2
2000 Neuchâtel
Switzerland

© Copyright 1996 Lionel Paratte

printed by Imprimerie Roger Geiser S.A.
CH - 2013 Colombier (NE)

To my wife Nathalie,
for her love, encouragement and help.

To my parents Ingrid and François, and to my brother Ronald,
for their love and support.

IMPRIMATUR POUR LA THÈSE

Integrated and hybrid electrostatic rotary micromotors
based on silicon technology

de M. Lionel Paratte

UNIVERSITÉ DE NEUCHÂTEL

FACULTÉ DES SCIENCES

La Faculté des sciences de l'Université de
Neuchâtel sur le rapport des membres du jury,

Messieurs N.F. de Rooij, H. Hügli, E. Bornand,
et L.S. Fan, (Almaden, USA)

autorise l'impression de la présente thèse.

Neuchâtel, le 17 avril 1996

Le doyen:

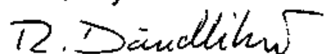

R. Dändliker

Abstract

The subject of this thesis is the design, fabrication and characterization of rotary electrostatic micromotors on silicon. Scaled homothetically down from tens of millimeters to hundreds of micrometers, electrostatic motors are theoretically more effective than their magnetic equivalents. They will fit emerging applications demanding high mechanical positioning precision, such as in microbiology, microelectromechanical displays, computer micro disc drives, and much more. Their fabrication become even more feasible and attractive by using *micromachining*, the techniques used for the mass production of silicon integrated circuits. Aside from the above cited applications, here the driving motto was wristwatch applications, where mechanical power in the order of 1 μW is required to drive the hands.

Wobble (or harmonic) electrostatic micromotors have been studied and patented. The rotor wobbles vertically exactly like a coin flipped on a table, and the rapid wobbling induces a much slower, reduced rotation of the rotor (output). The electrostatic generated friction forces, a major hindrance in direct drive motors, contribute directly in the wobble motors to the output torque.

Integrated direct-drive stepper and wobble motors have been analytically modelled, and fabricated using silicon surface micromachining. The rotors were typically 200 μm in diameter and 1 μm thick. Dry friction coefficients between thin films likely to be used in the construction have been measured. Hybrid wobble millimotors were fabricated using silicon surface micromachining for the stator and the rotor and fine mechanics for the axle. Tailored to deliver the power needed by wristwatches, their rotors were 2 mm in diameter and 10 μm thick, and were realized by electroplating of nickel in a photoresist mould. A flexible rotor version has been directly mounted onto a miniature gear train, realized by fine mechanics.

The integrated motors could be rotated mechanically, but not electrically, because of bearing jamming, which is an easily solvable problem. The hybrid wobble millimotors rotated successfully, with the following typical performances: excitation 80 V, speed 0 to 10 rpm (proportional to exc. frequency), average motive torque 0.2 μNm, operation time without interruption 2 days (limited by rotor-stator isolation chargeup), and still unknown mean time to failure (minimum 1 month). The power can be increased by improving the excitation scheme. The flexible rotor motor demonstrated for the first time the capability for electrostatic micromotors to drive mechanical loads.

These encouraging results make this work to a starter for practical electrostatic rotary microdrives, where -in addition- the driving circuit and the motor can be at least regrouped, at best integrated on a single chip.

Résumé

Le sujet de cette thèse est la conception, la fabrication et la caractérisation de micromoteurs électrostatiques sur silicium. Lors d'une réduction homothétique de quelques dizaines de millimètres vers quelques centaines de micromètres, les moteurs électrostatiques ont théoriquement un meilleur rendement que leurs équivalents magnétiques. Destinés à des applications émergentes de haute précision, t.q. microbiologie, affichages micro-électromécaniques, microdisques d' ordinateur, etc. Leur fabrication devient séduisante par l'utilisation du *micro-usinage*, soit les techniques de production des circuits intégrés sur silicium. La motivation est axée ici sur la montre-bracelet, où une puissance mécanique de quelque 1 μW est nécessaire à l'entraînement des aiguilles.

Des moteurs électrostatiques oscillants (ou harmoniques) ont été étudiés et brevetés. Leur rotor oscille verticalement comme une pièce de monnaie lancée sur un plan. Ce mouvement rapide induit une rotation lente du rotor, utilisée pour l'entraînement.

Des micromoteurs électrostatiques intégrés pas-à-pas et oscillants ont été modélisés analytiquement, puis fabriqués par micro-usinage. Leurs rotors ont 200 micromètres de diamètre par 1 micromètre d'épaisseur. Les coefficients de frottement sec entre couches minces envisagées pour leur fabrication ont été mesurés. Des moteurs oscillants hybrides millimétriques ont été réalisés. Leurs rotors et stators ont été fabriqués par usinage de surface du silicium, et l' axe par mécanique fine. Dimensionnés pour délivrer la puissance demandée d'une montre-bracelet, leurs rotors de 2 millimètres de diamètre et 10 micromètre d'épaisseur ont été réalisés par croissance galvanique de nickel dans un moule de résine photosensible. Un tel rotor, flexible, a été monté sur un train d'engrenages miniature réalisé par mécanique fine.

Les micromoteurs intégrés ont été mus en rotation mécaniquement, mais non électriquement en raison d'un blocage du palier, problème facilement soluble. Les millimoteurs hybrides ont les caractéristiques typiques suivantes: excitation 80 V, vitesse de 0 à 10 t/min (proportionnelle à la fréquence d'exc.), couple utile moyen 0.2 μNm, temps de fonctionnement sans interruption 2 jours (limité par chargement d'isolant rotor-stator), et durée de vie encore inconnu (minimum 1 mois). La puissance peut être augmentée par amélioration de la commutation. Le moteur à rotor flexible a démontré, pour la première fois, qu'il est possible d'entraîner une charge mécanique avec des micromoteurs électrostatiques.

Ces résultats encourageants font de cette étude un démarrage pour des micro-entraînements électrostatiques pratiques, de plus pour lesquels le circuit de contrôle et le moteur peuvent être regroupés, et au mieux intégrés sur une même puce.

Notations

Symbol	Description	Unit
α	tilt angle (WM)	rad
β, β_o	rotor-stator overlap angle, at zero net torque (SM)	rad
γ	contact point position w.r.t. electrode center (WM)	rad
δ	rotor output position around z (WM)	rad
ΔT	temperature difference between motor and ambient	°C
ε_0	permittivity in vacuum: 8.86 x 10^{-12}	As/Vm
ε_r	dielectric constant	1
η	viscosity	kg/ms
θ	rotor, stator tooth width	rad
Θ	magnetic potential	A
μ_0	permeability in vacuum: 1.256 x 10^{-6}	Vs/Am
μ_r	relative permeability	1
$\mu_{s,d}$	dry static, dynamic friction coefficient	1
$\mu_{bu,bc}$	dry dynamic bushings, bearing friction coefficient	1
ν	Poisson's coefficient	1
ρ	specific mass	kg/m^3
ρ_{el}	electrical resistivity	Ωm
φ	rotor position around z (SM)	rad
φ	rotor position around y' (WM)	rad
φ_0	zero net torque position around z (SM)	rad
Φ	magnetic flux	Vs
χ	convection coefficient	W/mK
ω	speed around the rocking axis y' (WM)	rad/s
ω_0	oscillation frequency (WM)	rad/s
ω_z	output speed around the z axis (WM)	rad/s
$\omega_{z\ av}$	average output speed (WM)	rad/s
$\omega_{z\ av\ max}$	maximum average output speed before cutoff (WM)	rad/s
Ω	contact point speed (WM)	rad/s

A	rotor-stator overlap area	m^2
A_e	cross-sectional area of coil wire	m^2
A_χ	convection area	m^2
b	torsion bar width (WM)	m
B, B_g	magnetic induction field, in the gap	T
c	voltage correction factor (WM)	1
c_{es}	voltage - normalized electrostatic spring stiffness	$Nm/radV^2$
C	total capacitance	farad
C_1, C_2	air gap variable capacitances, rotor-stator pair (SM)	farad
C_i	dielectric or isolation capacitance	farad
C_a	air gap capacitance	farad
d	air gap length	m
E	electrostatic field	V/m
E_y	Young's modulus	N/m^2
f	viscous damping coefficient (WM)	Nms
$F_{1,2}$	rotor side-pull forces (side-drive SM)	N
F_f	friction force	N
F_z	rotor pull-down force	N
G	modulus of rigidity	N/m^2
h	harmonic reduction ratio (WM)	1
I	current	A
I, $I_{y'}$, I_z	inertia, around y', around z (WM)	$kg\ m^2$
J	current density	A/m^2
k_{to}	torque multiplication factor (WM)	1
k_{sp}	torsion spring constant of one torsion bar (WM)	Nm/rad
K	torsion form factor (WM)	m^4
l_f	flow limit length	m
l	torsion bar length (WM)	m
l_{be}	lateral bearing clearance	m
l_m	ferromagnetic path length	m
m	rotor mass	kg
$M_{ax'}$	electrostatic adherence torque around the tilting axis x' (WM)	Nm
M_{az}	electrostatic adherence torque around the z axis (WM)	Nm
$M_{dy'}$	air drag torque around the rocking axis y' (WM)	Nm
M_f	electrostatic dry dynamic friction torque (SM)	Nm
M_m	electrostatic drive torque around z (SM)	Nm
$M_{my'}$	electrostatic motive torque around the rocking axis y' (WM)	Nm

M_{mz}	electrostatic motive torque around the z axis (WM)	Nm
M_n	electrostatic net torque (M_m-M_f)	Nm
$M_{sx'}$	spring torque of flexible gimbals rotor around tilt axis (WM)	Nm
M_{zav}	average motor electrostatic torque (WM)	Nm
N	normal (load) force	N
N_R	Reynolds's number	1
n	number of coil turns	1
n_g	number of air gaps per sector (comb drive SM)	1
n_s	number of stator electrodes	1
p	pressure	N/m^2
r	radial gap-to-gap pitch (comb-drive SM)	m
r_c	gas concentration ratio	1
R	rotor outer radius	m
R_s	rolling path radius (WM)	m
$R_{bu,be}$	bushings, resp. bearing radii	m
R_i	stator electrodes inner radius	m
$R_{mg,mm}$	magnetic reluctance of air gap, of ferromagnetic path	A/Vs
t	rotor thickness	m
T	kinetic energy	J
$T_{att,osc}$	period of attenuation, of oscillation	s
T_{mec}	mechanical step response time (WM)	s
T_{exc}	one step excitation period	s
U	potential energy	J
$u_{em,es,hp}$	specific electromagnetic, electrostatic, hydropneumatic energy	J/m^3
v	linear speed	m/s
V	excitation voltage	V
V	volume	m^3
V_{br}	breakdown voltage	V
W_{mec}	mechanical power	W
x,y,z	orthogonal coordinate axes attached to the stator	m
x',y',z'	orthogonal coordinate axes attached to the rotor (WM)	m
y', z'	rocking, tilting axis (WM)	m

Abbreviations:

AFM	atomic force microscope / microscopy
AP	atmospheric pressure
CCW	counter clockwise (rotation)
CVD	chemical vapor deposition
CW	clockwise (rotation)
GP	ground plane
IC	integrated circuit
LPCVD	low pressure chemical vapor deposition
LTO	low temperature oxide
PSG	phospho silicate glass (phosphorous-doped silicon dioxide)
RH	relative humidity
S.D.	standard deviation
SEM	scanning electron microscope / microscopy
SM	(synchronous) stepper motor
STM	scanning tunneling microscope / microscopy
TEM	transmission electron microscope / microscopy
VC	variable capacitance
VR	variable reluctance
WM	(harmonic) wobble motor
w.r.t.	with respect to
wt%	weight percent

Collaborating organizations:

Asulab S.A.	R&D Laboratories of SMH (Société de Microéléctronique et d'Horlogerie)
CSEM S.A.	Centre Suisse d'Electronique et de Microtechnique
EPFL	Ecole Polytechnique Fédérale de Lausanne Swiss Federal Institute of Technology, Lausanne (Switzerland)

Granting organizations:

CERS	Comité pour l'Encouragement de la Recherche Scientifique Committee for the Promotion of Applied Scientific Research (Switzerland)
M^2S^2	Groupement de laboratoires pour la micromécanique sur Silicium en Suisse Swiss Partnership for Micromechanics on Silicon

Contents

1. Introduction 1

1.1 A brief history of electrostatic motors 1
1.2 Smaller, why ? 2
1.3 Silicon micromachining 3
1.4 Outline of the thesis 6

2. Modelling 7

2.1 Scaling laws for rotary motors 7

2.1.1 Basic theory 7
2.1.2 Compared performances of electromagnetic and electrostatic drives 12

2.2 Integrated polysilicon variable-capacitance synchronous micromotors 16

2.2.1 Principle 16
2.2.2 Process-induced design considerations 17
2.2.3 The side-drive motor 19
2.2.4 The top-drive motor 21
2.2.5 Static performances of side- and top-drive motors 24
2.2.6 The comb-drive motor 26

2.3 Variable-capacitance top-drive wobble motors 29

2.3.1 Introduction 29
2.3.2 Principle (patented) 30
2.3.3 Kinematics 31
2.3.4 Torques 34
2.3.5 Dynamics 36
2.3.6 Calculated performances 40
2.3.7 Flexible gimbals rotor 42

3. Friction 45

3.1 Introduction 45
3.2 Friction conditions of the polysilicon motors 46
3.3 Measurement set-up 46
3.4 Test samples preparation 48
3.5 Results 50
3.6 Interpretation 52
3.7 Conclusions 54

4. Fabrication 55

4.1 Integrated polysilicon motors 55

4.1.1 Process 55
4.1.2 Low-stress silicon nitride 63
4.1.3 Planarization of PSG 64
4.1.4 Silicon whiskers 70
4.1.5 Bearing 71
4.1.6 Release etching 73

4.2 Hybrid electroplated wobble motors 75

4.2.1 General 75
4.2.2 Rigid rotor motor 76
4.2.3 Flexible rotor motor coupled to a gear train 76
4.2.4 Process 79
4.2.5 Electroplating mould 81

5. Testing 85

5.1 Drive electronics 85

5.1.1 Description 85
5.1 2 Determining parameters for the output drivers 87
5.1.3 Comments on efficiency 90

5.2 Test set-up 91

5.3 Integrated polysilicon motors 92

5.3.1 Samples preparation 92
5.3.2 Breakdown voltages of the devices 92
5.3.3 Electrical actuation of side-, top- and comb-drive motors 93
5.3.4 Discussion on the bearing function 96
5.3.5 Levitation effects in side-drive motors 97
5.3.6 Electrical actuation of top-drive wobble motors 98

5.4 Hybrid electroplated, rigid rotor wobble motors 100

5.4.1 Test samples and parameters 100
5.4.2 General observations 100
5.4.3 RC charging of the insulator 102
5.4.4 Wear 103
5.4.5 Speed measurements 105

5. Testing (continued)

5.4.6 Torque measurement by spring deformation 106
5.4.7 Torque measurement by optical detection and parameter extraction 107

5.5 Hybrid electroplated, flexible rotor wobble motor coupled to a gear train 112

5.5.1 Test sample and parameters 112
5.5.2 Tests without lubrication 112
5.5.3 Tests with lubrication 113
5.5.4 Rotor electromechanical static displacement measurements 114
5.5.5 Discussion 115

6. Conclusions **116**

6.1 Motivations 116
6.2 Scaling laws 116
6.3 Modelling 117
6.4 Friction 118
6.5 Fabrication 119
6.6 Testing 119
6.7 Final words 120

References 122

Acknowledgments **127**

Biography **129**

Chapter 1 - Introduction

1.1 A brief history of electrostatic motors

Today, numerous applications in the public and industrial domains use electric actuation, i.e. the conversion from electric energy into mechanical work. Most of these electric motors are electromagnetically driven. Applications are quasi infinite, ranging from millimeter (wristwatch stepper motor) to meter (railway locomotives engine). Inbetween, we find electric motors in toys, robots, automobiles, biomedical devices, mechanical displays (non-exhaustive list).

Since the needs for these products are increasing, their operating principle, power consumption, fabrication techniques and materials are continuously optimized. Sometimes this research efforts for new principles and materials lead, in turn, to machines for which no real needs exist yet. And then, most of the time, the application is also found once this device works, because it just fits -or fits better- to one specific application.

Electrostatic forces have been first experimented by Benjamin Franklin (1706-1790). Charles Augustin de Coulomb (1736-1806) wrote later that two with opposite sign electrically charged bodies attract each other with a force proportional to the charges product divided by the square of the distance between them. Further, these forces could be expressed by the use of the concept of the electrostatic field. The forces are found by derivation of the field potential electrostatic energy w.r.t. spatial position (J.-L. Lagrange, 1736-1813).

The first electrostatic motors were constructed by Franklin and needed quite high voltages [jef], because of the still "large" rotor-stator air gaps achievable with the available technology. Therefore, further development of electrostatic motors in the 19th century consisted mainly in demonstration machines. Practical applications of electromechanical conversion turned towards the use of magnetic fields, because these offered much more acceptable air gap lengths and excitation voltages, for centimeter- to meter-sized machines. Only electrostatic *generators* (Van de Graaff) were developed further in the 20th century for very high-voltage specific applications, such as breakdown studies or particles acceleration.

In 1889, Paschen [pas] established that smaller air gaps (~0.1 mm) sustain increasingly higher electric fields. In other words, electrostatic actuators with submillimeter gaps could be powered with lower voltages than the previous prototypes. As will be shown in the modelling chapter, when motors are scaled down, electrostatic forces also become competitive with electromagnetic because the heat generated at the coils of magnetic machines is increasingly

significant. Still, the incapability to fabricate micrometer-precise gaps and guidances (bearings) left the path free for the on-going development of magnetic actuators. Already well-established in power conversion applications, these entered more and more the information techniques (printers, disk drives, etc.).

It is the coming of VLSI technology for ICs (Integrated Circuits) around 1970 which permitted to envision much finer machining than ever. Micro image printing techniques such as photolithography, electron beam, laser beam, etc. allowed sub-micrometer precision machining of micrometer-sized features. This event was awaited and "has produced a far-reaching technological revolution" [haz]. Novel, IC-inspired techniques, grouped under the generic name of *micromachining* appeared to be just promising for building in particular electrostatic motors with micron-sized air gaps. Pioneers [mul, fan, how, bar1, meh1, lin1] have already made large steps in this direction.

To summarize, the realization of practical electrostatic micromotors is possible through the combination of an early discovered law, the Paschen's law, and a recent technology, the micromachining of silicon.

1.2 Smaller, why ?

"...if the word processor I am using were made of vacuum tubes, it would fill my office instead of a corner of my desk...".

This sentence from Trimmer [tri2] shows one among numerous benefits of the miniaturization of electronic components. The first vacuum tubes computer (ENIAC, 1944) consumed 150'000 W of power for 10'000 operations per second (OOPS), whereas today's portable PC's consume about 10 W and can perform 50'000'000 OPS (source: CSEM). The constant downscaling of electrical signal processing devices has changed, and is still changing our lives. Miniaturization of IC's is advantageous because power consumption and construction material volume are reduced. Another significant advantage of IC miniaturization is the reduction of the signal propagation time, allowing computers to accomplish faster more complex tasks.

Apart of being a technological challenge, why should *micromechanisms* be developed? For example, it is worth citing here again Trimmer [tri2]:

"A system on which I collaborated used a meter-sized robot to handle millimeter-sized chips with an accuracy of about ten microns. This macro system had several disadvantages. The forces needed to move the robot's mass were much larger than the forces that would destroy the chip. (...) Temperature changes of the macro robot were also troublesome. A one degree change of temperature led to about 10 microns expansion, the total error budget of our task. The larger robot spent also most of the time moving the chip from one work station to

another. Because of the size of the robot and associated equipment, these work stations had to be several feet apart. (...) Finally, finding space for this robot and its four by six foot table in a clean room was difficult. This thousand-to-one difference between the size of the macro robot and the chips is equivalent to using a bulldozer to move sugar cubes. The corresponding accuracy requirement is equivalent to positioning the sugar cube to within a hair's width."

The same author then cites the evident advantages of "a one centimeter robot" which could do the same task. The ant of Fig. 1.1 carrying a leaf somewhat exemplifies the mechanical possibilities aimed by this robots' task.

Fig. 1.1 Ant a few millimeters long carrying a load equal or higher than its own weight (source: Muséum d'Histoire Naturelle, Neuchâtel, CH).

Other fields of application include medicine and space exploration. In the former, invasive therapy and surgery with help of microscale tools is more and more replacing operations where usually a big opening of the patient's body was needed. In the latter, the lower mass of a space equipment using micro scale systems is the interesting parameter. A good example is a space miniature bioreactor, in which the growth of living cells (Yeast) in weightlessness is monitored. The complete instrument, comprising microsensors (pH, temperature), silicon micro -pumps and -valves is fitted in a standard container as small as $63 \times 63 \times 85$ mm^3 [arq]. Manipulation of micrometer to millimeter - sized objects also receives a growing interest in the domains of biology (study of living cells and microorganisms) and pharmaceutics (medication synthesis).

In brief, the miniaturization of mechanical actuators is not only a gain in power consumption but permits a better size and mass adaptation to the actuated load.

1.3 Silicon micromachining

The fabrication of micromechanical devices (such as micromotors) is possible with already numerous micromachining techniques which list is too long to be exposed here. Only

some of the basic ones developed further in the present work are given hereafter to exemplify and introduce the concept of micromachining.

The idea of using silicon processing techniques to manufacture micromechanical components is not so new. In 1967, Nathanson et al. realized a resonant gate transistor [nat], illustrated in Fig. 1.2, the gate of which was a 430 µm long metal cantilever beam. The beam could be moved up and down by electrostatic excitation of underlying electrodes ("input force plate").

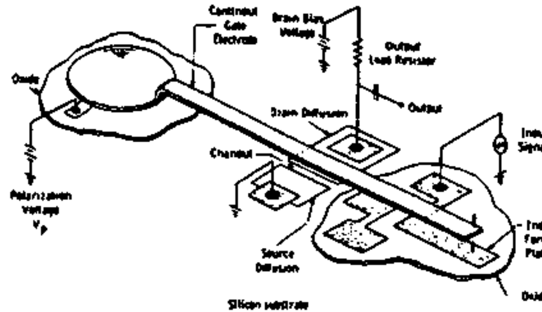

Fig. 1.2 The resonant gate transistor of Nathanson et al. [nat].

The novelty of this device was that a mechanical, protruding element - the beam - was created using photolithography and selective removal of a sacrificial layer between beam and substrate, instead of being *assembled*. The basic process steps for the realization of such a cantilever microbeam, with polysilicon in place of the metal, are depicted in Fig. 1.3 [lin1].

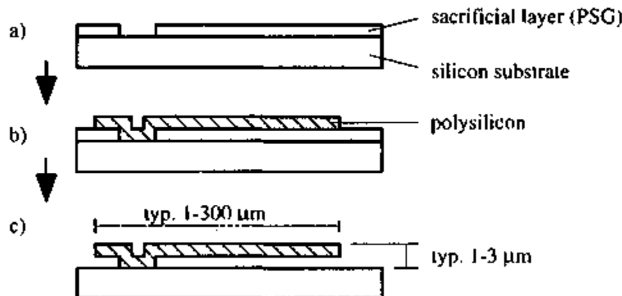

Fig. 1.3 Basic surface micromachining process sequence, in the case of a simply supported polysilicon thin-film microbeam. a) Sacrificial layer (PSG) deposition and patterning, b) structure deposition (Poly) and patterning, and c) release by removal of the sacrificial layer.

First, a heavily phosphorous-doped silicon dioxide layer (Phosphosilicate Glass, PSG) is deposited on the substrate, generally monocrystalline silicon. This is the sacrificial layer. The opening for the attachment of the beam to the substrate is then defined by photolithography, and wet-etched (Fig. 1.3 a). A polysilicon layer is then deposited and patterned to form the beam, using photolithography and wet or dry etching (Fig. 1.3 b). Finally, the sacrificial layer is removed by selective wet etching, leaving the beam free (Fig.

1.3 c). The sacrificial layer technique can be extended for the realization of integrated micro-rotors as will be shown in sect. 2.2.2.

Another method for the realization of integrated or separate micro parts is based on metal electroplating techniques. Electroplating was first used for the fabrication of thick (several tens of micrometer) gold bumps on IC bond pads to adjust to the height level of the DIP case bonding areas. Fig. 1.4 illustrates the general steps of such a process, with only small deviances from the works of many groups [bre, fra, dan, eng, beu, gob,...]. First, a sacrificial layer is deposited, followed by the deposition of the seed layer (1.4 a). Then, a thick resist is spun and patterned using X-ray [bre, guc3] or UV [eng, beu] to form a mould (polymer) in which a metal is electroplated (Fig. 1.4 b). The formed metal part can be released from the substrate by dissolution of the sacrificial layer (Fig. 1.4 c). The incorporation of supplementary steps and layers permits the realization of more complex structures with optional attachment to the substrate.

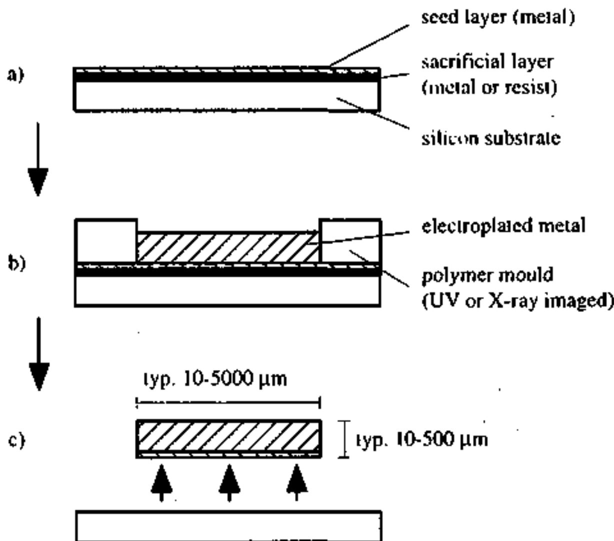

Fig. 1.4 Basic electroplating process sequence, as used for the realization of three-dimensional microparts. a) Seed and sacrificial layer deposition, b) deposition and patterning of the mould (polymer), and electroplating, and c) release by removal of the sacrificial layer.

Hence, submicron-precise machining, even of 3D-structures, issued from IC technology can be exploited to manufacture mechanisms some hundred of microns in size. On the other hand, fine machining (milling, turning, etc.) is currently used for the realization of centimeter-sized mechanisms, with a typical precision of 0.01 mm. Consequently, micromachining allows to push the size down from fine machining limits by two orders of magnitude. This last statement opens large unexplored areas of micromechanics, in particular that electrostatic motors become practical.

1.4 Outline of the thesis

Chapter 2 is dedicated to the design and modelling of electrostatic variable capacitance (VC) micromotors based on silicon. Electrostatic and electromagnetic drive torques are calculated for a homothetic machine, the air gaps being powered either by electric or by magnetic fields. Scaling laws for both principles are proposed. Downscaling of this model shows that microscale electrostatic motors are advantageous in terms of torque and space occupation (sect. 2.1). Polysilicon-based integrated micromotor designs are proposed and evaluated numerically (sect. 2.2). Novel variable capacitance, top-drive wobble motors realizable both in polysilicon and electroplated metals are modelled and numerically evaluated in particular for yielding 1 μW of mechanical power, the amount necessary to drive wristwatch hands (sect. 2.3).

Chapter 3 deals with the dry friction at the bearing of the polysilicon motors. The materials likely to be used in the process are characterized with pin-on-disc measurements. The validity of the measurement method is discussed. Material combinations are proposed.

Chapter 4 exposes the fabrication processes for both polysilicon and electroplated wobble motors. In the polysilicon process, the aspects of planarization, bearing design and release etching are emphasized (4.1). The motor assembly and the electroplating mould, two important points of the electroplated hybrid wobble motors, are discussed in details. Two versions, i.e. one rigid and one flexible rotors motors are described. The flexible rotor is mounted on a miniature gear train made with conventional machining (4.2).

Chapter 5 relates the testing of the fabricated motors. First, the dedicated electronics for square-wave excitation of the motors is described (5.1). The test set-up is briefly exposed in sect. 5.2. The tests results on polysilicon motors lead to reconsider the bearing construction. Successful operations of polysilicon wobble motors are related (5.3). Operation conditions for the rigid rotor electroplated wobble motors are identified. Charging / discharging of stator isolation layers, and related effects on the motor operation and torque are discussed. Wear after long-time operation (26 hours, one sample) is also characterized. Speed measurements at various excitation frequencies are measured. Contact and non-contact (optical) torque measurement methods are proposed, tested and discussed (5.4). The flexible rotor wobble motor coupled to a gear train is tested with and without liquid lubrication. Pull-in and pull-out voltages of the rotor are measured, and compared to theoretical values (5.5).

Chapter 6 concludes the work.

Chapter 2 - Modelling

2.1 Scaling laws for rotary motors

In this section, we are interested in the conversion of energy, mainly electrical, into mechanical work, and how this conversion behaves as the scale of the rotary actuator is lowered from centimeters to the typical size of MEMS, i.e. some hundreds or tens of microns. The conversion principles considered are: electromagnetic, electrostatic and hydropneumatic. Piezoelectric ultrasonic actuators, which represent also a very promising conversion principle in the micro domain [rac, duf, kasu] are not considered here.

2.1.1 Basic theory

First, we can calculate the forces and torques exerted on the movable part, the rotor, by the fixed part, the stator. The system has n degrees of freedom, hence n generalized coordinates $x_i = (x_1, ..., x_n)$. The equations of J.L. Lagrange (1736 - 1813) of the system are then

$$\frac{d}{dt}\frac{\partial L}{dx'_i} - \frac{\partial L}{\partial x_i} + \frac{\partial R}{\partial x'_i} = 0 \qquad (2.1)$$

with

$$L = T - U \qquad (2.2).$$

T and U are the kinetic and potential energies resp. of the system, and x'_i denotes the time derivative of x_i. R is the function of J.W. Rayleigh (1842 - 1919) and is equal to the half of the dissipated power.

There are, in general, three forces (F_x, F_y and F_z) and three torques (M_x, M_y and M_z) associated to the six displacement coordinates x_i (resp. x, y, z, and φ_x, φ_y, φ_z). In absence of dissipation contributions (R = 0), and if U is only a function of the x_i, one can rewrite the Lagrange equation (2.1), using second Newton's laws (F = ma for translations and $M = I\alpha$ for rotations), as

$$F_x = -\frac{\partial U}{\partial x}, \quad F_y = -\frac{\partial U}{\partial y}, \quad F_z = -\frac{\partial U}{\partial z} \qquad (2.3\text{-}5),$$

and

$$M_x = -\frac{\partial U}{\partial \varphi_x}, \quad M_y = -\frac{\partial U}{\partial \varphi_y}, \quad M_z = -\frac{\partial U}{\partial \varphi_z} \qquad (2.6\text{-}8).$$

These last equations express that the partial derivative of the potential energy w.r.t. a displacement coordinate is equal to the conservative forces or torque along that coordinate.

The cases of variable reluctance (VR) electromagnetic, variable capacitance (VC) electrostatic and hydropneumatic driven actuators, whose elementary operating principles are shown in Fig. 2.1, will be considered. All three are based on a variation of the volume where the potential energy is located, in the air gaps for the first two and in the piston chamber for the third [juf].

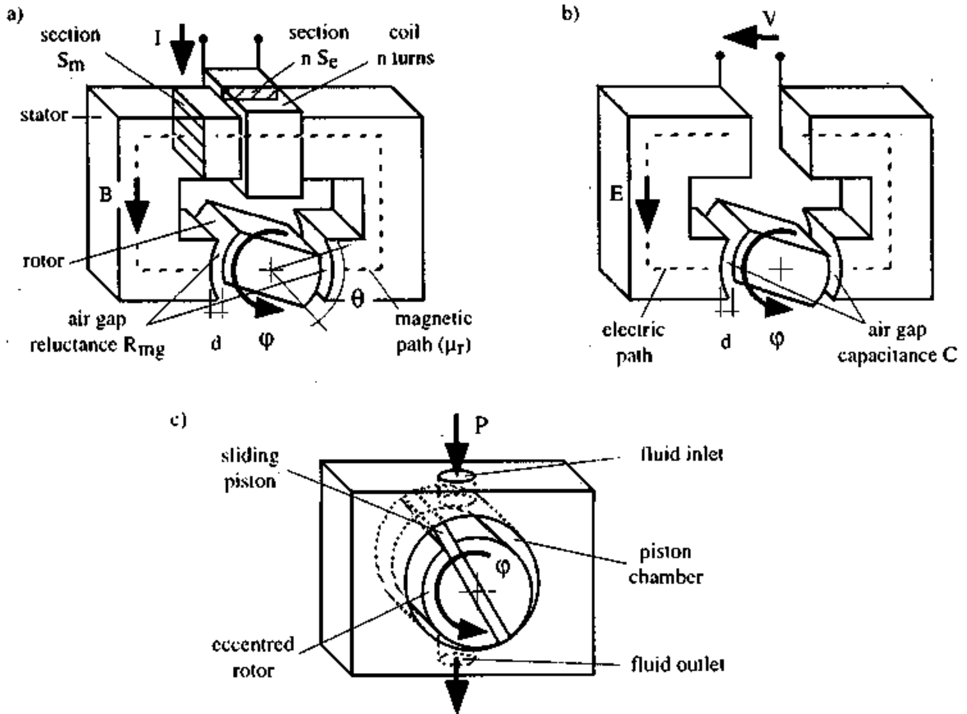

Fig. 2.1 Principles of various rotary actuators. a) VR electromagnetic, b) VC electrostatic, c) hydropneumatic.

One can define then the specific energy at these locations by

$$u = \frac{U}{V} \quad [\mathrm{J/m^3}] \tag{2.9}$$

where V denotes the volume of the active area (air gaps or piston chamber). If we consider a rotary system supplied with a constant specific energy, the motive torque is given by one of the eqs. (2.6-8) and can be rewritten using eq. (2.9) as

$$M = -\frac{\partial}{\partial \varphi}(u\,V) = -u\,\frac{\partial V}{\partial \varphi} \tag{2.10}$$

To obtain a maximum torque, one should have a maximum specific energy and a maximum volume change rate. According to [juf], the specific energies for the three principles of actuation mentioned, resp. electromagnetic, electrostatic and hydropneumatic are given by

$$u_{em} = \frac{1}{2}\frac{B^2}{\mu_0} \qquad (2.11),$$

$$u_{es} = \frac{1}{2}\varepsilon_0 E^2 \qquad (2.12),$$

$$u_{hp} = p \qquad (2.13),$$

where B and E are resp. the magnetic and electric fields, and p, the internal pressure. Sometimes, the electric specific energies u_{em} and u_{es} are also referred to as magnetic and electric pressures [guc4].

In practice, the maximum values for hydropneumatic pressures are limited to 400 bars ($u_{hp\ max} = 4 \times 10^7$ J/m^3), which is admissible for most of the materials employed for the chamber. Hence for centimeter sizes and lower, very large forces can be developed with this principle. Nevertheless, the production, transportation and distribution of pressure is more difficult than that of electricity. Moreover, the frequencies, hence the specific power attainable with electric devices are much higher than these of hydropneumatic devices [juf]. Therefore, only the theoretical evaluation of the electrically driven devices will be pursued hereafter.

For the electromagnetic actuator, a typical maximum value of B = 1 T in the air gaps is imposed by the magnetic saturation level in the ferromagnetic path, at any scale. Using eq. (2.11), the corresponding specific energy is 4×10^5 J/m^3 [juf]. Nevertheless, when scaled down, two limitations appear. First, the current density in the coil wires is limited by the thermal strength of the isolation (normally a polymer) to typically 6 A/mm^2 [juf]. Second, the temperature of the coil operated at constant current increases because of the reduced copper cross-section. This last effect is the most determining, and consequently, the maximum admissible temperature of the device is the limiting factor. At small sizes, the coil heat is mainly evacuated by air convection. Consequently, to achieve still acceptable magnetic induction levels and operating temperatures, small magnetic motors have large coils compared to the rotor size [juf], as exemplified by the wristwatch motor of Fig. 2.2. The incorporation of small permanent magnets in the construction also permits to obtain a higher induction level, but does not solve the thermal problem.

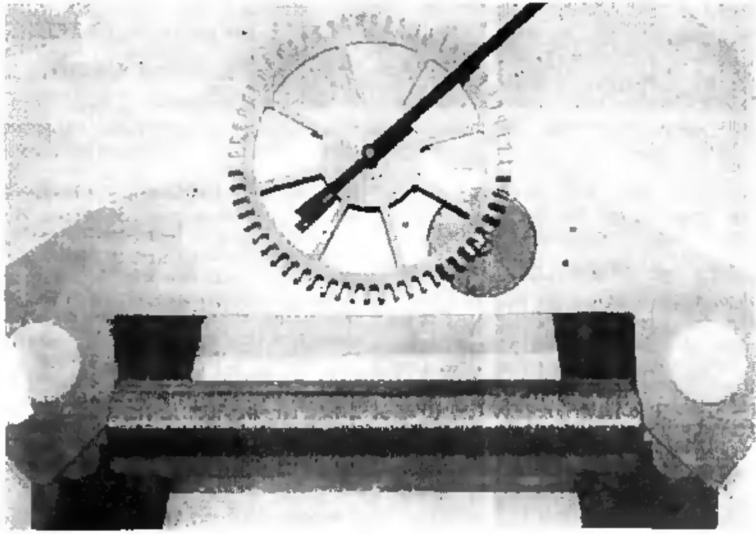

Fig. 2.2 Scale model of a typical wristwatch Lavet-type stepper motor (source: Neue Zuercher Zeitung 26.4.95, nr 96).

The electrostatic specific energy is limited by the maximum electrostatic field value before air breakdown occurs. The breakdown voltage V_{br} is a function of the product of the air gap distance d and the air pressure p, as described first by Paschen [pas] Fig. 2.3 shows a plot of the values for air at 20°C, as given by the table C 2 from Dakin et al. [dak].

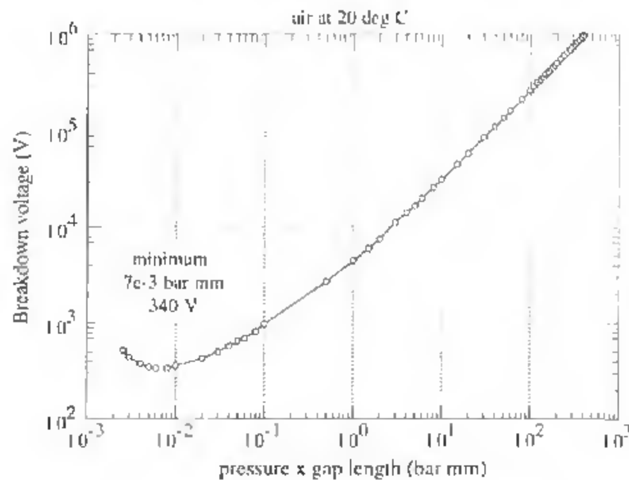

Fig. 2.3 Paschen curve in air at 20°C [dak]

The importance of this phenomenon to the subject justifies the following explanation. During breakdown, primary electrons are accelerated in the direction of the anode, and acquire enough energy to ionize the air molecules: one primary electron generates one secondary, which in turn generate four, and so on, propagating towards the anode (avalanche). In addition, more primary electrons are needed to maintain the discharge current. These are obtained by extraction from the cathode through bombardment by the ionized air molecules. The breakdown persists if, statistically, one primary electron at least is replaced by another one extracted from the cathode.

Let us illustrate the Paschen curve along a horizontal line passing above the minimum, at constant voltage and atmospheric pressure, and going from right to left with decreasing air gap. On the right side before breakdown, the mean free path between molecules is too short to allow the electrons to acquire the necessary ionization energy between two chocks. If the gap is decreased, the field increases and the electrons are accelerated more rapidly, i.e. they acquire the ionization energy on a shorter path. If this critical ionization path is smaller than the mean free path, breakdown occurs. Still lowering the gap size, we cross the curve again in its increasing left part. Here the mean free is still longer than the critical electron acceleration, but the extraction condition is no more fulfilled: due to the reduced gap length, a lower number of ions are produced. Thus not enough primary electrons are extracted from the cathode, and breakdown stops.

As a consequence, the number of molecules in the air gap seems to be the only determining factor of the breakdown voltage, regardless of their proximity (density) [tav2, dak]. This number is effectively fixed for given pressure and gap length.

Returning to quantitative considerations of the Paschen curve of Fig. 2.3, at ambient pressure centimeter-sized motors with air gaps longer than one half millimeter sustain electric fields up to approximately 3×10^6 V/m. Using eq. (2.12), we obtain a specific energy of 10^2 J/m^3, which is rather poor compared to the two other types of actuation. Citing Kasper [kasp], "This clarifies that research and application during the last hundred years were concentrated on magnetic converters.".

But the ability to fabricate nowadays smaller gaps using micromachining changes drastically the point of view [tri1, bar1, tav2]. The Paschen curve reaches a minimum at approximately 340 V and 7 µm, after what V_{br} increases [tav2]. At this minimum, we have already a field of 5.7×10^7 V/m, leading to $u_{es\ max} = 1.4 \times 10^4$ J/m^3. Decreasing the air gap length beyond this point leads to much higher field values, so that the energy density becomes comparable, and even superior to the one of electromagnetic actuators of that size.

The breakdown voltages in that region of the Paschen curve are more or less confirmed by other sources. Breakdown voltages in the neighborhood of 1000 V have been measured by R. Vuilleumier, in dry air at atmospheric pressure, on electrostatic microshutters

with gaps of 10 to 20 μm [vui]. The same author detected no breakdown at 100 V between tips distant a few microns. Breakdown voltages between 300 and 350 V for gaps between 1 and 7 μm have been measured on electromagnetic microrelays [hos]. Still, these values are quite high for measurements in non-uniform fields, as generally expected in practical electrostatic devices. In the measurements carried out by Paschen [pas] and as reported by Dakin et al. [dak], two spherical electrodes were used to generate a quasi uniform field in the breakdown region.

2.1.2 Compared performances of electromagnetic and electrostatic drives

From the last statements, the level of specific -hence convertible- electrostatic energy comes out to be higher than the magnetic for micrometer-sized gaps. This will be theoretically assessed hereafter with a comparative calculation. The hydropneumatic solution is left aside mainly because of difficulties in producing and handling of the fluid, but still remains the most powerful for particular applications, like microsurgery and hard endoscopy.

We will focus on variable reluctance (VR) magnetic and variable capacitance (VC) electrostatic systems, i.e. that are only excited by coils and conductive electrodes, and have no permanent magnets or electrets. The maximum mechanical torque of each system will be evaluated as a function of its size, assuming that the scaling factors are resp. the maximum breakdown voltage for the electrostatic, and the maximum coil equilibrium temperature for the electromagnetic system.

Let us first consider more closely the elementary electromagnetic system shown in Fig. 2.1 a. It has only one excitation coil to simplify the calculation. This system can be easily extended to a continuous rotating system by addition of supplementary coils and averaging of the step torques. The rotor angular position is denoted by φ, its pole width by θ. The ferromagnetic path has a cross-section S_m, a mean length l_m and a relative permeability of μ_r. The coil is characterized by its wire cross-section S_e of resistivity of ρ_{el} and by the number of turns n. A voltage V applied to the coil causes a continuous current I to circulate in it.

The Ampere law relates the circulation of B along the unique magnetic path to the current traversing any surface having the magnetic path as boundary. Using the formalism of magnetic circuits, this law can be written as

$$\Theta = (R_{mm} + 2\,R_{mg})\,\Phi \tag{2.14}$$

where Θ, R_{mm}, R_{mg} and Φ are resp. the magnetic coil potential, the ferromagnetic and air gaps reluctances (=magnetic resistances) and the flux. The magnetic potential is equal to the total coil current, $n\,I$. The flux is given by the product of B and the magnetic path cross-section.

The ferromagnetic path and air gap reluctances are resp. given by

$$R_{mm} = \frac{l_m}{\mu_r \mu_0 S_m}, \qquad R_{mg} = \frac{d}{\mu_0 |\theta - \varphi| R l} \qquad (2.15, 16).$$

Typically, μ_r is equal to 500 for iron, $l_m \sim 50$ d and the air gap cross-section is at maximum (φ=0) equal to the ferromagnetic one. Hence, R_{mm} becomes negligible compared to R_{mg} and can be removed from the calculation. Using eqs. (2.14-16), the magnetic field of the air gaps, B_g, can be obtained:

$$B_g = \frac{\mu_0}{2d} n I \qquad (2.17).$$

At a few millimeter size or lower, we can assume that the heat generated by electrical excitation of the coil is transferred essentially by convection to the surrounding air, rather than by conduction [juf]. Therefore, the relationship between the temperature rise of the coil, ΔT (= the temperature difference between motor and ambient), and the current density, J, is given by:

$$\Delta T = \frac{\rho_{el} J^2 V}{\chi A_\chi} \qquad (2.18),$$

where V and A_χ denote resp. the motor volume and convection area, and χ the convection coefficient in air (W/mK). Combining the last two equations, one gets the relation between the induction level and the temperature rise:

$$B_g = \frac{\mu_0}{2d} n^2 S_e \sqrt{\frac{\Delta T \chi A_\chi}{\rho V}} \qquad (2.19).$$

We consider now a homothetic, tridimensional scaling of both electromagnetic and electrostatic actuators. If the size of a reference (large) motor is l, and the one of the homothetic (small) motor is l', then the scaling factor, l*, is defined by [juf]

$$l^* = \frac{l'}{l} \qquad (2.20).$$

How do the specific energies and the volume change rate defined in eq.(2.10) behave when a centimeter-sized motor is scaled down ? The volume change rate of both motors is directly proportional to the volume itself and hence scales as

$$\left(\frac{\partial V}{\partial \varphi}\right)^* = l^{*\,3} \qquad (2.21).$$

For the electromagnetic system, using eq. (2.19) with the physical parameters n, ρ_{el}, ΔT and χ constant, the gap induction level scales as

$$B_g^* = l^{*\,0.5} \qquad (2.22).$$

Replacing eq. (2.22) in eq. (2.11) yields for the specific potential energy

$$u_{em}^* = l^* \qquad (2.23).$$

Similarly, the maximum allowable electrostatic specific energy for a motor as shown in Fig. 2.1b can be calculated as a function of the gap length using eq. (2.12) and the Paschen curve (Fig. 2.3).

We can compute a numerical example of the maximum static torques for both machines. A "large" motor is chosen, with the following realistic parameters: a rotor external diameter of 30 mm, a rotor active length of 30 mm, a rotor-stator gap of 0.3 mm (i.e. 1/100 of the rotor size). For the "large" electromagnetic motor, a maximum gap induction level of 1 T is imposed by the induction saturation level of the ferromagnetic circuit, generally iron.

The torques for both large motors are first calculated using eqs. (2.10), (2.11), (2.12) and the Paschen curve. Then, both torque expressions are calculated as a function of the air gap length for homothetic machines down to the micrometer range, using eqs. (2.21), (2.22), (2.23) and the Paschen curve. The result is shown in Fig. 2.4. For centimeter-sized machines (d=0.1-1 mm), the electromagnetic torque is several orders of magnitude the electrostatic one. There is a crossing point at d = 7 µm, where both motors deliver similar torques. At d = 2.5 µm, the electrostatic motor delivers already more than ten times the torque of the electromagnetic motor.

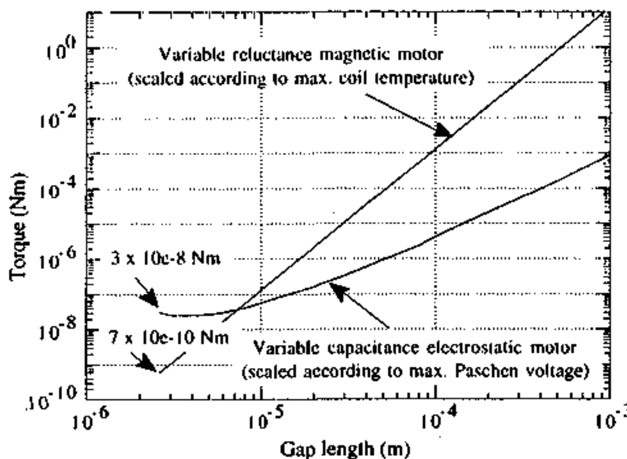

Fig. 2.4 Calculated electrostatic and electromagnetic torques of homothetic motors as a function of the gap length.

As a consequence, in order to keep a constant temperature rise, the coil of the magnetic motor has to be much larger than the magnetic circuit and rotor, whereas the electrodes of the electrostatic motor remain of the same size as the rotor. In addition, at electric equilibrium (static state), electric charges keep located at the surfaces of electrodes whereas the magnetic induction field establishes in the volume of the magnetic circuit. This is confirmed by Mikuriya [mik]: "With respect to physical size, electrostatic motors, where force depends on the surface area of rotor are more advantageous than electromagnetic motors, where force depends on the volume of the rotor.". Hence, electrostatic motors can be built much more compact then their electromagnetic equivalents.

We consider now the dynamic behavior of two such micro-electrostatic and electromagnetic motors, each of same static torque and size. If the cutoff frequency is determined mechanically, their maximum rotation speed, hence mechanical power are equal. If the cutoff frequency is determined electrically, the electrostatic mechanical power may be higher than the electromagnetic, because large coils are energized less rapidly than small capacitors. Nevertheless, appropriate calculations have to be made to reinforce this statement.

These considerations prove the theoretical ability for electrostatic motor performances to surpass the ones of their electromagnetic duals, when respectively the air gaps and the rotor sizes are lowered beyond typically 10 microns and 1mm. This is in good agreement with Mikuriya [mik] concluding that "the electrostatic micromotor (their modelization) is more effective in terms of torque than the electromagnetic micromotor when the size is less than 1.5 mm ø".

2.2 Integrated polysilicon variable-capacitance synchronous micromotors [1]

Starting from realizable, surface-micromachined polysilicon variable-capacitance motors concepts, various types of synchronous stepper motors are proposed and analytically modelled. The step torques of motors with fixed dimensions are calculated for comparison between each type. Some of the realized prototypes are then evidently fabricated at these modelling dimensions (see fabrication).

2.2.1 Principle

Variable capacitance (VC) synchronous stepper motors work nearly similarly as their magnetic duals, the conventional variable reluctance (VR) stepper motors. The rotor disc has salient teeth and is surrounded by stator electrodes of same width (Fig. 2.5). Other electrodes dispositions and number combinations are possible.

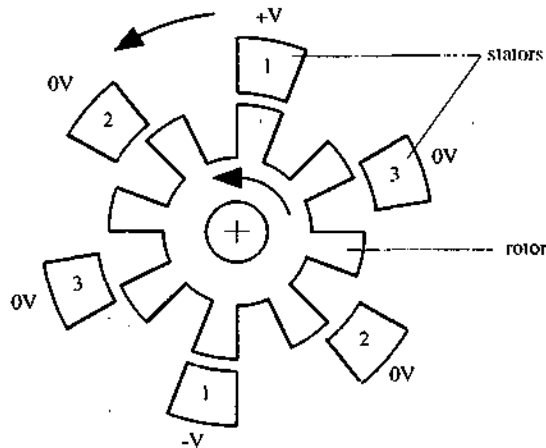

Fig. 2.5 Operating principle of a variable capacitance, synchronous stepper motor, here in a 8:6 rotor-stator configuration.

One phase formed by two diametrically opposed stator electrodes (here phase #1) is excited at the potentials +V and -V, causing the rotor to align to the electrodes, so as to minimize the potential energy in the air gaps (see eqs. 2.3-8 with zero conservative forces or torques). If the rotor is grounded, the two air gap capacitances are in parallel. If the rotor is floating, these are in series. If the next CCW (counter clockwise) phase (#2) is switched on at

[1] Part of this work is published in [bor]

the same time the first one is switched off, the rotor will rotate one step in CCW direction, and so on for continuous operation. Hence the rotation speed is synchronized to the electric field switching speed, or excitation frequency. This kind of motor is thus named "synchronous", and abbreviated SM for stepper motor.

2.2.2 Process-induced design considerations

Solid conductive and non-conductive layers a few microns thick can be deposited using surface micromachining. Moreover, the typical micromachining precision in x-y dimensions being a few tenths of microns, a reasonable rotor diameter is a hundreds of microns. The realized structures will thus rather have a "flattened" than a three-dimensional aspect. Getting inspiration from the elementary process of Fig. 1.3, let's look at one possible process to make an electrostatic motor as described in sect. 2.2.1. The first question is how to fabricate a rotary element.

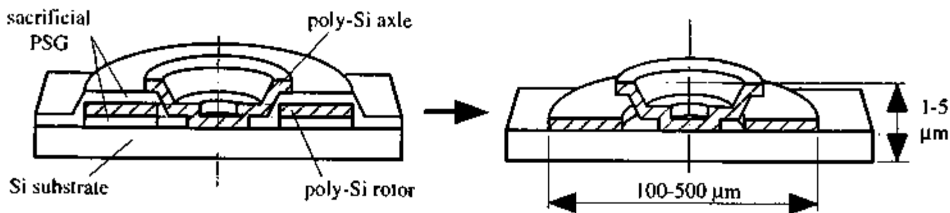

Fig. 2.6 Cross-sectional perspective view of a surface micromachined polysilicon rotary disc, before (left) and after (right) the sacrificial PSG layer etching.

Fig. 2.6 shows a cross-section of a possible construction, were only the two last process steps are shown, i.e. before (left) and after (right) the etching of the sacrificial layer (not to scale). This process needs three photolithographic masks, two PSG and two polysilicon depositions. One can already see that removing the sacrificial layer will cause the disc to "fall" on the substrate (Fig. 2.6 left). Consequently it will no more be guided around the axle at the appropriate height - where the axle is auto-aligned to the rotor hole. Moreover, the entire disc surface will rub onto the substrate. To avoid this, it is possible to form some bushings to the rotor so that it will be kept offset from the substrate as shown in Fig. 2.7.

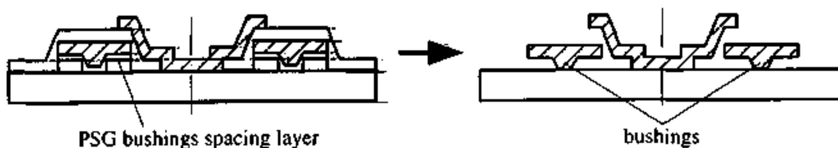

Fig. 2.7 Cross-sectional view of a surface micromachined polysilicon rotary disc, with bushings to keep the rotor offset from the substrate.

The bushings are formed by defining their negative shape in the PSG layer, followed by a very thin PSG "refill" deposition to prevent them from adhesion to the substrate. This step needs one more mask, thus bringing the total number to four. Note that the lateral and tilt bearing plays are determined by the thicknesses of the second and refill PSG layers. To build a motor, the rotor and the stator electrodes have now to be shaped somehow around this rotating disc. Still evolving from Fig. 2.7, the construction of a typical VC side-drive stepper motor, as described in sect. 2.2.1, is considered. Fig. 2.8 shows such a motor, of the same type as the ones of Muller et al. [mul] and Tavrow et al. [tav1].

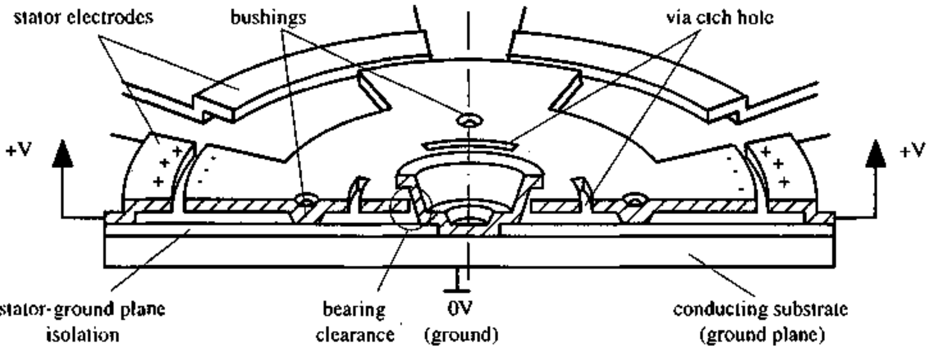

Fig. 2.8 Cross-sectional perspective view of a polysilicon surface micromachined, electrostatic VC synchronous side-drive stepper motor.

The conductive substrate is connected to the rotor via the bearing and consequently prevents the rotor to be electrostatically attracted downwards, which would cause additional friction torque. Depending on the process, the conducting region underneath the rotor may no more be the entire substrate but only a limited region which is called "ground plane" [mul, tav2]. An isolation layer prevents short-circuit between the stator electrodes and to the ground plane. One more mask than in the process of Fig. 2.7 is needed to define the attachment regions of the stator electrodes to the substrate. The process needs thus five masks. Via holes in the rotor allow a better sacrificial layer underetching in the bearing clearance (circled region).

Following the same process deductions and refinements as for the side-drive motor of Fig. 2.8, different types of polysilicon electrostatic motors have been designed to fit a nine-mask process (see fabrication). These motors are analytically evaluated in the next sections.

2.2.3 The side-drive motor

Variable capacitance side-drive motors have been already studied and characterized by many groups [tai1, mul, meh2, bar2, tav1]. A typical motor of this type is shown in Fig. 2.9.

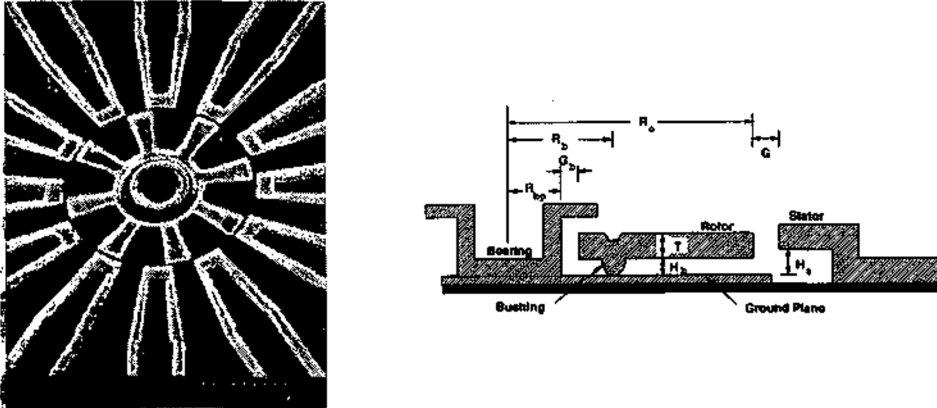

Fig. 2.9 Left: SEM of a 8:12 (rotor: stator teeth), 100 μm diameter VC side-drive electrostatic micromotor. Right: schematic cross-section [bar2].

Bart et al. report experimental data (the measured rotor speed) fitted to a model of the rotor dynamics, from which practical parameters such as torque, friction, etc. can be extracted [bar2]. During rotation, the rotor experiences the air drag torque, the electrostatic excitation drive and friction torques, a constant friction torque -which is supposed to be due to trapped charges in native oxide, and the gravitational friction torque. As a result of the data fitting, only the drag and electrostatic excitation torques are found to be determinant for the dynamics. Starting from these experiences, this kind of motor will be remodeled hereafter, for comparison with the top-drive motor of the next section.

Fig. 2.10 shows a modelling schematics of the motor, where only one phase (two opposite stator electrodes) is represented, the rotor and stator teeth number being not important for the calculation of the torque on one step. Finite element modelling of [tav2] showed that vertical rotor displacements up to typically the rotor thickness do not induce significant changes of the drive torque and the side-pull force, hence this parameter is not considered. The rotor is assumed to be electrically conductive and grounded. If a constant voltage V is applied to one phase, the rotor teeth tend to align to the facing stator teeth (of same width θ), and close the air gap (dotted area) by rotating around z. But as the faces overlap, rotor side-pull forces F_1 and F_2 appear.

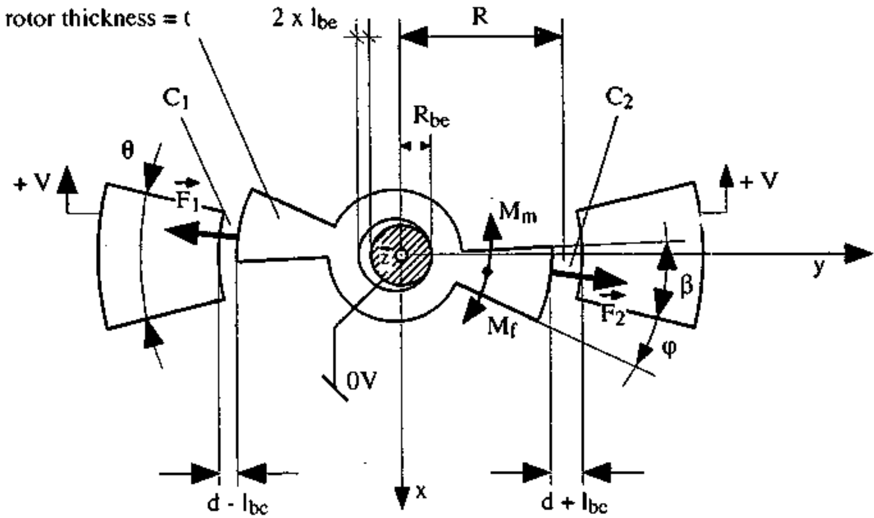

Fig. 2.10 Modelling schematics of the VC side-drive motor.

The bearing clearance, l_{be}, allows the rotor to move laterally, causing imbalance between both pulling forces F_1 and F_2 that do no more cancel each other. This results in a retarding friction torque due to the resultant side-pull force exerted against the axle [tav1]. The fringing fields around the rotor-stator air gaps are assumed to be negligible, i.e. the overlapping areas can be considered as parallel plate, variable air gap capacitors with homogenous field [bar4]. According to chapter 2, the electrostatic torques are equal to the derivative of the gap energy w.r.t. the rotor rotation angle φ (eqs. 2.6-8). Hence the drive torque M_m is given by

$$M_m = M_{m1} + M_{m2} = \frac{1}{2} V^2 \left(\frac{\partial C_1}{\partial \varphi} + \frac{\partial C_2}{\partial \varphi} \right) \tag{2.24}$$

where C_1, C_2 denote the air gap capacitors, which can be calculated as a function of the geometry:

$$C_1 = \varepsilon_0 R\, t\, (\theta - |\varphi|)\, \frac{1}{d - l_{be}} \tag{2.25}$$

and

$$C_2 = \varepsilon_0 R\, t\, (\theta - |\varphi|)\, \frac{1}{d + l_{be}} \tag{2.26}$$

where R denotes the rotor radius, $d \pm l_{be}$ the air gap length and t the rotor thickness. We assume that $R >> d \pm l_{be}$. Introducing eqs. (2.25) and (2.26) into eq. (2.24) yields

$$M_m = -\,\mathrm{sign}(\varphi)\, \frac{1}{2} V^2 \varepsilon_0 R\, t \left(\frac{2d}{d^2 - l_{be}^2} \right) \tag{2.27}$$

which is zero when rotor and stator are aligned ($\varphi = 0$), and the sign of which is opposite to the one of the angle. The side-pull forces F_1 and F_2 are calculated by taking the derivative of the energy of the air gap capacitors w.r.t. the bearing clearance coordinate. The friction torque M_f is then given by the resultant of the two forces, $F_1 - F_2$, multiplied by the bearing radius R_{be} and by the bearing dynamic friction coefficient μ_{be} between rotor and axle:

$$M_f = -\,\mathrm{sign}\left(\frac{\partial \varphi}{\partial t}\right) \frac{1}{2}\, \mu_{be} R_{be} V^2 \varepsilon_0 R\, t\, (\theta - |\varphi|) \left(\frac{1}{(d - l_{be})^2} - \frac{1}{(d + l_{be})^2}\right) \quad (2.28),$$

which is zero when the rotor is at standstill, and the sign of which is opposite to the one of the speed. The rotor will move to align to the stator as long as the drive torque is bigger than the friction torque. Going from movement to standstill requires the use of the dynamic friction coefficient. The static equilibrium is then reached when $M_m = M_f$, i.e. at the zero net torque angle φ_0. Using eqs. (2.27) and (2.28), the rotor-stator overlap angle β_0 can be calculated:

$$\beta_0 = \theta - \varphi_0 = \frac{1}{2 \mu_{be} R_{be}} \frac{d^2 - l_{be}^2}{l_{be}} \quad (2.29).$$

We can see that this overlap angle is independent from the tooth width, the rotor radius and thickness, and the excitation voltage. For proper continuous motor operation, the overlap has to be ideally as big as the tooth width, otherwise the next phase will not catch the rotor.

2.2.4 *The top-drive motor*

The variable capacitance top-drive motor is different from the side-drive in that the stator electrodes are not placed radially around the rotor, but underneath it (Fig. 2.11). The rotor-stator field lines are globally axially oriented, therefore this type of motor is also referred to as *axial* field motor [par1]. The rotor-stator overlap, hence the drive torque, is higher than for the radial field motor. On the other hand, as the rotor and stator overlap, an axial force pulls the rotor against the substrate, causing a retarding friction torque, the lever arm of which is the bushings radius. Bart et al. proposed a design where this pull-down force is balanced by supplementary upper stators (Fig. 2.12) [bar1].

Nevertheless, rotor axial and tilt instabilities, leading to rotor-stator short-circuit, are major drawbacks for this design [tav2]. A similar design has been proposed by Mehregany et al. (Fig. 2.13) [meh2]. As reported by these authors, and as it can be deduced from the figures, the sacrificial layer -no more present here- between rotor and upper stators must be planarized, otherwise the stators fabricated over the rotor teeth are at different elevation than the other stators. This is another drawback of the double-stator solution.

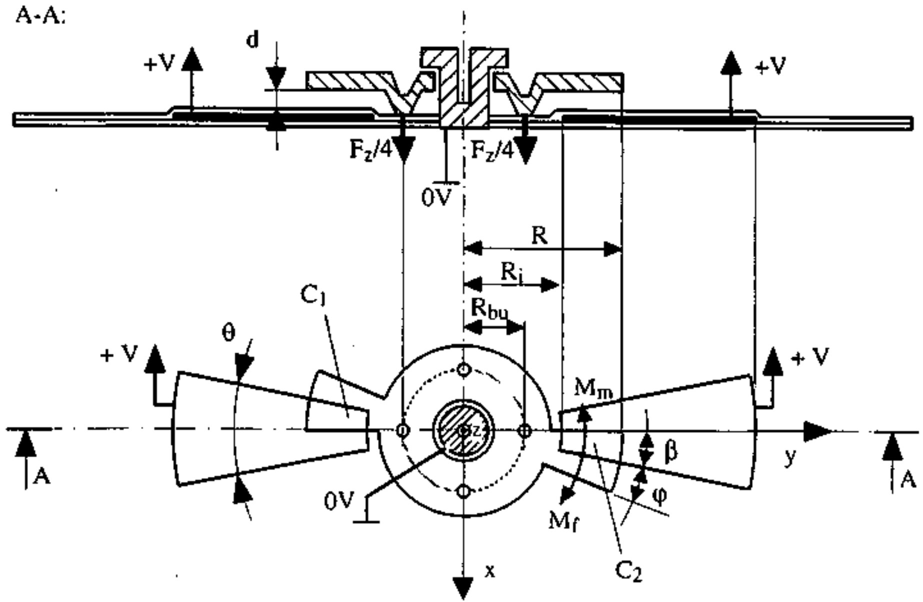

Fig. 2.11 Modelling schematics of the VC top-drive motor.

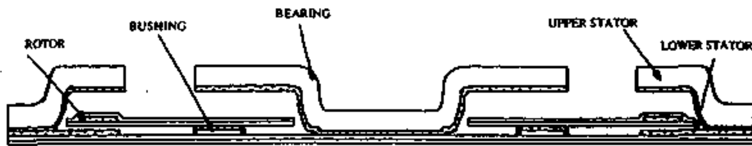

Fig. 2.12 Process cross-sectional view of a double stator top-drive VC stepper motor [bar1].

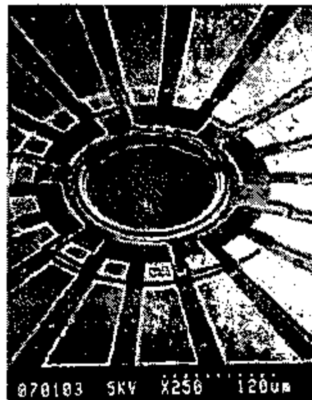

Fig. 2.13 SEM of a three-phase VC top-drive micromotor (rotor diameter 300 μm) [meh2].

Therefore, we come back to the primary design of Fig. 2.11 and perform the same calculations as for the side-drive motor. The drive torque is given by eq. (2.24). The lateral bearing play, in the order of one micron, causes only small changes to the air gap capacitances which radial length is a few tens of microns. Hence we have $C_1 = C_2 = C$, which can be expressed as

$$C = \frac{1}{2}\frac{\varepsilon_0}{d}\,(R^2 - R_i^2)\,(\theta - |\varphi|) \tag{2.30}$$

where d is the rotor-stator gap length along the field lines (z-oriented), and R_i the inner radius of the stators. The transparent layer is dielectric (silicon nitride) and basically prevents accidental short-circuit between rotor and stator teeth. It has been neglected in eq. (2.30) for the following reason. The exact value of the total capacitance C of the air gap and the dielectric in series is given by

$$\frac{1}{C} = \frac{1}{C_a} + \frac{1}{C_i} = \frac{d}{\varepsilon_0 A} + \frac{d_i}{\varepsilon_0 \varepsilon_r A} \tag{2.31}$$

where A is the rotor-stator overlap area, and ε_r, d_i and C_i resp. the dielectric constant, its thickness and its capacitance. C_a denotes the air gap capacitance. For typical process values, we assume $d_i = 0.3\ \mu m$ and $d = 1.5\ \mu m$. The dielectric constant for LPCVD silicon nitride is $\varepsilon_r = 6$ [sze]. Introducing these values into eq. (2.31), C_i is 30 times C_a, hence the total capacitance C is nearly equal to C_a. Introducing the derivative of eq. (2.30) w.r.t. the rotation angle into eq. (2.24) yields:

$$M_m = -\,\mathrm{sign}(\varphi)\,\frac{1}{2}V^2\,\frac{\varepsilon_0}{d}\,(R^2 - R_i^2) \tag{2.32}$$

Using eq.(2.30), the pull-down force F_z exerted at the bushings is given by

$$F_z = \frac{1}{2}V^2\,\frac{\varepsilon_0}{d^2}\,(R^2 - R_i^2)\,(\theta - |\varphi|) \tag{2.33}$$

The resulting retarding friction torque M_f is given by

$$M_f = \mu_{bu}\,R_{bu}\,F_z \tag{2.34}$$

where μ_{bu} denotes the friction coefficient at the bushings, and R_{bu} their radius. As before, the overlap angle can be found when solving the equality $M_f = M_m$ and by using the last three equations:

$$\beta_0 = \frac{d}{2\,\mu_{bu}\,R_{bu}} \tag{2.35}$$

Again, as in eq.(2.29), this overlap angle is independent from the tooth width, the rotor radius, the inner stator electrode radius, and the excitation voltage.

2.2.5 *Static performances of side- and top-drive motors*

Table 2.1 Parameters of side- and top-drive motors as used for the numerical application.

Both motors:			
rotor radius [par1]	R	100	μm
bearing radius [par1]	R_{be}	30	μm
dynamic dry friction coefficient	$\mu_{be} = \mu_{ba}$	0.1, 0.4	
Side-drive motor [tav2]:			
bearing clearance	l_{be}	0.35	μm
rotor thickness	t	2.55	μm
Top-drive motor [par1]:			
stator teeth internal radius	R_i	60	μm
bushings radius	R_{bu}	50	μm

A comparison between side- and top-drive motors of same dimensions will be made through a numerical example with possibly realistic parameters, listed in Table 2.1. Some parameters for the side-drive motor are taken from Tavrow's thesis [tav2], and some other from our first design [par1]. The minimum possible bearing radius is 30 μm according to our layout design constraints (see fabrication). Thus the bushings radius, which must be bigger, is chosen at 50 μm. In both motors, the electrostatic friction torque is due to dry friction of LPCVD polysilicon rotors against LPCVD silicon nitride. In the case of the side-drive, the nitride is covering the bearing hub [tav2], whereas for the top-drive it is the isolation layer. A realistic dynamic dry friction coefficient of 0.4 is chosen [tav2]. The use of solid lubricant monolayers could potentially reduce μ to around 0.1 [zar], therefore this value is also taken for the calculation.

Fig. 2.14 shows a plot of the overlap angles as given by eqs. (2.29) and (2.35) as functions of the air gap length d, with the parameters of table 2.1. The overlap angle has to be as high as possible, so that possibly wide angle stators, hence few electrodes can be designed. The plot shows that large overlap angles exist for the side-drive motor (continuous lines) even at a dynamic friction coefficient of 0.4, which is not the case for the top-drive motor (dotted lines), unless its friction coefficient is lowered at typically 0.1.

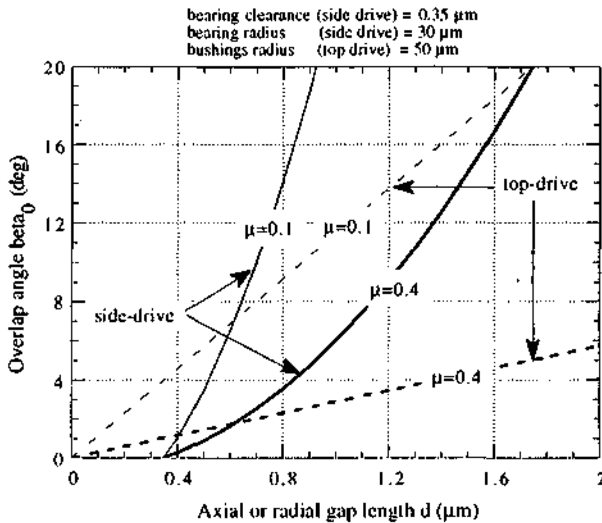

Fig. 2.14 Rotor-stator overlap angle (at which drive and friction torques balance) in function of the gap distance, for two friction coefficients and for side-drive (continuous lines) and top-drive (dotted lines) motors.

It is then significant to look also at the maximum net torque, also called figure of merit [tav2], $M_n = M_m - M_f$, numerically. This torque is zero when there is no overlap, and decreases linearly from M_{nmax} to $-M_{nmax}$ as shown in Fig. 2.15.

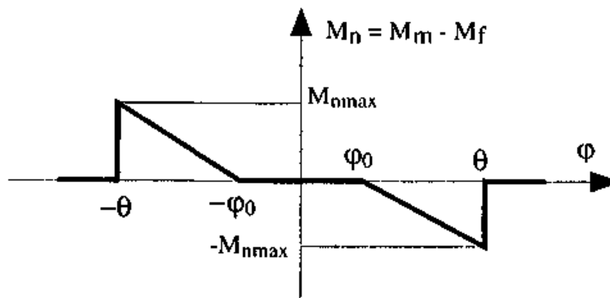

Fig. 2.15 Net torque dependence of the rotor position.

The absolute value of the net torque is maximum at the angular positions $\varphi = -\theta$ and θ, where the friction torque is still zero. Hence, from eq. (2.27), the maximum value M_{nmax} for the side-drive motor is given by

$$M_{nmax}\ (\text{side-drive}) = \frac{1}{2} V^2 \varepsilon_0 R\, t \left(\frac{2d}{d^2 - l_{be}^2} \right) \tag{2.36}$$

Similarly, from eq.(2.32), the maximum value for the top-drive motor is given by

$$M_{nmax}\ \text{(top-drive)} = \frac{1}{2} V^2 \frac{\varepsilon_0}{d} (R^2 - R_i^2) \qquad (2.17).$$

Fig. 2.16 shows a plot of eqs. (2.36) and (2.37), normalized w.r.t. the actuation voltage squared, as a function of the gap distance d, for the values listed in table 2.1. The graph shows that a 200 μm diameter top-drive motor yields about ten times the torque of a side-drive motor, for the same rotor dimensions. This is a result of the larger overlapping areas of the top-drive.

We can thus deduce that the top-drive is an interesting solution, provided that the friction coefficient at the bushings is low enough to keep an overlap angle as high as possible.

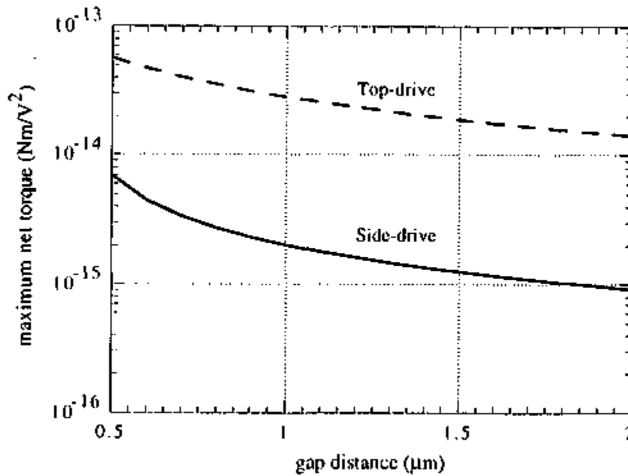

Fig. 2.16 Maximum net torques (φ=±θ) in function of the gap distance, for side and top-drive motors of same size (parameters of table 2.1).

2.2.6 *The comb-drive motor [par2]*

The comb-drive motor of Fig. 2.17 is basically different from the side-drive motor in that the number of working air gaps per sector is more than one, so as to yield more torque. The stator and rotor teeth, both formed in the middle level polysilicon, are interdigitated. The rotor comb teeth are connected together and to the central hub by means of linkage arms formed in the top level polysilicon, i.e. the same as for the bearing post. Note that these arms may be used to support an outer, peripheral drive gear or mechanism, formed in the middle or top level polysilicon. The stator comb teeth of one sector electrode are connected to a stator conduction land formed in the lower level polysilicon (see also the cross-section of Fig. 4.4, in the fabrication chapter).

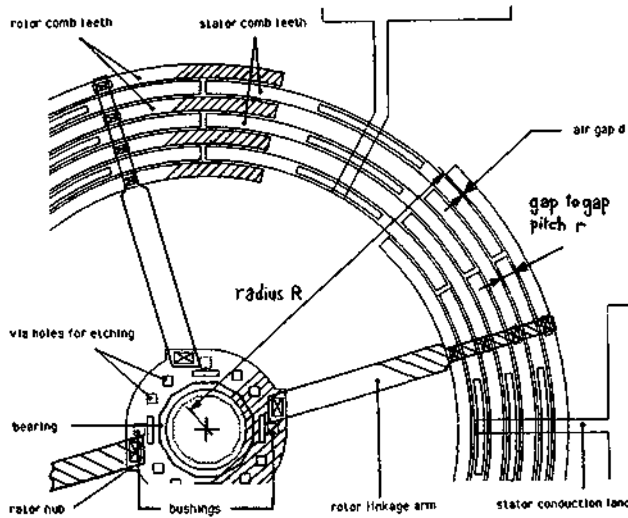

Fig. 2.17 Top view of a 4:6 VC comb-drive stepper motor.

Hereafter we compare the static motor torques developed by the side- and the comb-drive motors analytically. The relevant parameters common to both motors are: the (radial) air gap distance d, the rotor thickness t, the outermost air gap radius R, the tooth width θ, the rotor position angle φ and the excitation voltage V. We assume to have no bearing play, i.e. $l_{be} = 0$. The parameters relative only to the comb motor are: the radial gap-to-gap pitch r and the number of air gaps n_g. One comb capacitance of width $\theta - |\varphi|$ is given by the sum of all n_g air gap capacitances, connected in parallel. Using eqs. (2.25) and (2.26) with $l_{bc} = 0$ and summing up over n_g, this capacitance can thus be expressed as:

$$C_1 = C_2 = \sum_{i=0}^{n_g-1} \frac{\varepsilon_0 t (R - ir)}{d} (\theta - |\varphi|). \qquad (2.38).$$

The resulting comb motor torque per phase, M_{mcomb}, is then obtained by introducing eq. (2.38) into eq. (2.24). Using this result and eq. (2.27), the motor torque ratio M_{mcomb} / M_{mside} is then simply given by:

$$M_{mcomb} / M_{mside} = n_g \left(1 - \frac{(n_g - 1) r}{2R} \right) \qquad (2.39).$$

Fig. 2.18 shows a plot of eq. (2.39), as a function of the gap number, for two different geometrical r/R ratios. This plot shows that the comb drive motor torque is nearly n_g times higher than the side-drive motor torque, when the gap-to-gap pitch of the comb drive, r, is small compared to the outermost gap radius R. In reality, a non-zero bearing clearance exists, and hence also a side-pull, position-dependent friction torque. It can be calculated that this

torque is also about n times higher than for the side-drive. In consequence, the overlap angle will be the same as for the side-drive, but the net torque is increased nearly proportionally to the number of working air gaps.

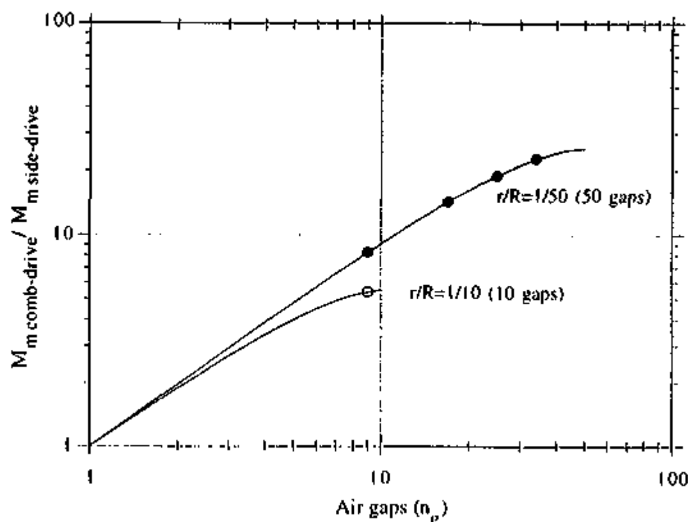

Fig. 2.18 Comb / side-drive motor torque ratio as a function of the comb air gap number, for a same outer rotor radius of 270 µm.

But the enhanced rotor side-pull force, as described before, represents a potential advantage, as follows. As reported in [meh4], the main operation problems encountered for single gap side-drives seem to be caused by lack of electrical contact between the rotor and the bearing contacted to the ground plane. This is due to a native oxide formation on the polysilicon between bearing and hub. Consequently vertical clamping of the rotor against the substrate occurs. Operation immediately after release seems not sufficient to keep the lateral contact clean of the native oxide. Maybe the side-pull force is just not high enough in side-drive motors to wear away the native oxide between hub and bearing post, which may be achieved by a comb-drive design.

Another effect should play in the favor of comb drives concerning the vertical substrate clamping. Comb-driven structures could be levitated over the substrate [tan]. This effect is due to the image charges mirrored in the ground plane, provided this last element is properly contacted to the movable comb part. This effect has actually been observed in the testing of our side-drive motors, in sect. 5.3.5.

2.3 Variable-capacitance top-drive wobble motors [1]

Starting from the very principle of cylindrical wobble motors (WM), the concept of planar, vertically wobbling electrostatic micromotors is presented. Formulas for kinematics, torques and dynamics are proposed. Finally some realistic numerical applications are presented and discussed.

2.3.1 Introduction

As we have seen, for all above presented designs of direct-driven motors, the electrostatic attraction between the salient rotor and stator electrodes intended to be aligned to each other also causes significant friction retarding torque. Harmonic wobble motors use just these high friction forces to generate torque.

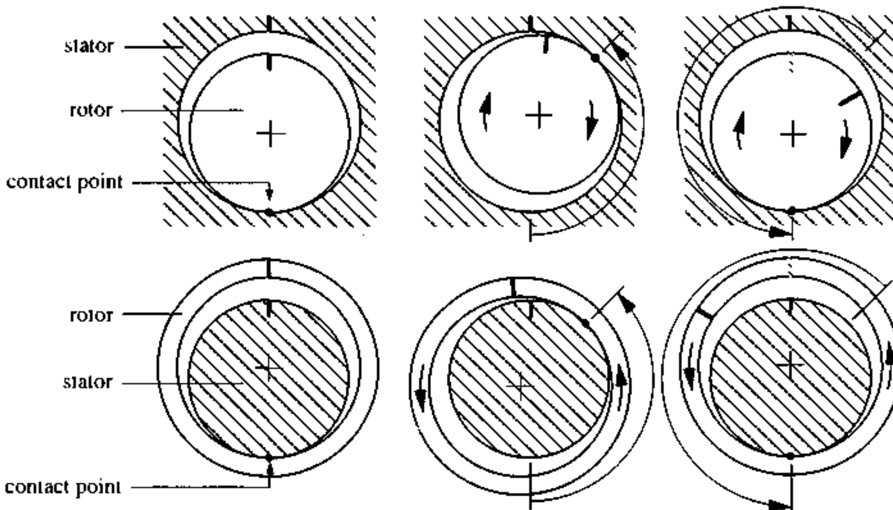

Fig. 2.19 Principles of cylindrical harmonic wobble motors. Top: inner rotor WM, where the rotor turns in opposite sense to the contact point. Bottom: outer rotor WM, where both rotor and contact point rotate in the same sense.

The basic principle of a wobble motor, here of the cylindrical type, is shown in Fig. 2.19. The rotor rolls without slipping on a path of different diameter, resulting in a differential, reduced rotation of the first one. If the radius of the rotor (R) is smaller than that of the rolling path (R_S), the contact point and the rotor rotate in opposite senses (Fig. 2.19, top) [jac]. If on the contrary the rotor rolls on a stator of smaller diameter, both rotor and

[1] Part of this work is published in [par 3, 4 and 6]

contact point rotate in the same sense (Fig. 2.19, bottom) [meh3]. The harmonic reduction ratio h is defined as

$$h = \frac{\text{rotor output speed}}{\text{contact point speed}} = \frac{R - R_S}{R} \quad (2.40).$$

The ratio h is very small when R_S is close to R. For proper output, the wobbling motion of the rotor may be transformed into a rotation, e.g. by means of some flexible links between the rotor and the output shaft. The implementation of such an output coupling mechanism represents a critical issue for wobble motors. Therefore, this aspect should be possibly taken into account already at the conception stage. The name "harmonic" refers to "harmonic drive", the term used in mechanics for a reduction stage between input and output shafts using the same rolling principle. Hence this motor is sometimes simply referred to as harmonic motor, or more generally as wobble motor (WM).

2 3.2 *Principle (patented)*

Similarly to one of its electromagnetic dual [aue], the electrostatic wobble motor design proposed hereafter is vertically wobbling and has a planar architecture (Fig. 2.20). Its basic principle, in association with planar microfabrication technologies, has been patented in the frame of the present work [par7]. As for the direct top-drive motor, this design takes a maximum advantage from the planar process since its variable capacitors can be larger compared to other planar designs [meh4]. Therefore it can be named either *top-drive* WM or *planar* WM.

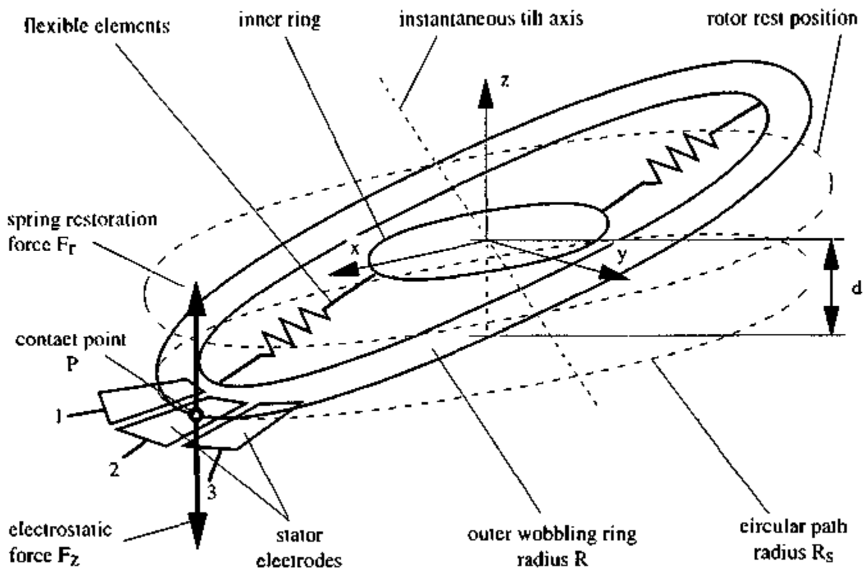

Fig. 2.20 Operation principle of the planar surface-micromachined WM.

A thin solid isolation layer covers the stator electrodes. The rotor is electrically conductive, and is composed of an outer wobbling ring of radius R, offset from the base plane by the air gap length d. This ring is elastically linked to an inner ring, which is used for output and which is guided in rotation around z by a bearing (not shown). Flexible elements are designed so as to provide a higher inner-to-outer ring twisting elasticity around an instantaneous tilt axis (contained in the x-y plane) than around the z-axis.

The rotor is set to ground potential. When a sufficient voltage is supplied to one stator electrode, the rotor is attracted and tilts from its horizontal rest position down to contact the isolation over the excited electrode. If the voltage is applied sequentially to the other adjacent electrodes, the contact point P will move accordingly. The wobbling ring rolls then without slipping along the circular rolling path of radius R_S, which is slightly smaller than R. Hence, the rotor rotates in the same direction as the contact point, as in Fig. 2.19, bottom. Exactly the same motion can also be observed in the case of a coin wobbling vertically on a plane surface. Apart from the flexible rotor, there are other possibilities for coupling such motor type to a driven mechanism, as shown in Fig. 2.21. A rigid rotor may also be used.

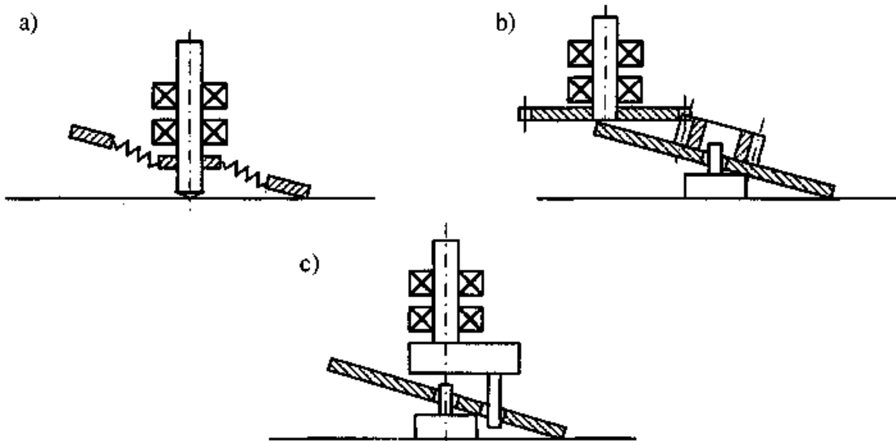

Fig. 2.21 Possibilities for power transmission from a planar WM. a) flexible rotor, b) pinion-gearwheel train, and c) crank.

2.3.3 Kinematics

The rotor kinematics are considered first, without any of the linkages shown in Fig. 2.21. All rotor movements are referenced in a 3D Cartesian coordinate system (Oxyz) attached to the stator plane and passing through the rotor center C, as shown in Fig. 2.22. Another orthogonal system (C x'y'z') is attached to the rotor. The x' axis is called the tilting axis and is parallel to the x-y plane. The y' axis is called the rocking axis and passes through points C and P.

The rolling motion of the rotor is derived from the general case of two cones rolling against each other [siv]. The disc rotor of radius R rolls without slipping like on a cone of height d (rotor offset distance) and base radius R cos α, with α being the tilt angle. If d is significantly smaller than R, then α is almost equal to d/R. The rotor trajectory can be described by the instantaneous rotation vector ω (position φ) around y', the instantaneous rocking axis. This vector ω itself rotates around z at speed Ω, the contact point angular rotation speed. Its angular position is denoted by γ. The rotor output position and speed around z are denoted respectively by δ and ω_z and depend on the type of coupling as will be seen below. Note that ω_z is not a projection of ω on the z-axis.

Fig. 2.22 Model of the planar wobble motor [par6].

If the contact point accomplishes one turn ($\gamma=2\pi$), the rotor is "shifted" around z by an angle δ. This last can be expressed as the difference between the rotor and the rolling path circumferences, divided by the rotor radius:

$$\delta = \frac{2\pi R\,(1 - \cos\alpha)}{R} \qquad (2.41).$$

The harmonic reduction ratio h can be expressed using eqs. (2.40) and (2.41) by:

$$h = \frac{\delta}{2\pi} = 1 - \cos\alpha \qquad (2.42).$$

This ratio can be very small for small values of α.

The trajectory of a point attached to the rotor rim (P') during one revolution of the contact point, is shown in Fig. 2.23. The rotation speed of P', ω_Z, hence the one of an output axle with crank as shown in Fig. 2.21 c, is not constant. Therefore, the couplings shown in Fig. 2.21 are called non-homokinetic.

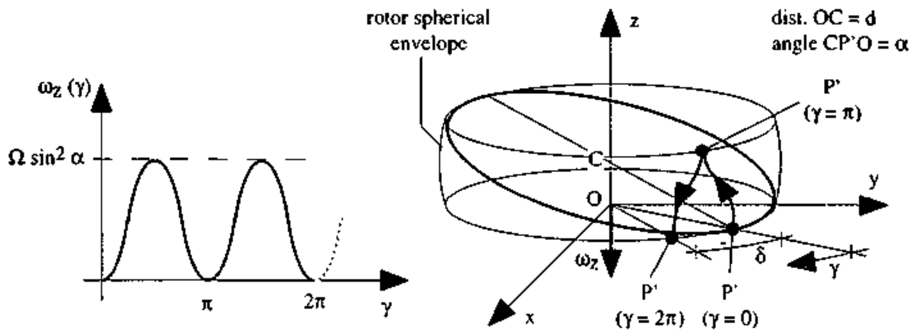

Fig. 2.23 Trajectory of one point attached to the rotor, P'. Speed of P' (ω_Z) around z.

From the vector construction of Fig. 2.22, we can write that

$$\omega = \Omega \sin \alpha \tag{2.43}$$

and

$$\omega_{Z\,max} = \Omega \sin^2\alpha \tag{2.44}$$

The average output speed of a load driven by any of the couplings shown in Fig. 2.21 is then an average value of $\omega_Z(\gamma)$ taken over one revolution of the contact point, i.e.

$$\omega_{Zav} = \frac{1}{2}\, \omega_{Z\,max} \tag{2.45}$$

It can be shown, for small values of α, that

$$\frac{1}{2} \sin^2\alpha \approx 1\text{-}\cos \alpha \tag{2.46}$$

From the last three equations, the harmonic reduction ratio h of eq. (2.42) can be retrieved:

$$\frac{\omega_{Zav}}{\Omega} \sim 1\text{-}\cos \alpha \tag{2.47}$$

2.3.4 Torques

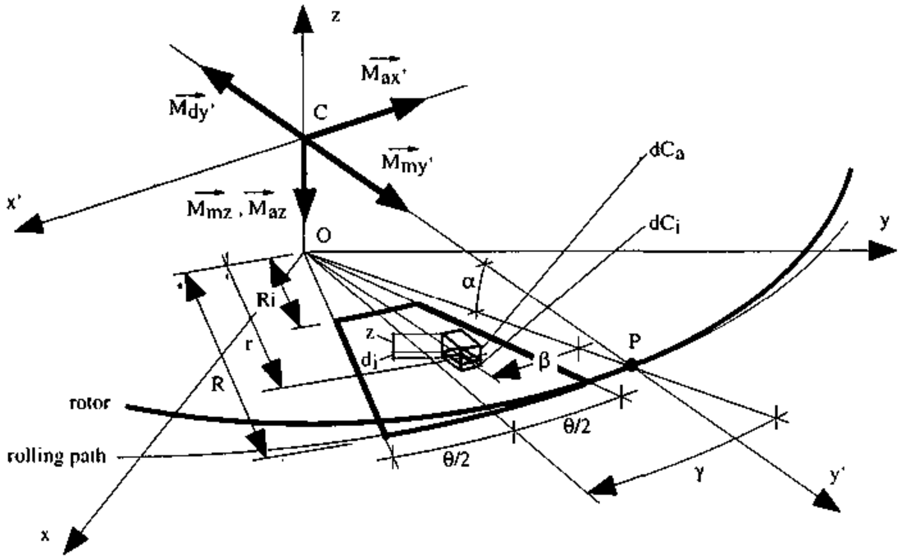

Fig. 2.24 Model for the torques calculation with one excited electrode.

Let us now consider a DC voltage V applied to one stator electrode, the rotor being grounded, as shown in Fig. 2.24. The electrostatic torques will be calculated as functions of the contact point position, γ. We denote by $M_{my'}$ the electrostatic motive torque around r, and by M_{mz} the electrostatic average (because non-homokineticity) motive torque around z. If there is no slipping, we can write, using eqns. (2.43) and (2.47) :

$$M_{mz}(\gamma) = M_{my'}(\gamma) \frac{\sin \alpha}{1-\cos \alpha} = M_{my'}(\gamma)\ k_{lo} \qquad (2.48),$$

where k_{lo} denotes the torque multiplication factor. For small values of α, k_{lo} tends to $2/\alpha$. The maximum allowable motive torque before the rotor slips under an external load torque M_{lz} is called adherence torque and denoted by M_{az}, and is given by

$$M_{az}(\gamma) = \mu\, M_{ax'}(\gamma) \qquad (2.49),$$

where μ is the dry friction coefficient between the outer rotor rim and the isolation layer, and $M_{ax'}(\gamma)$ the electrostatic adherence torque around the x' axis.

To calculate the motive and adherence torques, we may consider the variable capacitances. We have an inclined variable air gap capacitor, C_a, in series with the capacitor

formed by the isolation, C_i. As for the direct-drive motors, the fringing fields are neglected. The field being not homogeneous over their surfaces because of the rotor inclination, we shall consider small elementary capacitors dC put in parallel, in which the field is considered homogeneous. Because α is small, the field lines are assumed to be perpendicular to the substrate [bra].

We can write:

$$\frac{1}{dC} = \frac{1}{dC_a} + \frac{1}{dC_i} = \frac{z + d_i/\varepsilon_r}{\varepsilon_0\, dA} \qquad (2.50),$$

were z denotes the air gap length, ε_r and d_i resp. the dielectric constant and the thickness of the isolation layer and dA the surface of the elementary capacitor. The vertical electrostatic attraction force dF exerted by one elementary capacitor, for a fixed γ, is equal to the derivative of its stored energy w.r.t. z, as expressed by

$$dF = \frac{1}{2} V^2 \frac{\partial dC}{\partial z} = \frac{1}{2} V^2 \varepsilon_0 \frac{dA}{\left(z + d_i/\varepsilon_r\right)^2} \qquad (2.51).$$

The surface element dA and the gap length z can in turn be expressed as functions of the polar coordinates β and r respectively as:

$$dA = r\, dr\, d\beta \qquad (2.52),$$

$$z = d\left(1 - \frac{r}{R} \cos\beta\right) \qquad (2.53).$$

Using the three last equations, the elementary force dF can be expressed as

$$dF = \frac{1}{2} V^2 \varepsilon_0 \frac{R^2}{d^2} \frac{r}{\left(R\,(1 + d_i/d\,\varepsilon_r) - r\cos\beta\right)^2}\, dr\, d\beta \qquad (2.54).$$

The motive torque around r is obtained by summing up all dF elements, multiplied by their lever arm around r, over the electrode surface, as expressed by the following integrals:

$$M_{my'}(\gamma) = - \int_{r=R_i}^{R} \int_{\beta=\gamma-\theta/2}^{\gamma+\theta/2} r \sin\beta\, dF(r,\beta) \qquad (2.55).$$

Similarly, the adherence torque around x' is obtained by

$$M_{ax'}(\gamma) = \int_{r=R_i}^{R} \int_{\beta=\gamma-\theta/2}^{\gamma+\theta/2} r \cos\beta\, dF(r,\beta) \qquad (2.56).$$

Using eqs. (2.48), (2.49) and (2.54-56), one can compute numerically the motive and adherence torques around z. Fig. 2.25 gives the result for the case of the electroplated wobble motor with a 2 mm diameter rotor, as described in Table 2.2, sect. 2.3.6. The maximum motive torque is limited by rotor adherence and thus indicated by the bold continuous line. Averaging this motive torque over one step (45 degrees) we obtain 2.03×10^{-10} Nm/V^2 (finer, dashed line), or 1.1 μNm under 75 V excitation.

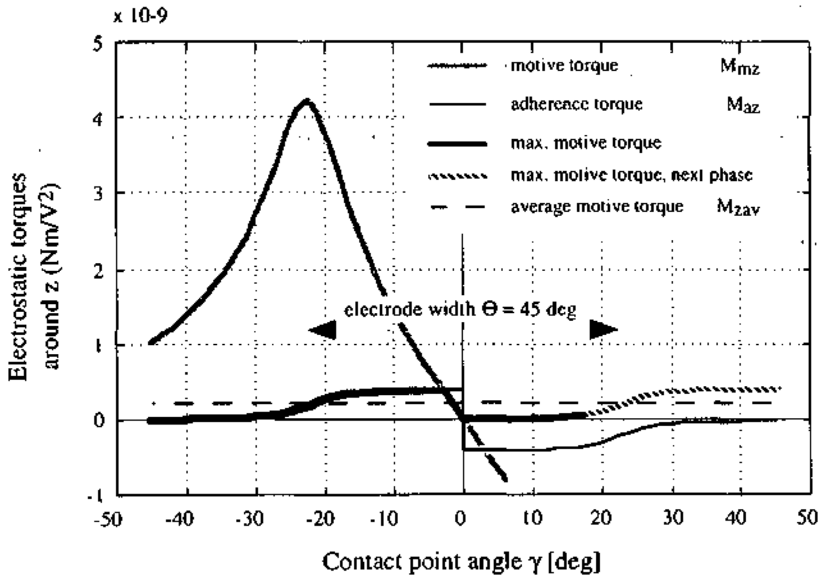

Fig. 2.25 Calculated electrostatic torques (voltage-normalized) as a function of the contact point position y along the activated electrode, for the 2 mm diameter rotor of Table 2.2.

There is almost no torque coverage between two adjacent phases: this may be sufficient to accelerate the free rotor, but in case of load, another switching sequence must be used. For this numerical figure, we can also see that the adherence torque is much lower than the available motive torque, which limits considerably the actuator performance. This situation can be improved by switching a larger number of adjacent narrow electrodes instead of one wide electrode at a time [ler].

2.3.5 Dynamics

We consider now a square wave signal sequence applied to the electrodes (Fig. 2.26). At any time, one stator electrode is excited and all others are grounded; the rotor is also grounded. At low frequencies, the rotor will oscillate around each step equilibrium position, at the middle of the activated electrode (Fig. 2.26 a). We have the well-known case of a damped spring-mass mechanical oscillator, where the spring is the electrostatic torque, and

the air is the damper. The oscillation frequency ($f = 1/T_{osc}$) and attenuation duration (T_{att}) depend on the rotor inertias, the air drag and electrostatic torques. If the excitation frequency ($1/T_{exc}$) is increased, the rotor may still be oscillating when the next phase is activated ($T_{osc} > T_{exc}$). In this case, either the rotor speed is in the same (positive speed, Fig. 2.26 c) or in the opposite (negative speed, Fig. 2.26 b) direction. Negative speed switching causes the rotor to stop or to slide, whereas positive speed switching results in a "smooth" rolling. The extreme "smooth" rolling case is when the step mechanical response time is roughly equal to the imposed switching period (Fig. 2.26 d). At higher frequency, the rotor will not start from rest. This dynamic behavior has been confirmed by qualitative observations and measurements on a similar, electromagnetic "dual" model having a 40 mm diameter iron rotor. The same characteristic is known for variable reluctance, direct-drive stepper motors [juf].

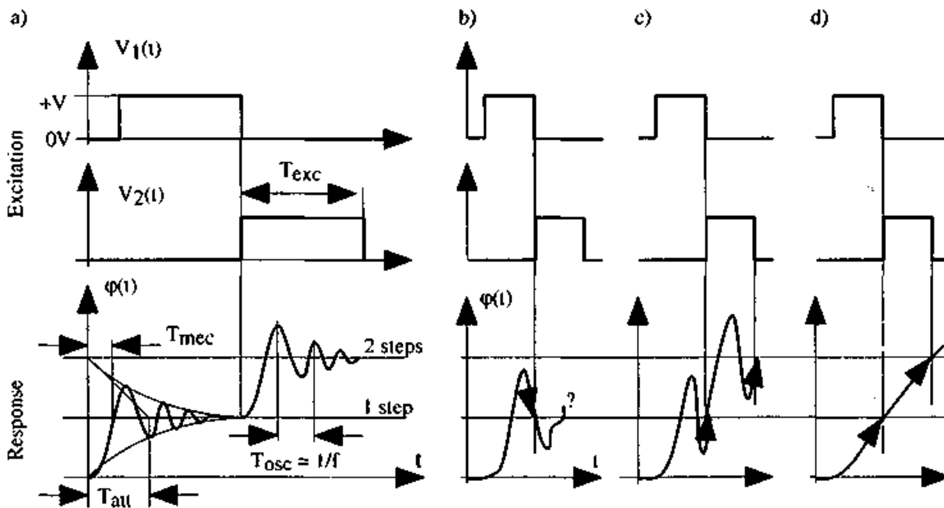

Fig. 2.26 Step response of the wobble motor. a) Low frequency excitation, $T_{osc}<T_{att}<T_{exc}$, b) High frequency, $T_{osc}>T_{exc}$, negative speed switching, c) identical than b) but positive speed switching, and d) positive speed switching before mechanical cutoff, $T_{mec}\sim T_{exc}$.

In order to evaluate the maximum attainable frequency, hence the maximum mechanical power of the electrostatic motor under these switching conditions, a dynamic model has to be made as follows.

The rotor inertias around z and y' are respectively given by

$$I_z = \frac{1}{2} m R^2 \qquad (2.57)$$

and

$$I_y = m\left(\frac{R^2}{4} + \frac{t^2}{12}\right) \qquad (2.58),$$

where m and t are respectively the rotor mass and thickness. In our case, if we assume to have $t << R$, the thickness term in eq. (2.58) can be neglected. Thus, I_z is about $2\,I_{y'}$. Moreover, eq. (2.48) gives the speeds ratio as $\omega_{zav} = \omega / k_{to}$. Again, we assume to have a small angle, hence k_{to} is much higher than 1 (see eq.(2.48)) and consequently $\omega_{z\,av} << \omega$. One can then compute the rotational kinetic energy for both axis ($I\,\omega^2/2$), and see that the energy around z is negligible compared to the energy around y'. In addition, the air drag effect on the rotor is only determining around the rocking axis, because of the rotor geometry and the low speed ratio cited above. It follows that the rotor dynamic behavior can be approximated with the Newton's 2nd law only around y' as given by

$$I_{y'} \frac{\partial^2 \varphi}{\partial t^2} = M_{dy'} + M_{my'}(\varphi) \quad (2.59),$$

where $M_{dy'}$ denotes the air drag torque.

Considering the unusual rotor motion, the air drag term is difficult to estimate and only experimental data or appropriate finite element modelling of the air flow could outline the important effects. To keep the present model as simple as possible, the squeeze film effect is neglected because the approaching surfaces are not parallel ($\alpha \neq 0$) and a major part of the rotor disc surface is open (annular rotor).

We shall consider only the air flow around the rotor along z, which maximum speed is 90 degrees apart each side from the middle of the activated electrode. The flow at these locations is either laminar or turbulent. The limit between these two domains will be evaluated in a worst case figure, as follows. We first calculate a maximum linear speed figure at these rotor locations when no air damping takes place. As can be seen in Fig. 2.25, the electrostatic output torque is nearly linear w.r.t. γ between $-\theta/2$ and $+\theta/2$. Hence the motive torque around y' can be written within these boundaries as

$$M_{my'}(\varphi) = -c_{es} V^2 \varphi \quad (2.60)$$

where c_{es} denotes the voltage-normalized electrostatic spring stiffness. To express $M_{my'}$ as a function of φ, the following variable change had to be made (see eq. (2.43) and Fig. 2.21):

$$\gamma = \frac{1}{\sin \alpha} \varphi \quad (2.61).$$

The differential eq. (2.59) has in this case a solution of the kind

$$\varphi(t) = \varphi_0 \sin(\omega_0 t) \quad (2.62),$$

$$\text{with} \quad \omega_0 = \sqrt{\frac{c_{es} V^2}{I_{y'}}} \quad (2.63).$$

The maximum speed at the rotor extremity v_{max} is obtained by first taking the time derivative of eq. (2.62), then by multiplying the amplitude of the last by R:

$$v_{max} = R\ \varphi_0\ \omega_0 \qquad (2.64),$$

where φ_0 is the maximum rocking amplitude. Since the inertia for a given thickness is proportional to R^4 after eq. (2.58), considering successively eqs. (2.63) and (2.64) this maximum speed scales as 1/R. Hence the maximum values will occur in small rotors for a given voltage. Using eqns. (2.58), (2.63), (2.64), and calculating the electrostatic spring stiffness c_{es}, we obtain a maximum speed of 3.3 m/s for the 200 µm diameter polysilicon rotor as described in table 2.2 below. To evaluate the limit between turbulent and laminar flow, we can compute the Reynolds's number [ros] with

$$N_R = \frac{\rho\ l_f\ v}{\eta} \qquad (2.65),$$

where ρ and η denote respectively the specific mass and the viscosity of air, and l_f the flow limit boundaries or object length. Using eq. (2.65), we obtain a Reynolds's number of 4.7 for the following input values: $\eta = 1.8 \times 10^{-5}$ kg/ms, $\rho = 1.3$ kg/m^3 (air at 20°), $v = 3.3$ m/s and $l_f = 20$ µm. This Reynolds's number value being far below the usually encountered turbulent limits for most bodies [ros], we assume in our case a laminar flow and thus the air drag term of eq. (2.59) can be written as

$$M_{dy'} = - f \frac{\partial \varphi}{\partial t} \qquad (2.66),$$

where f denotes the viscous damping factor.

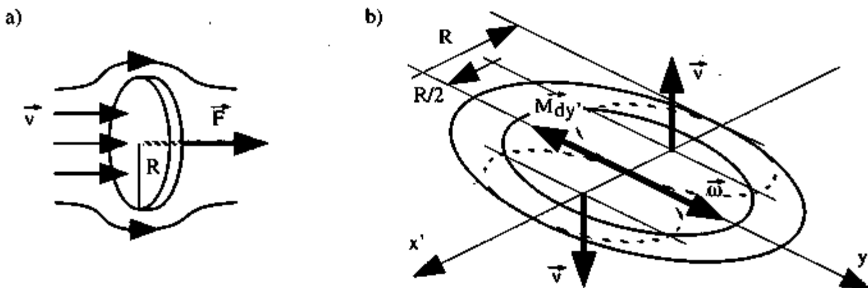

Fig. 2.27 Viscous drag torque model for the rotor oscillation motion. a) disc in a normal fluid flow, b) drag torque for an annular rotor approximated with two such discs.

A very rough value of f can be computed using the formula for the viscous drag force experienced by a circular disc placed perpendicularly in a flow, as shown in Fig. 2.27 a), and expressed by:

$$F = 16 R \eta v \tag{2.67}$$

where R denotes the disc radius, η the viscosity and v the flow speed. We assume that the viscous drag torque experienced by the annular rotor around y' is roughly equivalent to the one of two discs of radius R/2, disposed as shown in Fig. 2.27 b). Applying eq. (2.67) to this case, we obtain

$$f = 4 R^3 \eta \tag{2.68}$$

The differential equation (2.59) of the rotor movement has to be solved numerically considering the nonlinear angle-torque characteristic over one step (see Fig. 2.25). The solution will resemble somewhat to the response $\varphi(t)$ depicted in Fig. 2.26 a). Hence, the maximum contact point speed for a motor with n_s stator electrodes is given by

$$\Omega_{max} = \frac{2\pi}{n_s T_{mec}} \tag{2.69}$$

where T_{mec} denotes the mechanical response time of the rotor, i.e. the time necessary for the contact point to travel from standstill at the middle of one electrode to the middle of the adjacent, activated electrode (Fig. 2.26). Hence, the maximum mechanical output power (around z), using eq. (2.47), is given by

$$W_{mec\,max} = \omega_{z\,av\,max} M_{z\,av} = (1 - \cos\alpha)\, \Omega_{max} M_{z\,av} \tag{2.70}$$

where $M_{z\,av}$ denotes the average motive torque over one step (dashed line in Fig. 2.25).

2.3.6 Calculated performances

The electrostatic torques (eqs. (2.55-56)), the differential equation of the movement (2.59) and the one of the maximum output power (2.70) are evaluated numerically hereafter, for two different wobble motors likely to be fabricated with the silicon-based planar processes (see fabrication). The first one has a 200 μm diameter flexible gimbals rotor and is fabricated with the polysilicon process (see Fig. 4.5 left and [par 2,3]). The second one is realized with the nickel electroplating process, in larger rigid rotor diameters of 1, 2 and 3 mm (spoked rotors of Fig. 4.27, [par6]). The input parameters and results are given in table 2.2. A dedicated computer program has been written to perform all the calculations ("ESMOTOR" on MATLAB).

Table 2.2 Planar wobble motor parameters and calculated performances.

all motors: air viscosity = 1.8×10^{-5} kg/ms at 20°C, excitation voltage = 75 V, friction coefficient = 0.5, isolation layer: silicon nitride of 0.2 μm and with $\varepsilon_r = 6$.

motor type:			**Poly ø 200 μm**	**Ni ø 1 mm**	**Ni ø 2 mm**	**Ni ø 3 mm**
rotor (input):						
specific mass	ρ	[kg/m^3]	2300	8900	8900	8900
outer radius	R	[mm]	0.1	0.5	1	1.5
inner radius	R_i	[mm]	0.08	0.3	0.8	1.3
thickness	t	[μm]	1	15	15	15
stator (input):						
electrode width	θ	[°]	20	45	45	45
electrode number	n_s		12	8	8	8
open air-gap distance	d	[μm]	1	10	20	30
reduction ratio	h	[1]	1/20'000	1/5000	1/5000	1/5000
performances (output):						
aver. mot. torque	M_{zav}	[μNm]	0.048	0.383	1.14	2.13
visc. damping factor	f	[10^{-13}Nms]	0.0007	0.09	0.72	2.4
response time	T_{mec}	[μs]	0.27	61	150	252
max. output speed	$\omega_{zav\,max}$	[rad/s]	97	2.58	1.05	0.62
max. mec. power	$W_{mec\,max}$	[μW]	4.66	0.99	1.20	1.32

The results of the calculations show that the millimeter-sized nickel motors deliver about one microwatt of power. The mechanical power increases with size for the nickel motors. A somewhat surprising result is the larger amount of power delivered by the 200 μm diameter polysilicon motor. One reason for this discrepancy is that this motor is not homothetic to the three others, and has a different rotor specific mass. Its very fast response time corresponds to a maximum drive frequency around 3 MHz, which is most challenging for up-to-date high voltage drivers. Therefore, these extreme and unexpected values should not be taken for granted before any practical measurement.

The calculated step responses $\varphi(t)$ are quasi-undamped when taking the f values as listed in the table, calculated using eq.(2.68). Even with a viscous damping factor of 10^{-11} Nms, i.e. about two orders of magnitude higher, the oscillation is largely underdamped (Fig. 2.28). This question is treated further in the test chapter.

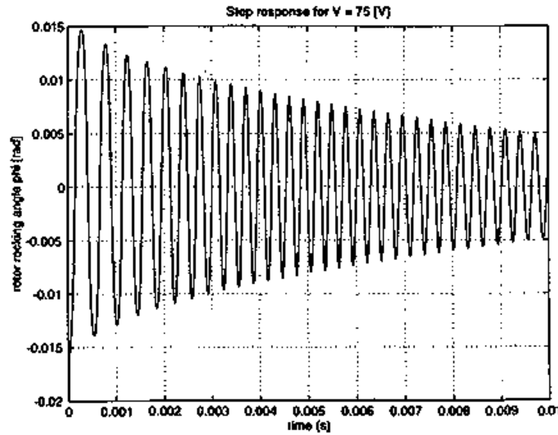

Fig. 2.28 Calculated step response φ(t) of the 2mm spoked nickel motor with the parameters as given in table 2.2, and with a viscous damping factor of 10^{-11} Nms (instead of 7.2×10^{-14} Nms). The mechanical response time is T_{mec} = 150 µs.

2.3.7 *Flexible gimbals rotor* [1]

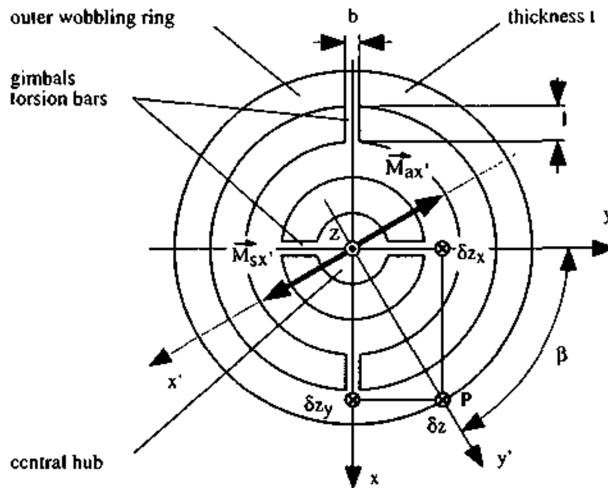

Fig. 2.29 Model of a flexible rotor with elastic gimbals suspension.

A possible construction for a flexible rotor (Fig. 2.21 a) consists in the arrangement of flexible torsion bars between an inner rotating hub and the outer wobbling, rigid ring (Fig. 2.29). This kind of suspension permits a preferably lower tilting (about the x' axis) than

[1] Part of this work is published in [par5]

rotation flexibility (about the z-axis) between central hub and wobbling ring. When the rotor is tilted against the substrate, the spring restoration torque (due to the torsion bars) must be ideally negligible compared to the electrostatic adherence torque, so that possibly a large amount of the electrostatic energy can be converted into rotary output work. To ensure this, the spring torque $M_{sx'}$, must be evaluated and compared to the electrostatic adherence torque about this same axis, $M_{ax'}$ (Fig. 2.24).

In the following modelization, only the four torsion bars are assumed to be deformed under pure torsion. The torsion spring constant of one bar is given by [roa]

$$k_{sp}\ [\mathrm{Nm/rad}] = \frac{KG}{l} \qquad (2.71),$$

with

$$K = \frac{b}{2}\frac{t^3}{8}\left(\frac{16}{3} - 3.36\,\frac{t}{b}\left(1 - \frac{t^4}{12\,b^4}\right)\right) \qquad (2.72),$$

and

$$G = \frac{E}{2\,(1+\nu)} \qquad (2.73),$$

where K is a torsion form factor, dependent on the dimensions of the cross-section, assumed rectangular of width b and thickness t. G denotes the modulus of rigidity, l the bar length, E the Young's modulus and ν the Poisson's ratio. The spring restoration torque around x' can be decomposed into its x and y components as given by

$$M_{sx'x} = M_{sx'}\cos\beta \qquad (2.74)$$

and

$$M_{sx'y} = M_{sx'}\sin\beta \qquad (2.75)$$

where β denotes the angular position w.r.t. the torsion bars location. The amplitude of deflection of the rotor rim at P, δz, is given by

$$\delta z = \delta z_x + \delta z_y = R\ (\alpha_x\cos\beta + \alpha_y\sin\beta) \qquad (2.76),$$

where δz_x, δz_y and α_x, α_y denote the z-displacements and tilt angle around resp. the x and y axis. The torques are related to the bar spring constant by

$$M_{sx'x} = 2k_{sp}\,\alpha_x \qquad (2.77),$$

and

$$M_{sx'y} = 2k_{sp}\,\alpha_y \qquad (2.78).$$

By equating eq. (2.77) with eq. (2.74), and eq. (2.78) with eq. (2.75) and solving for $\alpha_{x,y}$, and by replacing these values into eq. (2.76), one finally obtains the expression of the spring torque

$$M_{sx'} = 2k_{\varphi}\frac{\delta z}{R} \tag{2.79}$$

We can see that this torque is independent of β, the force application location w.r.t. the torsion bars location. The tilt spring constant is hence uniform over the whole rotor, and has a value of 2k. It is possible to calculate the static pull-out voltage, i.e. the voltage at which electrostatic adherence and spring forces around s are equal, i.e. that

$$M_{sx'} = M_{ax'} \tag{2.80}$$

The right member of this equation can be expressed as a product of the voltage squared by the torque normalized to the squared voltage, $m_{ax'}$. Solving w.r.t. the voltage, and using eqs.(2.79) with $\delta z = d$ (the open air-gap distance), and eq. (2.71), the pull-out voltage is obtained:

$$V_{po} = \sqrt{\frac{2\,KG\,d}{l\,R\,m_{ax'}}} \tag{2.81}$$

A very acceptable pull-in voltage as low as 6V is calculated using this equation, for the following numerical figure (electroplated flexible rotor): $\vartheta = 45°$, $R_i = 0.8$ mm, R = 1 mm, d = 20 µm, $d_i = 0.34$ µm, $\varepsilon = 6$ for silicon nitride [sze1], $G = 8.1\times10^{10}$ N/m^2 (nickel: $E=21\times10^{10}$ N/m^2 and $\nu = 0.3$ for metals [kur]), torsion bars: l = 200 µm, b = 50 µm and t = 10 µm. These parameters are then used for the fabrication of the rotor (see fabrication).

Chapter 3 - Friction [1]

3.1 Introduction

As shown in chap.2, the dry friction in the bearings of electrostatic micromotors is a determining, important parameter. Moreover, the top-drive motor has theoretically better static performances than the side-drive motor, if the dry friction coefficient at the bushings is typically 0.1 (sect. 2.2.5). This motivates to know friction coefficients values.

Many groups have worked for in-situ characterization of friction. Tai and Muller obtained dynamic, dry friction coefficient values between 0.21 to 0.38 for polysilicon on nitride, by fitting starting and stopping rotor positions of side-drive micromotors to a model [tai1, 2]. Gabriel et al. found coefficients between 0.25 to 0.35 for polysilicon on silicon, by fitting the deceleration of air-spun microturbines [gab2]. By modelling the step transient of electrostatic side-drive micromotors and subsequent fitting to experimental data, Bart et al. [bar2] determined values between 0.26 and 0.4 for polysilicon on itself (Fig. 2.9). Fisher and Tomizawa [fis] report a value of 0.80 for hot-pressed silicon nitride (Norton NC-132) on itself, in laboratory air with a pin-on-plate friction machine and under 0.5 to 2 GPa mean contact pressures. These pressures are much higher than encountered in electrostatic motors, as the calculation hereafter will show. The same authors also report the influence of humidity, which causes the formation of highly hydrated amorphous silicon oxide through tribochemical reaction at the wear location. Unknown adsorbed species may also hide the intrinsic material friction values. These adsorbates result from uncontrolled environment or inadequate cleaning.

The above mentioned, in-situ measured values are roughly concurring and already give a good indication for silicon-derived micromachined bearings. Still, a particular bearing design and operating conditions and environment determine entirely the bearing tribological context. Moreover, for a practical friction characterization in a design phase, an alternative test to motor data fitting must be used, possibly made under the same conditions as for the future bearing. The materials likely to be used in the process can then be directly compared.

A pin-on-disc measurement method for the evaluation of dry friction coefficients between centimeter-size silicon samples covered with thin films has been used, as described hereafter. One material for reducing the friction is proposed and investigated.

[1] Part of this work is published in [par1]

3.2 Friction conditions of the polysilicon motors

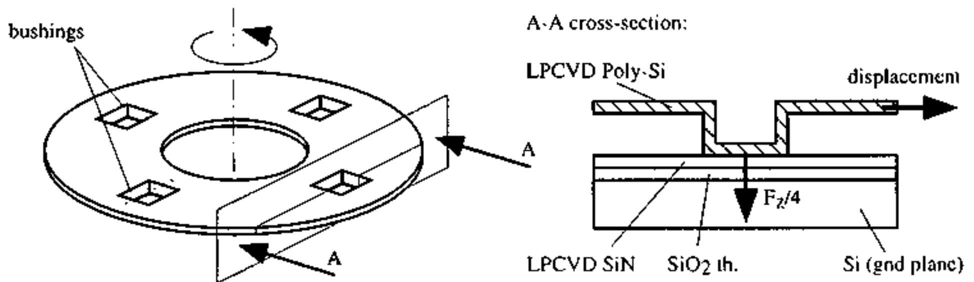

Fig. 3.1 Model of the bushing friction of the bearing.

The measurement is chosen as close as possible to the friction conditions of the 200 μm diameter top-drive motor bearing (Figs. 2.11, 3.1, 4.3, [par1]). The actuation pressure is exerted vertically on the bushings. The lateral friction can be neglected as long as no lateral load is demanded. The friction materials are LPCVD Poly-Si against LPCVD SiN (sect. 2.2.5). Poly-Si against itself is also considered. The four bushings size 8 x 8 μm^2. Under 50 V DC (aligned position), the rotor is pulled against the substrate with 2.7 μN. The contact pressure per bushing is then 10.5 kPa. The friction force F_f is assumed to be independent of the apparent contact surface area, i.e. that

$$F_f = \mu_{s,d} N \qquad (3.1),$$

where N is the normal load and $\mu_{s,d}$ the static or dynamic friction coefficient. Test surfaces topographies, flatnesses and histories must be similar to the motor's. A rotor speed of 600 rpm is chosen, which corresponds to a sliding speed of 3 mm/s. The conditions are: normal air ambient, atmospheric pressure, 20 to 25°C and 35 to 50 RH (Relative Humidity).

3.3 Measurement set-up

A pin-on-disc machine (Tribometer, CSEM) has been employed (Figs. 3.2, 3.3). The upper sample is a 4.7 x 4.7 mm^2 Si chip covered with a thin film of a material 1 (pin). The lower sample is an approx. 40 x 40 mm^2 part of a 3" Si wafer covered with a film of material 2 (disk). The upper sample, free to tilt inside its holder, is pressed with a known vertical force N against the lower sample. A weight of 100 g is placed to give an apparent contact pressure of 45.3 kPa, calculating with the upper sample area. This is about four times the estimated pressure in the motor. The lower sample is mounted on a turntable, which rotation axis is offset from the upper sample axis by a distance r = 15 mm.

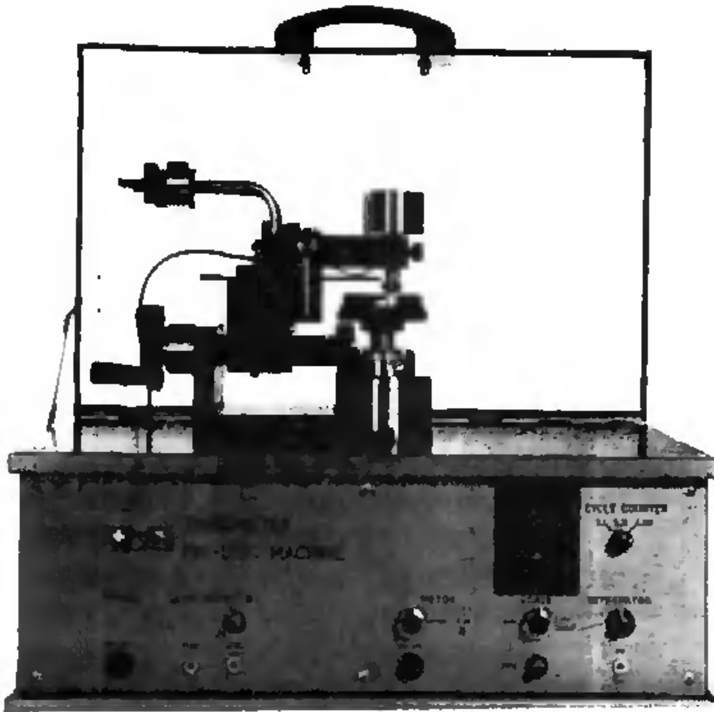

Fig. 3.2 Pin-on-disc machine (Tribometer from CSEM S.A.)

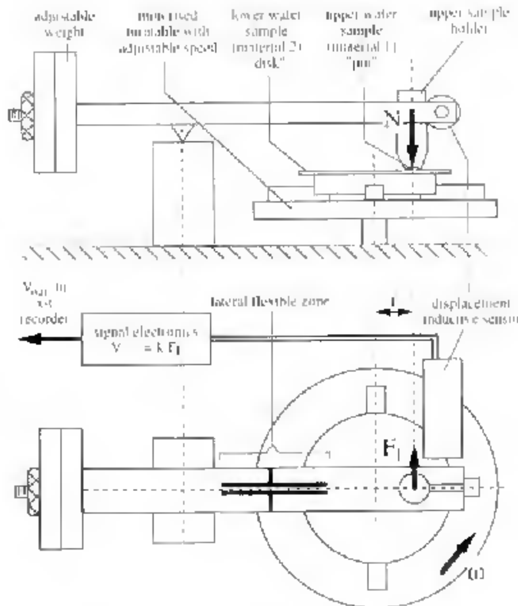

Fig. 3.3 Schematics of the tribometer of Fig. 3.2.

When the turntable is rotated, the upper sample experiences the friction force Ff which bends the arm laterally. The arm deformation is measured by an inductive displacement sensor. Appropriate electronics deliver a voltage proportional to the force, which can be plotted on an x-t recorder. As shown in Fig. 3.4, as the rotation starts, the lateral friction force increases to μ_s N, the static friction value, until slipping occurs. During rotation, the friction is dynamic, of average value μ_d N. The maximum test sliding speed of 3 mm/s is reached for a turntable rotation speed of 2 rpm.

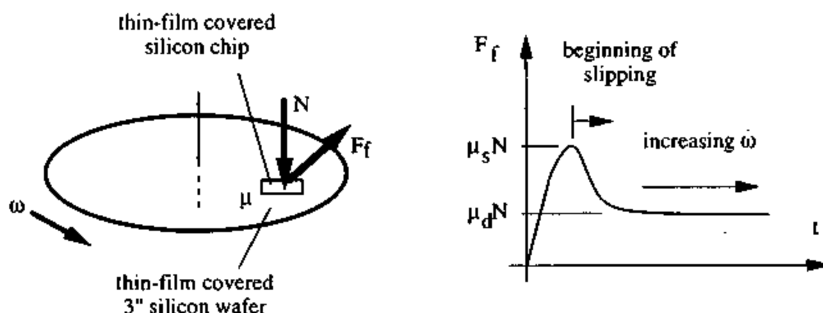

Fig. 3.4 Measurement principle.

3.4 Test samples preparation

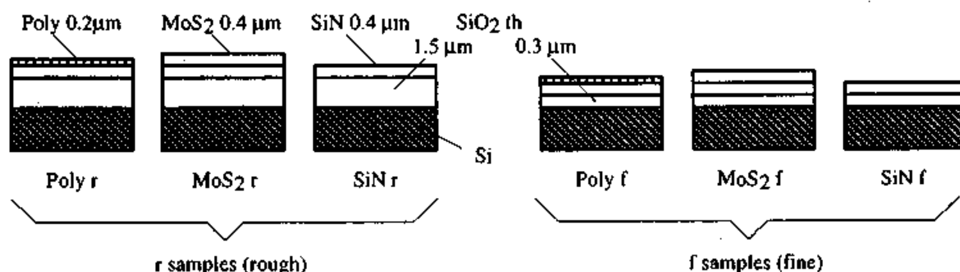

Fig. 3.5 Samples used for the pin-on-disc friction measurements.

The test samples have been prepared to measure the friction of LPCVD polysilicon on itself, LPCVD silicon nitride on LPCVD polysilicon, LPCVD silicon nitride on itself and molybdenum bisulfide (MoS_2) on itself (Fig. 3.5). The films were deposited over two different thermal oxide thicknesses, to assess a possible roughness or thickness dependency of the friction ("r" or "f" prefix).

Molybdenum bisulfide is a commercially available solid lubricant (Microslide® from CSEM [mos2]) used namely for space applications. Because of its hexagonal lamellar microstructure, similar to the one of graphite, the friction between two MoS_2 covered surfaces

cause the MoS_2 lames to be oriented along the sliding directions. It has a quite low hardness (1-2 Mohs) and is sensitive to humidity. MoS_2 against steel has a friction coefficient of 0.01 to 0.04 in dry air and vacuum, and of 0.2 to 0.3 in humid air (RH>50%).

The silicon wafers (ø 3", 380 μm thick, or. 100, p-type, one side polished, 5-7 Ωcm) are first standard cleaned to remove organic matter and uncontrolled native oxide, and to grow a very thin uniform thickness of passivating oxide (see process sect. 4.1.1, step a). Thermal oxidation is then performed at 1100°C with 4l/min of 80°C water steam, to form 1.5 and 0.3 μm of silicon dioxide. The 4000 Å of silicon nitride are then deposited by LPCVD, at 230 mtorr and 800°C by reacting 20 sccm dichlorosilane ($SiCl_2H_2$) with 60 sccm ammonium (NH_3), at a growth rate of 3330 Å/h. On some of the wafers, 2000 Å of polysilicon are then deposited by LPCVD, at 220 mtorr and 600°C by reacting 20 sccm silane (SiH_4 100%), at a growth rate of 3000 Å/h. On other wafers, a layer of 4000 Å MoS_2 is deposited by PVD (by CSEM [mos2]). Some of the polysilicon samples have been re-cleaned using the standard silicon cleaning, to assess possible dependency of the friction on the presence of native silicon oxide. These wafers/samples are cited as poly "cl", like "clean". The wafers are then cut into samples of appropriate dimensions with a wire saw, and glued with a 100°C paraffin on adequate metal adapters, which fit into the turntable and the upper sample holder.

Prior to testing, all samples except the MoS_2 are cleaned with acetone and isopropanol, and dried with nitrogen. As reported in [fis], the acetone, which is not of high purity, may leave lubricating impurities by evaporation. Therefore, the acetone is washed by isopropanol of high purity before the drying.

3.5 Results

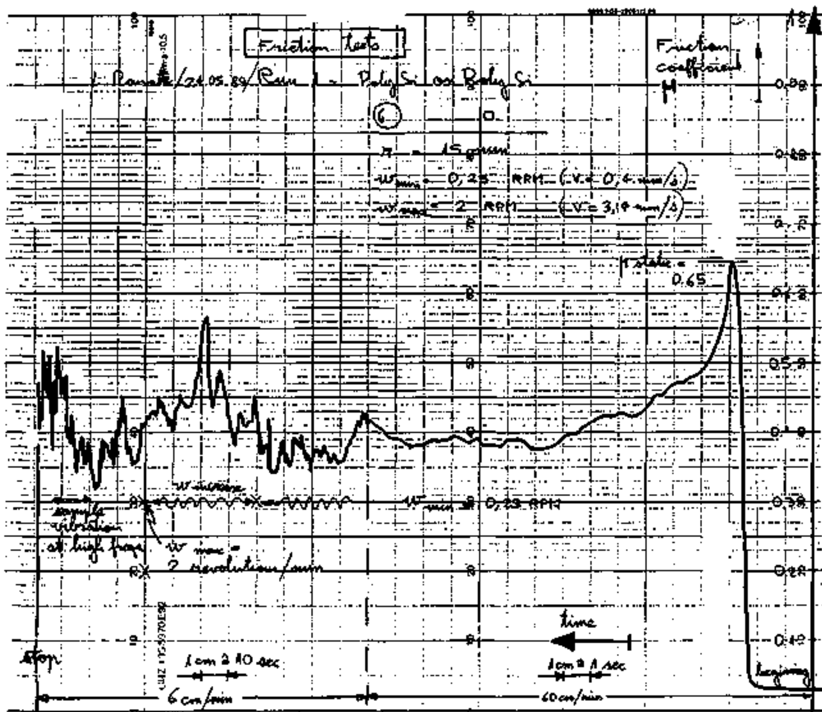

Fig. 3.6 Typical x-t plot of the friction coefficient (here poly against poly).

Fig. 3.6 shows a typical x - t plot of the friction coefficient. The friction coefficient axis (vertical) is calibrated by hooking the load of 100 g laterally to the upper sample holder, by means of a thread and a pulley, and by adjusting the plotter gain so that the full scale value of one is read. After the installation of the samples, the turntable is started by slowly increasing the speed from standstill to 0.5 rpm, during which the first slipping occurs. After one revolution, the speed is increased to the maximum test sliding speed of 2 rpm. After five revolutions, the turntable is automatically stopped. The resolution over the μ axis (vertical) is ± 0.01.

A total of 29 runs of dry static and dynamic friction measurements have been carried out in ambient air at 20°C. The results are listed in Table 3.1. The relative humidity was not controlled and varied between 35 to 50 % RH, and was measured for each run with a precision of ± 0.5.

Table 3.1 Measured dry friction coefficients (dynamic and static) between thin-film covered silicon samples at 20°C in air using the tribometer.

	run no	class no	RH (%)	film 1	film 2	surface	μ stat	μ dyn	avg.μ dyn ± S.D.
1	1	1	48.0	Poly	Poly	fine	0.25	0.2	0.225
2	2	1	46.0				0.26	0.25	
3	3	2	46.0	Poly	Poly	rough	0.25	0.23	0.225
4	4	2	44.0				0.25	0.22	
5	28	3	37.0	Poly clean	Poly clean	fine	0.31	0.28	0.265
6	29	3	36.0				0.32	0.27	
7	30	4	37.0	Poly clean	Poly clean	rough	0.48	0.3	0.363
8	31	4	35.0				0.52	0.5	
9	32	4	35.0				0.31	0.29	
10	18	5	35.0	Poly	SiN	fine	0.31	0.31	0.35 ± 0.06
11	19	5	35.0				0.34	0.31	
12	20	5	35.0				0.41	0.39	
13	21	5	34.5				0.51	0.45	
14	22	5	34.0				0.31	0.29	
15	10	6	38.5	Poly	SiN	rough	0.39	0.25	0.36 ± 0.17
16	11	6	36.0				0.26	0.5	
17	12	6	38.0				0.36	0.6	
18	13	6	38.0				0.27	0.27	
19	14	6	37.0				0.17	0.16	
20	15	6	36.0				0.27	0.35	
21	25	7	38.0	Poly clean	SiN	rough	0.55	0.45	0.36 ± 0.10
22	26	7	37.0				0.45	0.38	
23	27	7	36.0				0.29	0.25	
24	7	8	46.0	MoS2	MoS2	fine	0.32	0.26	0.28 ± 0.02
25	8	8	45.0				0.32	0.29	
26	6	9	47.0	MoS2	MoS2	rough	0.36	0.32	0.32
27	16	10	36.0	SiN	SiN	rough	0.48	0.55	0.55
28	17	10	36.0				0.33	0.55	
29	23	11	36.0	SiN	SiN	fine	0.26	0.4	0.40

In many runs, the recorded μ_d value was very unstable, hence an average value is taken. A probable cause of these fluctuations may be random changing of the contact points locations occurring between the flat samples, which in turn varies the level arm and the contact nature. In most runs, the sharp edges of the upper sample (chip) ground visible scars into the disc when the speed was increased from 0.5 to 2 rpm. The moment of appearance of the scars coincidences with a strong increase of μ_d. This undoubtedly indicates local piercing of the film on the disc, rendering this part of the graph insignificant. Consequently, most of the values of μ_d listed are measured before the grinding, at 0.5 rpm (= 0.75 mm/s). For a same run, the value of μ_d being not very stable over that speed range, a graphical average value is taken. In the rare cases where ground samples had to be re-used, they were thoroughly rinsed with acetone and isopropanol. Dust particles, breath humidity and stick-slip also caused grinding at 2 rpm. In some runs, audible sample vibration (around 100 Hz) revealed stick-slip. This phenomenon always happens when μ_d is smaller than μ_s and when one of the bodies in contact is mounted on an elastically undamped spring. If necessary, this problem can be avoided by adding a damping mechanism [ish].

In some runs, periodical variations of μ_d with a period corresponding to one turntable revolution were observed. This happened because the disc was by accident mounted not

parallel to the rotation axis normal plane, and that the ability of the upper sample to tilt inside its holder was not very effective. In these cases again, an average value over one period is taken.

The 0.4 μm MoS_2 layer showed early grinding and bad adhesion, as shown by wear particles generated during the test. It was found that PVD nucleation deposits of MoS_2 having approximately 50 μm in size were responsible for grinding. A metal sample coated in the same PVD run did not exhibit such deposits. We conclude that this phenomenon is inherent to the sample material, here LPCVD silicon nitride. Nevertheless, the values of μ_d are not as high as when traversing scars are ground, thus the measured values are taken into account.

The sample grinding during the tests allowed to evaluate the relative hardness of the materials in presence. Hence, it has been observed that nitride is harder than poly, which is harder than MoS_2.

3.6 Interpretation

Table 3.2 shows the average values for same material combinations, disregarding their surface finish (smooth or rough) and the cleaning method used for the polysilicon samples (Poly and Poly cl). Because of the low number of runs of the two last combinations, their S.D.'s must be considered as indicative.

Table 3.2 Dry friction measurements regrouped in classes of similar materials. (a) = no diminution after slipping for some runs, (b) = unstable/increasing during slow rotation for some runs, (c) = same as (b), but for all runs.

class #	materials	number of runs	%RH	μ_s±S.D.	μ_d±S.D.
1,2,3,4	Poly on Poly	9	40.5 ± 5.5	0.33 ± 0.10	0.28± 0.09
5,6,7	SiN on Poly	14	36.5 ± 1.5	0.35 ± 0.10 (a)	0.35±0.12 (b)
8,9	MoS_2 on MoS_2	3	46 ± 1	0.33 ± 0.02	0.29±0.03
10,11	SiN on SiN	3	36 ± 0	0.36 ± 0.11	0.50±0.09 (c)

We can see that the average values of Table 3.2 are within the range of the early in-situ measurements of the works mentioned in the introduction. There is no significant difference between Poly on itself and Poly on SiN, their S.D.'s causing the values to overlap. Surprising is also that a same, polycrystalline material (Poly) on itself produces a lower coefficient than SiN on Poly. It would be hazardous to quantitatively compare rows 1 and 2 with rows 3 and 4, because of the large difference in the number of runs. Nevertheless, SiN on itself has a higher μ_d then the other combinations, and higher μ_d than μ_s values in all runs, and thus seems not to be a good sliding combination at a relatively low humidity.

Despite of the grinding effects, a μ_d of 0.29 is obtained for MoS_2 with a humidity of about 47 % RH. This result is close to the specifications of [mos2], mentioning a μ_d of 0.2 to 0.3 for RH > 50 %. Supplementary tests under a lower humidity are nevertheless required to obtain a confirmation.

Dependencies on humidity, surface roughness and native oxide are very difficult to assess quantitatively because of lack of data. Nevertheless, some qualitative observations between the μ_d values of table 3.1 are made hereafter.

There is no significant difference for Poly on itself, between smooth (class #1, μ_{dav} = 0.225) and rough surfaces (class #2, μ_{dav} = 0.225), but in case of Poly cl on itself, the average is lower for the smooth surface (class #3, μ_{dav} = 0.265) than for the rough surface (class #4, μ_{dav} = 0.363). Adsorbed impurities and/or uncontrolled native oxide may decrease here the dynamic friction coefficient. The standard cleaning reveals the polysilicon grains and thus offers a more rough and hard surface. Adequate samples analysis (e.g. SEM) are necessary to reinforce these hypothesis. These combined effects of cleaning and surface topography are not observed for Poly on nitride which exhibits quite close average values of 0.35 ± 0.06, 0.36 ± 0.17 and 0.36 ± 0.1 for resp. fine (class #5), rough (class #6) and cleaned rough surfaces (class #7).

To evaluate a possible relationship between humidity and friction, same material combinations can be plotted versus the relative humidity. The class #6, Poly on SiN, is the best candidate of Table 3.1, because its μ dyn. S.D., the number of runs and the humidity span are maximum. As shown in Fig. 3.7, there is no clear evidence of humidity dependency, if any. The low number of runs in other classes, as well as their small humidity range do not allow to properly assess further such dependence.

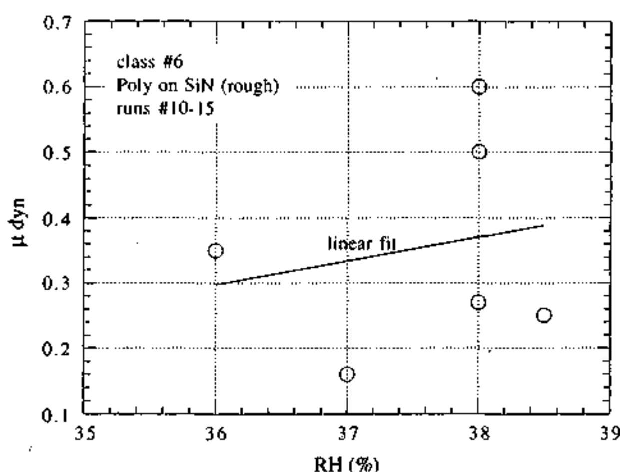

Fig. 3.7 Dynamic friction coefficient as function of the relative humidity, for polysilicon on silicon nitride (class #6 of Table 3.1).

3.7 Conclusions

Plate-on-disc friction tests between LPCVD-deposited Poly-Si and SiN, as well as PVD MoS_2 thin films on thermally grown SiO_2 have been performed in ambient air at 20°C, under 35 to 50 % humidity. Average values of static (μ_s) and dynamic (μ_d) dry friction coefficients are resp. 0.33 ± 0.10 and 0.28 ± 0.09 for Poly-Si on itself, 0.35 ± 0.10 and 0.35 ± 0.12 for Poly-Si on SiN, 0.33 ± 0.02 and 0.29 ± 0.03 for MoS_2 on itself, and 0.36 ± 0.11 and 0.50 ± 0.09 for SiN on itself. The present data for Poly-Si on itself and Poly-Si on SiN correspond to the ones found by in-situ characterization of micromotors [tai1, tai2, gab2, meh1], under an estimated apparent contact pressures in the range of 10 kPa.

The closeness of the average values and their large fluctuations (S.D.) makes it impossible to conclude for a proper material dependency of the friction coefficient, except for SiN on itself, which shows quite higher coefficients and a tendency to tribological welding. This is more or less confirmed by Fisher and Tomizawa [fis] who found for the same ambient but at much higher pressures (0.5-2 GPa) a μ_d of 0.8 for hot-pressed SiN on itself.

The μ_d value of 0.29 for MoS_2 on itself at 47 % RH corresponds to the specifications of [mos2], mentioning a μ_d of 0.2 to 0.3 for RH > 50 %. This solid lubricant should in fact be used at much lower humidity to offer lower friction coefficients. This implies a permanent humidity control, which should be avoided for the simplicity's sake of the motor. Other solid lubricants should be investigated. Characterization of carbon chains monolayers (C_{22}) already showed promising results for applications to MEMS [zar].

When standard-cleaned, rough polysilicon on itself has a higher friction coefficient than smooth polysilicon. Hence, organic impurities and/or uncontrolled native oxide may act as lubricants, which are removed through the standard cleaning. This phenomenon is not observed for cleaned polysilicon on nitride.

The effect of humidity could not be assessed in these measurements.

A pin-on-disc test configuration may be preferable to the plate-on-disc. The fluctuations of μ_d would be reduced and the problem of grinding by the sharp edges of the upper sample, avoided.

A much larger amount of runs, post-test observations (SEM) of the worn surfaces, are still needed to make a better evaluation.

Concerning wear, same materials combinations should be avoided, such as poly on itself or nitride on itself. Hence, polysilicon on nitride seems to be the best combination for the motors bushings from the point of view of wear and coefficient.

Chapter 4 - Fabrication

4.1 Integrated polysilicon motors

4.1.1 Process

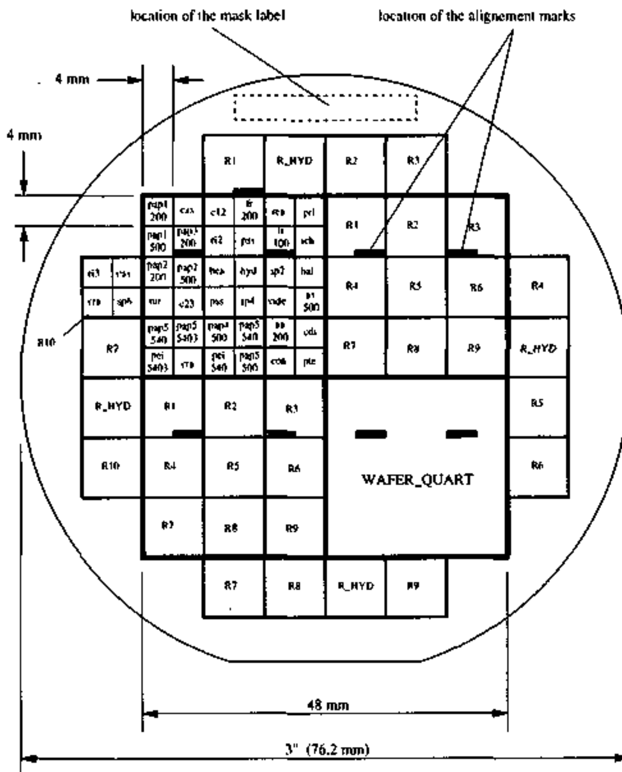

Fig. 4.1 Arrangement of the structures on the 3" silicon wafer.

The process for the polysilicon motors is mainly inspired from our surface micromachining technology (sect. 1.3., [lin1]). It has been conceived to fabricate simultaneously the four motor types, as well as various test structures. Each chip is 4 x 4 mm^2 and is either one motor or a group of test structures (Fig. 4.1). There are 83 motors and 208 chips per wafer. Figs. 4.2 to 4.5 show the motors and their cross-sections.

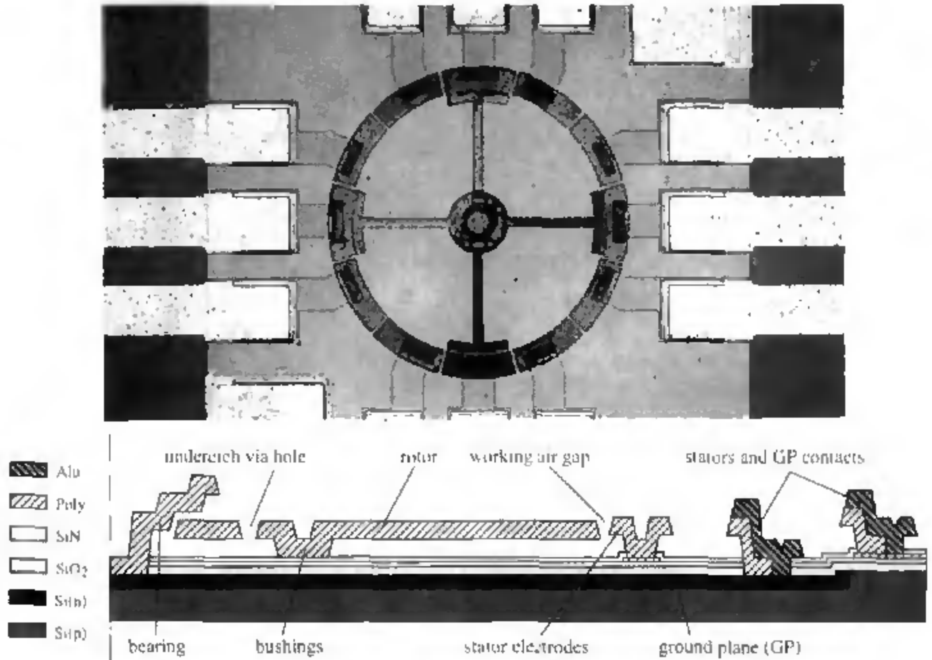

Fig. 4.2 4:12 side-drive electrostatic stepper motor (rotor ø 500 μm) and half cross-section.

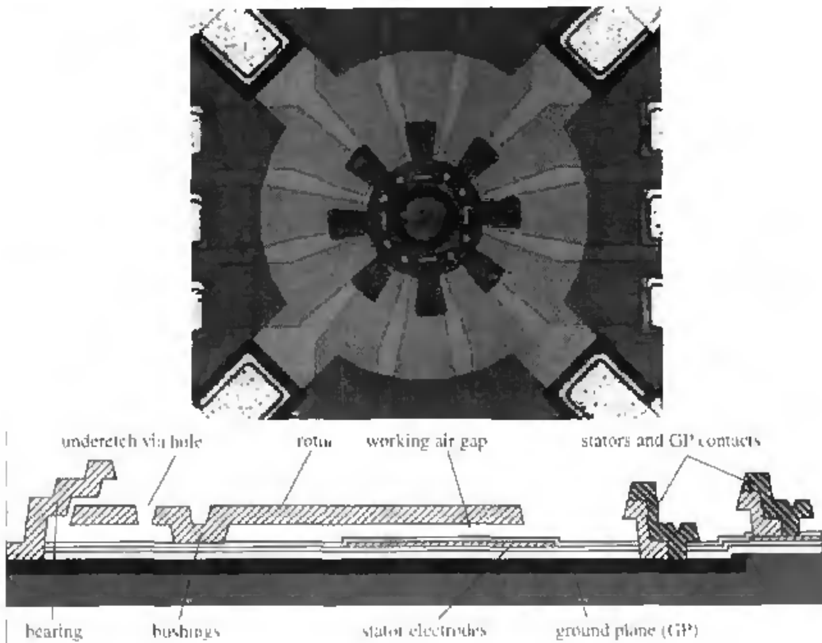

Fig. 4.3 8:12 top-drive electrostatic stepper motor (rotor ø 200 μm) and half cross-section.

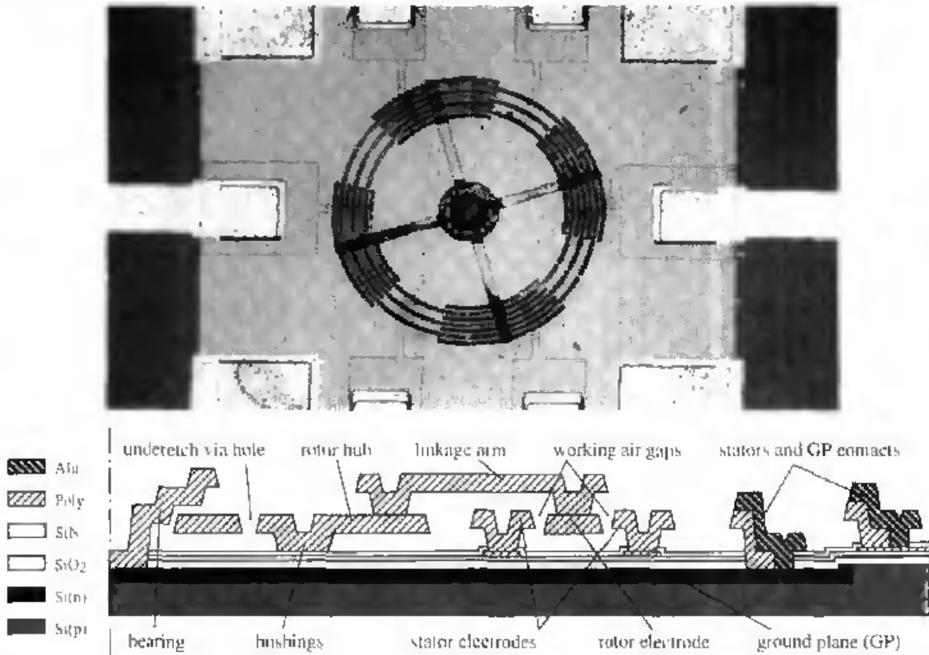

Fig. 4.4 4:6 comb-drive electrostatic stepper motor (rotor ø 540 µm) and half cross-section. For simplicity, only two stator and one rotor electrodes are shown.

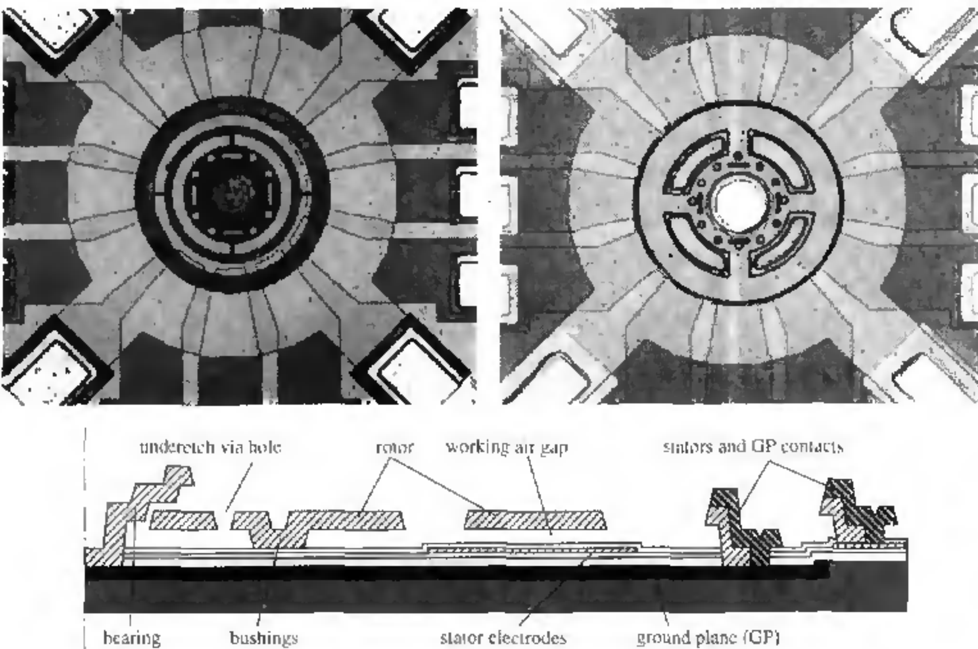

Fig. 4.5 12-pole, top-drive electrostatic, flexible gimbals wobble motor (left) and asynchronous motor (right). Both rotors are 200 µm in ø. Bottom: half cross-section.

There are three levels of conductive Poly-Si layers (0.2-1 μm). All motors have identical bearings (sect. 4.1.5). The ground plane (GP) is a n-diffusion, isolated from the rotor by a thermal silicon dioxide layer and one or two silicon nitride layers. Selective removal of sacrificial silicon dioxide is used for the rotor release (sect. 4.1.6).

The process steps, illustrated in Fig. 4.6, are described hereafter for the case of the most complex, hence representative structure, i.e. the comb-drive motor.

a) The Si wafers (3", 380 μm thickness, <100> orientation, one-side polished, p-type, resistivity = 5-7 Ωcm) are first standard cleaned: 5 mn in 100% nitric acid (HNO_3) to remove the organic matter, 30 s in 7:1 buffered hydrofluoric acid (BHF[1]) to remove native SiO_2, and finally 5 mn in 115°C HNO_3 70% to grow a uniform passivation SiO_2 (≤ 50 Å). Dry thermal oxidation is performed at 1100°C to obtain typically 3000 Å of SiO_2. The GP region is defined by opening a window in this oxide with BHF, at an etch rate of typ. 700 Å/mn (mask 1). Etch rates are found either from thicknesses measurements by ellipsometry, or from steps measurements by mechanical profilometry (Alphastep 200). N-doping of the region is performed through phosphorous-doped SiO_2 deposition, by reacting gaseous silane (SiH_4), phosphine (PH_3) and oxygen at 350°C (LTO-APCVD) followed by a 20 mn, 1100°C drive-in in neutral ambient. The oxide layer is composed of 1000 Å of phosphorous-doped oxide having 2.1 wt% (weight percent) of P, covered by 2500 Å of undoped oxide. This last prevents direct phosphorous rediffusion from the wafer during the drive-in. The obtained electrical resistance and junction depth were typically of resp. 50 Ω/square (four-points test probe) and 1.8 μm (Calotest ® from CSEM), which is acceptable for the ground plane function. The removal etching of the doping layer is done in BHF, but must be stopped before etching further the thermal oxide mask. A precise etching end-point is detected by visual inspection when looking at large (~ 2 mm^2) dummy diffusion openings. The water or BHF is repelled from these locations as soon as the silicon is revealed because silicon is more hydrophobic in contrast to silicon oxide. To sustain voltages during operation of typ. 100V between the stator electrodes and the GND plane, a field oxide of 3000 Å is thermally grown. This thickness is enough since breakdown voltages as high as 450 V have been measured on such oxide films one micron thick. Prior to this oxidation, a thin CVD oxide is deposited to form a barrier against rediffusion from the wafer. A first, low-stress (see sect. 4.1.2) silicon nitride layer of 2000 Å (SiN I) is deposited by LPCVD at 835°C and 230 mtorr, by reacting ammonia (NH_3) and dichlorosilane ($SiCl_2H_2$). This SiN I serves as etch protection for the subsequent polysilicon definition. A thin polysilicon layer of 2000 Å (Poly-Si I) is deposited by LPCVD at 600°C and 220 mtorr, by reacting SiH_4. This layer is then phosphorous-doped in the same way as for the bulk silicon (see above), but with a drive-in temperature of

[1] Our 7:1 BHF is composed of 7 parts of ammonium fluoride 40% and 1 part of hydrofluoric acid 50%, added with an anticrystallizing agent (ethylene glycol).

1050°C, leading to a resistance of 200 to 500 Ω/square, which is low enough for the application. The stator electrodes and their lands are then defined (mask 2) with a dry SF_6/O_2 plasma etching of the polysilicon, at 0.02 mbar and 90 W (Leybold Z401S). The etch rate in poly is 1400 Å/mn. The etching end point determination on the first nitride was monitored by light spectroscopy of the fluor luminescence (wavelength of F = 703.7 nm, Sophie Instruments). The end-point is detected by a rise in fluor concentration. A second LPCVD nitride layer of 2500 Å is then deposited (SiN II). This layer serves as etch protection for subsequent processing, and as electrical isolation during operation to prevent short-circuit between rotor and stator.

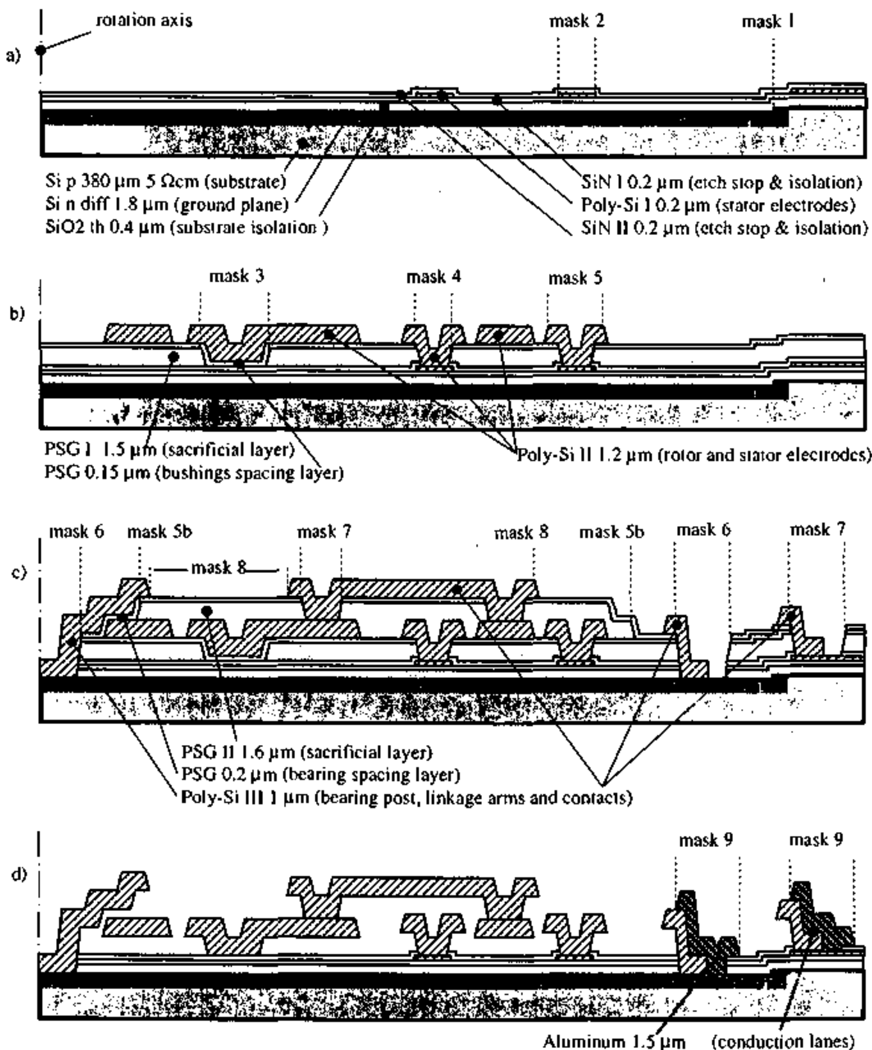

Fig. 4.6 Process sequence for the fabrication of the polysilicon electrostatic motors, here the comb-drive motor. a) Stator base, b) hub, rotor and stator. c) axle, linkage arms and contacts and d) metallization and structure release.

b) A first sacrificial phosphosilicate glass (PSG I) with a high concentration of phosphorous (4.4 wt% P) of 1.5 µm is deposited by CVD. A 1100°C reflow for 20 mn in water steam is then performed to planarize the PSG, i.e. to smoothen its surface and to eliminate the replication of the stators steps to further deposited layers (see sect. 4.1.3). The rotor bushings negatives are opened with BHF (mask 3) down to SiN II, at an etch rate of 3500 Å/min. A thin CVD oxide of 1500 Å is then deposited, in order to prevent the rotor from sticking to the second nitride when released (bushings spacing layer). To open the contacts between polys I and II (mask 4), both the PSG I and the SiN II layers must be etched. The former can be opened with BHF, but the latter can hardly be wet-etched with good precision, and the photoresist mask risks degradation since it is used twice. Therefore, an aluminum mask is used here in place of the photoresist mask. The aluminum layer (0.8 µm) is evaporated over the PSG I and patterned (mask 4) with a dry $SiCl_4/Cl_2$ plasma etching (0.1 mbar, 100 W). A very good replication precision of the aluminum is attained with this process (± 0.1µm of over- or undersize/edge w.r.t. mask). The PSG is etched in BHF down to the nitride. The photoresist is then stripped away in acetone, followed by a dry CHF_3 /O_2 plasma etching (0.03 mbar, 100 W) to open the second nitride down to the first polysilicon. The etch rates in this plasma for the nitride and the poly are quite close, with resp. 450 and 200 Å/mn. Therefore, special care has to be taken not to pierce the poly I layer. End-point detection by light spectroscopy was not possible because of the small open mask area. Thus, good control of the etch rate, combined with electrical contact verification (prober) in large openings permitted a reliable processing here. A second polysilicon layer of 1.2 µm is deposited (Poly-Si II). Prior to this deposition, the aluminum mask must be completely removed by wet etching, in order to prevent aluminum-silicon whiskers from appearing during the LPCVD run (see sect. 4.1.4). The rotor comb teeth and hub, and the stator comb teeth are defined with a dry SF_6/O_2 plasma etching (mask 5). This etch step is critical because the 2 µm wide air gaps of the side- and comb-drive motors must be defined. Therefore, an aluminum mask is used here again because its etch selectivity to polysilicon is far higher than that of the positive photoresist, and it enables a higher etch contour definition in the polysilicon.

c) A second sacrificial PSG of 4.4 wt% P and 1.6 µm is deposited (PSG II). A 20 mn, 1100°C anneal permits to simultaneously liberate the internal stress of the as-deposited Poly-Si II [lin1, guc1], render it conductive through phosphorous diffusion from the PSGs I and II, and planarize the PSG surface (see sect. 4.1.3). Afterwards, the PSG II is defined with BHF to reveal the rotor bearing holes and to remove the PSG II wherever it does not cover the rotors (mask 5b). A thin CVD oxide of typically 2000 Å is then deposited, i.e. the bearing spacing layer, to create the appropriate bearing lateral play. Sect. 4.1.5 discusses this critical point. Next, the openings to the ground plane for the bearing post and for the contacts are wet- and

plasma-etched in the same way as under b) (mask 6). The openings for linkage of all rotor comb teeth to the hub, as well as the contacts to the Poly-Si I are wet- and plasma-etched (mask 7). As before, in these two last operations, the etch end-point is verified by measures of the electrical resistance along a strip opened in these conductive layers. A third polysilicon (Poly-Si III) of 1 μm is deposited and the bearing post, the linkage arms and the contacts are patterned (mask 8) with the same plasma etching as for the Poly-Si II. A sandwich of 1000 Å of phosphorous-doped and 2500 Å of undoped CVD silicon oxides (as before) is then deposited on top (not shown). At that stage, a 1050°C drive-in is performed to dope principally the Poly-Si III through diffusion from the underlying PSG II and from the top CVD oxide.

d) The top CVD-oxide and all open-surface sacrificial PSG are removed by wet etching (not shown). An aluminum layer of 1.5 μm is evaporated and annealed at 450°C to ensure a good electrical contact with the GND plane (diffusion) and the Poly I. The conduction lanes are then patterned (mask 9) by wet-etching of the aluminum. Between each 4 mm x 4 mm chips, 100 μm (approx. 1/4 wafer thickness) profound grooves are diced to permit easy manual breaking into individual chips after the rotor release. In the same dicing run, complete separation into four wafer quarters is made (one entire pre-sawed wafer is quite fragile for subsequent manipulation and transportation). Finally the rotor is released through wet etching of the remaining sacrificial PSG, in 7:1 BHF for 1 hr (see sect. 4.1.6). The metallized surfaces are protected in this last step by photoresist. Microscope observations after this step reveal that some of the rotors are rotated due to the strong fluidic forces present in the etch and rinse baths, attesting the successful rotor liberation.

Figs. 4.7 to 4.10 show SEMs of a successfully released and rotated comb-drive motor of 540 μm rotor diameter. In Fig. 4.7, a faint, dark cross phantom image printed in the substrate still reveals the fabrication position of the rotor. Most free-standing elements of the structure, i.e. the comb teeth and the linkage arms, have a very good planarity, as shown in Figs. 4.8 to 4.10. The slight vertical deflections of the rotor arms are explainable by the out-of plane deformation of the bearing, induced by rotation jamming (see sect. 4.1.5).

Still on their quarter wafer dies, the liberated rotors are then submitted to a coercition test with a prober needle, to evaluate the mechanical rotor freedom. Afterwards, the wafer quarters are separated into individual chips, and the successfully rotated motors are mounted on a PCB and bonded as shown in Fig. 4.11 in view of the electrical actuation tests (see test, chapter 5).

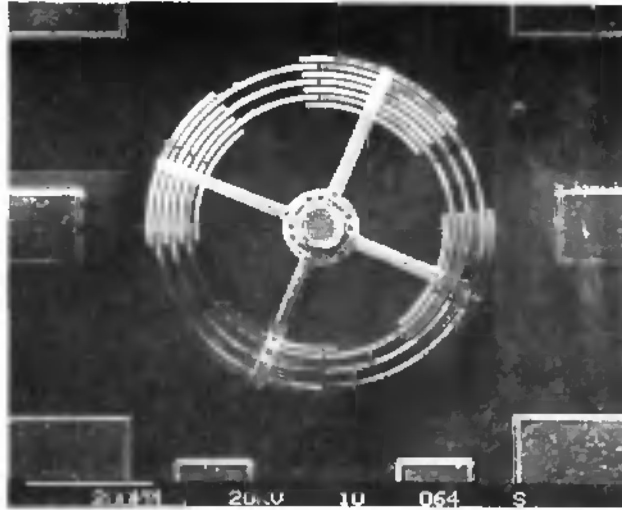

Fig. 4.7 SEM top view of a successfully released comb-drive motor (rotor ø = 540 μm). The fabrication position is still visible (dark, phantom image of the four linkage arms).

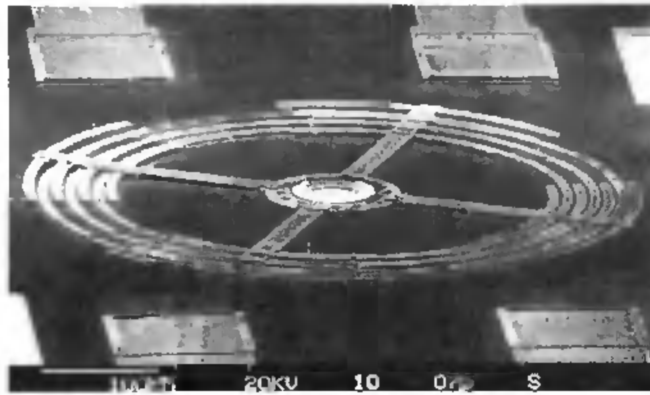

Fig. 4.8 SEM perspective view of the comb-drive motor of Fig. 4.7.

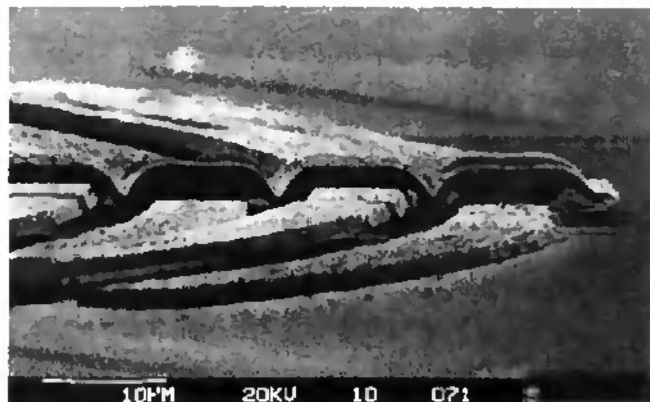

Fig. 4.9 Enlarged SEM of Fig. 4.8, right, showing the four last comb teeth.

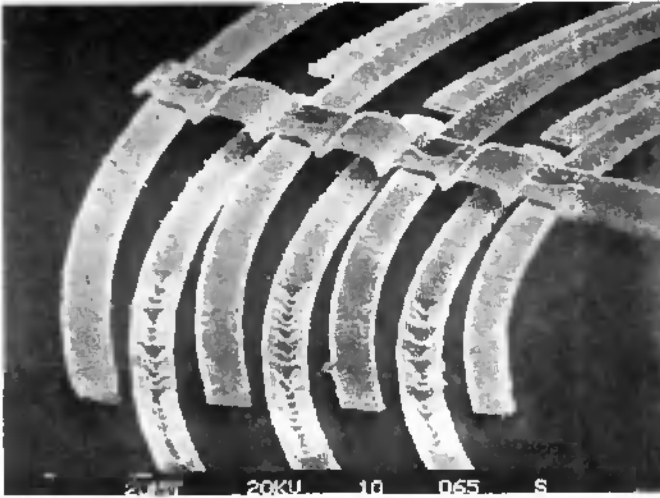

Fig. 4.10 Enlarged SEM of Fig. 4.8 showing one group of 7 rotor and stator comb teeth

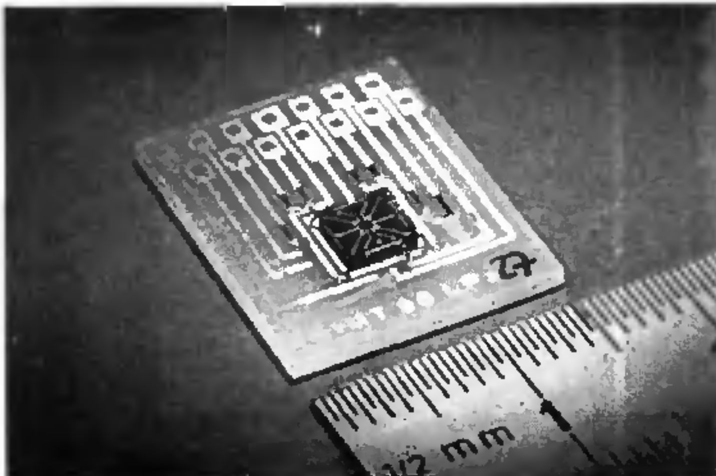

Fig. 4.11 Motor chip (4 mm x 4 mm) mounted on a PCB and bonded, ready for the electrical actuation tests. Because of its small diameter of 540 µm, the rotor, located in the center of the chip, is not visible.

4.1.2 Low-stress silicon nitride

As mentioned, the LPCVD silicon nitrides I and II serve as etch-stop for subsequent processing. Additionally, the SiN II film has to withstand the one hour liberation BHF etching. In the first process runs, we observed cracks in the silicon nitride layers, revealed by the BHF etching of the underlying thermal oxide, as shown in Fig. 4.12. Our standard nitride is stoechiometric (Si_3N_4) and was deposited at 800°C and 230 mtorr, with ammonia and dichlorosilane flows of resp. 60 and 20 sccm. Our observation is confirmed by [gue0]

reporting that stoechiometric films are in strong tension, and that consequently the film may break. In fact, bare silicon wafers having only one layer of stoechiometric silicon nitride broke frequently under normal manipulation. The same author also reports that "High dichlorosilane/ammonia gas ratios produce silicon-rich films, which exhibit compressive strain fields". An appropriate gas ratio may then be found to obtain low-stress nitride, as reported by [sek]. We changed our depositions conditions according to this last author. In this case, no signs of stresses appear; but after a long (one hour) BHF 7:1 etch, small circular spots indicating again underetching of the thermal oxide revealed the presence of pinholes in the nitride surface (~20 holes/mm^2). The final solution to this problem was to deposit the low-stress nitride sandwiched between two 300 Å stoechiometric nitride layers. No signs of cracking nor pinholes were visible after 1 hour BHF etching of samples realized with this process.

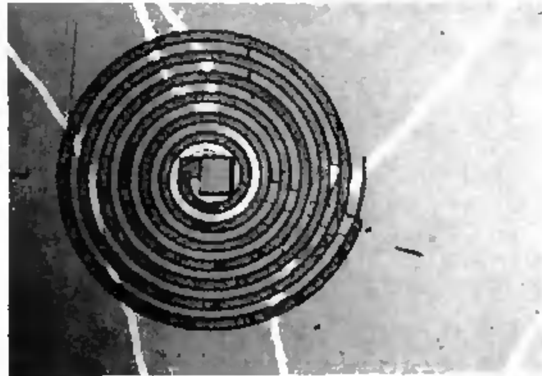

Fig. 4.12 Crack lines in the SiNs I and II, revealed by underetching of the thermal oxide during the long BHF release etching of this test spiral (poly II 1 µm thick, ø approx. 240 µm, beam width 10 µm). Note the cross clamped under the spiral at right.

4.1.3 Planarization of PSG

Fig. 4.13 Typical, non-conformal step coverage (polysilicon) by as-deposited AP LTO-CVD PSG (phosphorous-doped SiO_2) [sze].

As-deposited micrometer-thick APCVD films are generally non-conformal (their thickness is not constant over steps), they have granular surfaces [arm]. The step coverage is self-shadowing (Fig. 4.13, [sze1, p. 361]). The adequate formation and definition of the

polysilicon layers II and III depend mainly on the morphology of the underlying CVD PSG layers I and II. Fig. 4.14 shows the comb motor linkage arm attachment point to the bearing, a result of a former process version. Clearly visible is the granular aspect of the as-deposited PSG II, propagated to the LPCVD poly III, the surface of which becomes bubbly. Note also the non-conformal covering of the sharp edge of the poly II (not visible) by the PSG III. The worst case happens at places where all four layers are stacked, e.g. where the linkage arms cross the stator electrodes (Fig. 4.6 c). Important surface roughness of the polysilicon elements of the motor may lead to point discharge effects during motor operation, whereas non-conformal step coverage renders subsequent film deposition and patterning difficult.

Fig. 4.14 SEM showing an enlarged view of the attachment point between linkage arm (Poly III, black) and rotor bearing (PSG II, white) in a former version of the process (comb-drive motor). Note the granular aspect of the as-deposited PSG.

A planarization of the PSG layer is thus needed. This operation can be achieved by a high-temperature reflow of the PSG, as described in [sze1, arm]. Typically, the samples are "heated in steam at 1100°C for 20 mn". The PSG "becomes soft and flows upon heating". PSG reflow tests over the nearly vertical step of Fig. 4.13 at the above cited conditions, and having various phosphorous concentrations (0 - 7.2 wt%, weight percent P) are reported in [sze1]. The higher the phosphorous concentration, the lower the softening point and lower the slope of the PSG surface over the step. The effects of phosphorous concentration, ambient, heating time and temperature are reported elsewhere [arm]. In particular, it is cited that steam ambient gives a lower viscosity to the PSG than a nitrogen ambient and that the annealed PSG surfaces become very smooth.

The reflow method has been used in our process. Samples have been prepared for preliminary reflow tests. The PSG deposition is performed at 350°C (LTO) in an APCVD reactor by reacting silane, phosphine and oxygen according to the following reactions:

$$SiH_4\,(g) + O_2\,(g) \xrightarrow{350^\circ C} SiO_2\,(s) + 2H_2 \qquad (4.1),$$

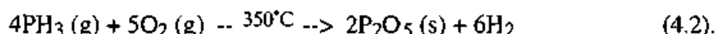

$$4PH_3\,(g) + 5O_2\,(g) \xrightarrow{350^\circ C} 2P_2O_5\,(s) + 6H_2 \qquad (4.2).$$

If the reactor is saturated with oxygen and if the balance of the above reactions is set to the right (all input products react), the proportion SiO_2:P_2O_5 depends only on the input flow rates of silane and phosphine. Therefore, the concentration of P in the dioxide can be calculated, using the two equations above and the flow rates, with the following equations:

$$\text{wt\% (P)} = \frac{\text{weight (P)}}{\text{weight (Si, P, O)}} = \frac{31\,r_c}{71\,r_c + 60} \qquad (4.3),$$

$$\text{with } r_c = \frac{[PH_3] \times \text{input flow } PH_3}{[SiH_4] \times \text{input flow } SiH_4} \qquad (4.4),$$

where the brackets indicate the volumic concentration of the gases. However, this calculated wt% of P is only indicative here because it is not confirmed by direct analysis.

Table 4.1 LTO-APCVD deposition parameters of the PSG samples used for the reflow tests (deposition temperature = 350°C, Ar flow = 12 l/mn, N_2 flow = 10 l/mn).

	gas flow (ml/mn)					CVD	
sample #	SiH_4 2 %	PH_3 1000 ppm	O_2 100 %	P* (wt%)	PSG thick. (Å)	dep.time (mn)	dep.rate (Å/mn)
4D11	695	840	73	2.9	5200	5	1040
4D12	"	1320	"	4.4	5800	5	1160
4D13	200	840	21	8.7	2500	5	500
4D7	695	840	73	2.9	11'000	9	1220
4D8	"	1320	"	4.4	10'500	9	1170
4D9	360	840	43	4.4	6000	9	670

*calculated after the gas flows

Deposition of PSG with various gas flow rates has been made on six samples (see Table 4.1). The first three samples (4D11-13) are silicon substrates used to determine the PSG deposition rate and conditions. The three last samples (4D7-9) had a 1.4 μm LPCVD polysilicon layer, in order to create similar topographic conditions as in the motor process,

and were subsequently reflown. The PSG thicknesses and refractive index are measured by two-angle ellipsometry with a 633 nm laser beam. A refractive index of 1.47 ± 0.02 and a growth rate of 1150 ± 70 Å/mn are obtained (4 samples 4D11,12,7,8). Samples 4D13 and 4D9 exhibit a lower than normal deposition rate, indicating probably a too low amount of silane or oxygen. After the deposition, the samples 4D7-9 are heated at 1100°C for 20 mn, under neutral ambient (N_2 at 4l/mn). The PSG having 2.9 wt% of P did not reflow over the step, but its surface is somewhat smoother (Fig. 4.15). The PSG having 4.4 wt% of P did reflow, and its surface is much smoother (Fig. 4.16): the reflown step coverage has a positive, finite slope, which is favorable for subsequent layer deposition and patterning. These results are very comparable to the observations of [sze1, arm].

a)

b)

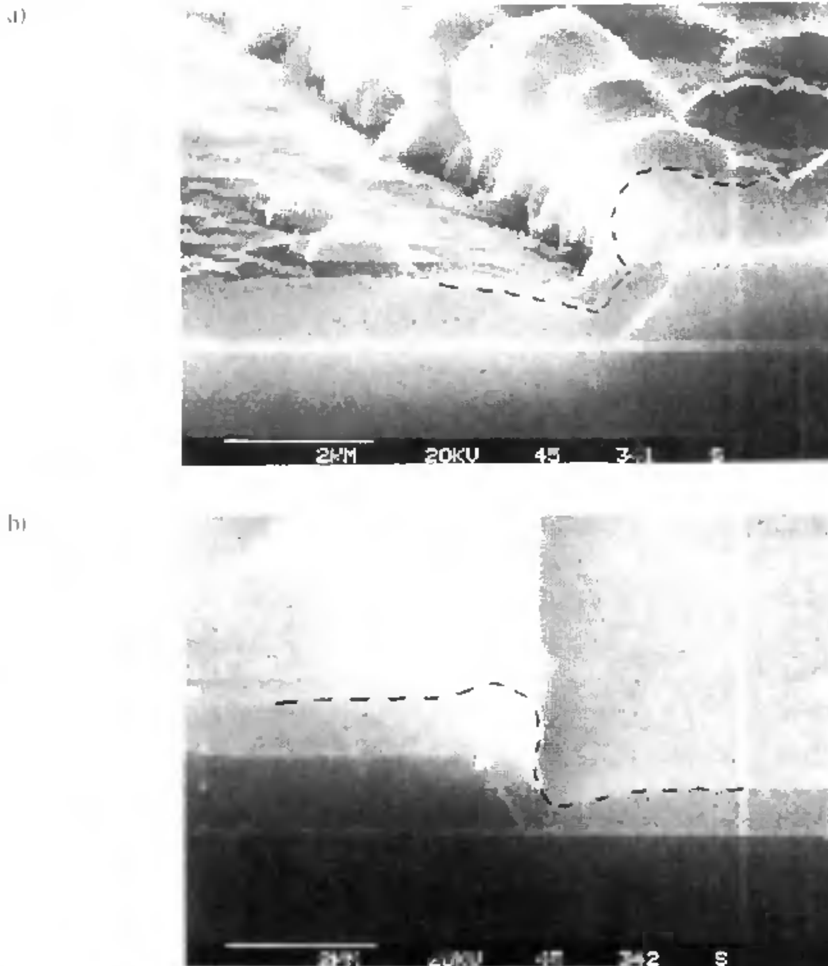

Fig. 4.15 SEM of a PSG layer having a calculated 2.9 wt% P deposited over a polysilicon step (sample #4D7 in Table 4.1). a) As deposited, and b) After annealing at 1100°C for 20 mn in steam under 4l/mn of nitrogen flow.

a)

b)

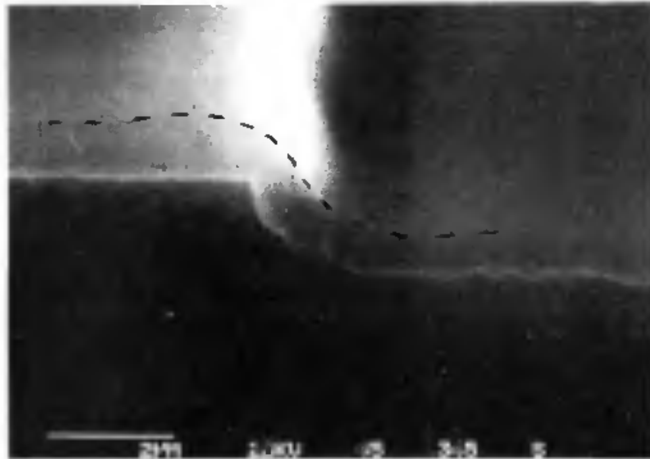

Fig. 4.16 SEM of a PSG layer having a calculated 4.4 wt% P deposited over a polysilicon step (sample #4D8 in table 4.1). a) As deposited, and b) After annealing at 1100°C for 20 mn in steam under 4l/mn of nitrogen flow.

The ideal deposition and reflow parameters illustrated in Fig. 4.16 have thus been used for the PSGs I and II of the motor process. The worst case figure, where the linkage arms of the comb-drive motor cross the stator and rotor electrodes, is schematized in Fig. 4.17. Apart from the problems of roughness amplification, the rotor-stator air gaps are not completely filled because of the self-shadowing effect. Depending on the steepness of the poly II sidewall, the step may even not be covered by the PSG. The remaining hole is then filled with the LPCVD deposition, and creates a sort of hook (circled zone in Fig. 4.17 a) which may in the worst case even connect the stator electrode. A reflow of the two PSGs allows a good smoothening and the elimination of the hook as illustrated in Figs. 4.17 b and 4.18.

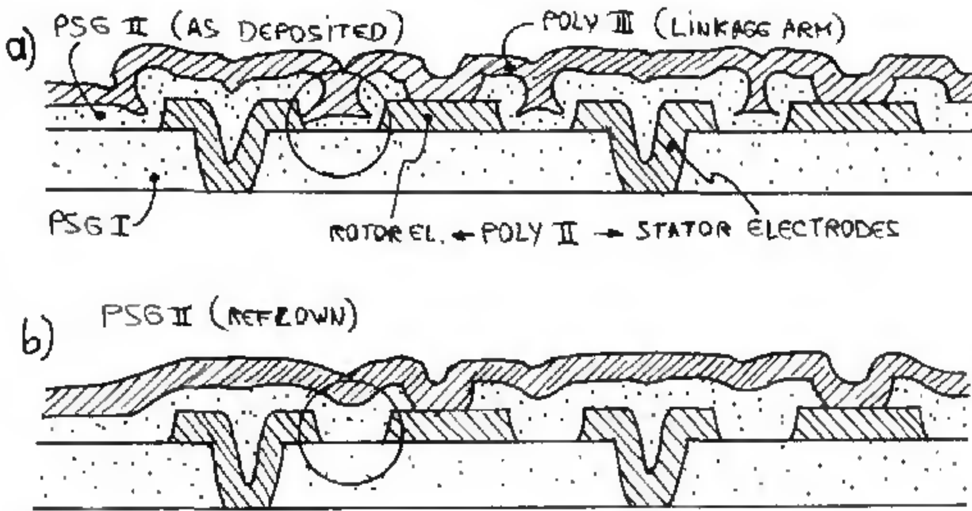

Fig. 4.17 Schematic process cross-section of the comb-drive motor. a) Without PSG II reflow, self-shadowing growth may produce inter-level polysilicon connections (circled). b) With a 1100°C PSG II reflow, the gaps are filled.

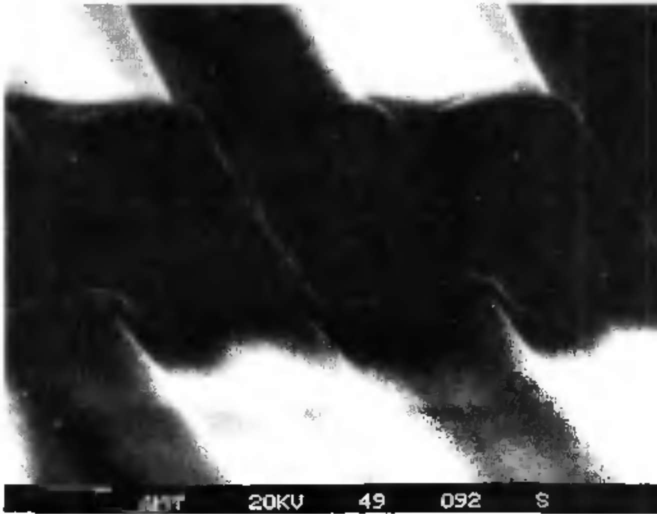

Fig. 4.18 SEM of the linkage arm of the comb-drive motor (poly III) deposited and defined over the reflown PSG.

4.1.4 Silicon whiskers

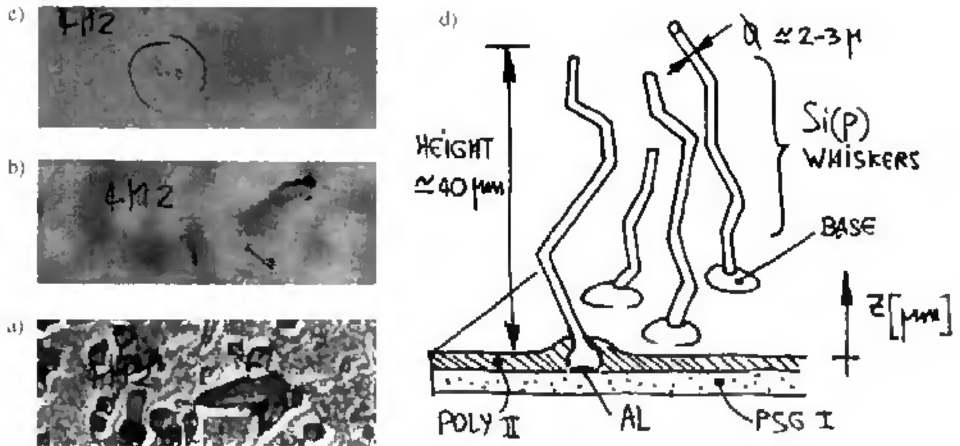

Fig. 4.19 Si (p) whiskers formed by nucleation growth from Al spots covering the PSG I, during the LPCVD deposition of the poly I. Microscope plan views at different focus heights: a) z = 0 μm, b) z = +20 μm, and c) z = + 45 μm. d) Sketch.

In the first runs, after the deposition of the Poly II, we have observed accidental formation of whiskers typically 40 μm long, consisting of a few successive straight cylindrical portions of 2-3 μm in diameter, randomly oriented as shown in Fig. 4.19. These structures appeared during the LPCVD growth of the Poly-Si II over the PSG I, and at regions where the aluminum of the precedent mask was not completely etched away, leaving small Al spikes. Consequently, it seems that the whiskers result from the rapid growth of an Al-Si compound, somehow extruded from the surrounding polysilicon layer in formation, inducing the observed bulby and slightly conical basal structure around an aluminum nucleation point located at the PSG surface.

We propose the following explanations for this "accident". A resembling phenomenon is described by Abbasi et al. [abb], studying the thermomigration of Al-Si liquid eutectic inclusions through n-type silicon wafers, leaving p-doped silicon behind. Typically, aluminum pads 3 μm thick and 50 μm wide traverse the 400 μm thick wafers within two hours, at a temperature of 1200°C and temperature gradient across the wafer thickness of 75°C. In our situation, the materials in presence are also aluminum and silicon, the temperature is somewhat lower (600°C) but the silicon source is gaseous instead of solid. In brief, let us assume to have nearly the conditions for the formation of the eutectic. Then, the only difference with Abbasi's experiments is that our eutectic Al-Si droplet is not moving, but remains at the PSG surface, "pinned" at the location of the aluminum unremoved spots.

Therefore the reaction product, i.e. p-doped silicon, simply grows and extrudes itself through the surrounding, growing LPCVD poly, hence in form of whiskers.

To conclude, we may say that the above hypothesis must be confirmed by further experiments, if this phenomenon finds a useful application (?). Otherwise, the imperative lesson is that the aluminum must be completely and very carefully wet-etched from surfaces before undergoing an LPCVD polysilicon deposition ! Even if an optical inspection does not reveal the presence of aluminum, an additional overetching is needed.

4.1.5 Bearing

Fig. 4.20 Bearing equipping all the motors. Top: SEM (bearing post top ø = 70 µm). Bottom: scaled process half cross-section (A-A).

The bearing equipping all motors (Fig. 4.20) is one of the most critical feature of the motors. The rotating part (hub) is restrained in all but the z-rotation degrees of freedom by the four bushings and the central post. Lateral play is determined by the bearing spacing layer, whereas the vertical play is determined both by the bearing and the bushings spacing layer. Ideally, one wants these spacings to be as small as possible, but has to consider the following design rules. If the bushing is designed too wide compared to the separation oxide, the

liberation underetch will be too slow. On the contrary, very small bushings (2 μm) are quite difficult to realize. In another way, if the separation oxide thickness is increased too far, once liberated the bearing hole will no more be at the appropriate height w.r.t the bearing post, compromising the lateral guidance. Therefore a compromise between bushing separation distance and size has to be made. We opted for bushings of 8 x 8 μm^2 and for a 0.2 μm spacing layer, which permitted complete underetching within one hour in BHF 7:1 (see sect. 4.1.6). Underetch via holes patterned in the poly-Si II allow a better access of the BHF to the underlying shallow regions of the bushings and the bearing hole. The sidewall of this last must be positive, unless it will not be covered properly by the bearing spacing oxide, due to the non-conformity of the CVD process.

The bearing hole must have a good roundness and the spacing layer has to be thick enough, unless the bearing risks lateral jamming when rotated (Fig. 4.21). In particular, jamming occurs when the radius (R_{bc}) variation is higher than the bearing clearance, or spacing layer thickness (l_{bc}). Therefore these parameters are of importance. For this process, on our masks, all circular objects are in reality polygons with a maximum of 48 edges. One can then easily calculate that a bearing hole radius of 35 μm with 48 edges leads to a radius variation of 0.075 μm. Tests have shown that the plasma etching irregularities along the poly sidewalls are well below this value. Therefore, the spacing layer thickness of 2000 Å is enough to prevent rotational jamming.

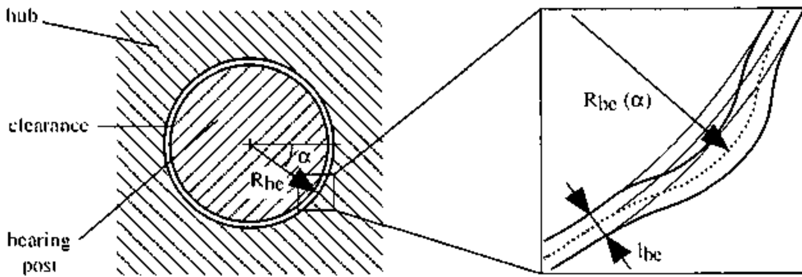

Fig. 4.21 Lateral rotation-induced bearing jamming. When rotated, the hub will jam to the post, when the variations of the radius (R_{bc}) are higher than the bearing clearance (l_{bc}).

However, in some cases, accidental defaults introduced by the photolithography of the bearing hole prevented the rotors from turning freely. Fig. 4.22 shows the enlarged view of a rotor bearing that has been forced to rotation by coercition with a prober needle. As result, the bearing came out of its track, revealing the failure cause, i.e. a large radial default of about 1 μm visible in the figure. On other samples, identical defaults of smaller dimensions did not prevent rotation under coercition, but the resulting radial contact forces caused by the jamming induced out-of-plane deformation of the bearing hub, hence of the entire rotor (Figs. 4.8-10).

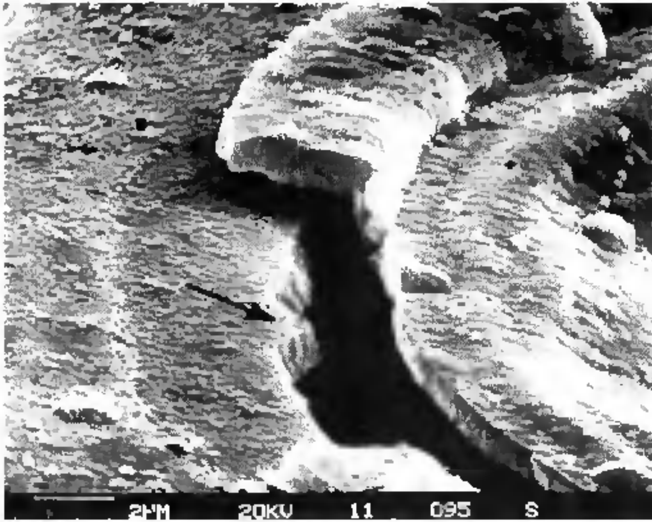

Fig. 4.22 SEM showing an enlarged view of a bearing hole edge. A photolithographic default of the poly II definition (arrow) provoked the failure of this bearing. The replication of the default in the poly III, in form of a boss, is visible in the upper right corner

4.1.6 Release etching

Appropriate x and y sizing of our structures must be made according to the final long BHF release etching. From measurements in the release step of his doubly-supported polysilicon beams, Linder [lin1] reports lateral underetch rates of 0.33 μm/mn in BHF 7:1 for a straight etch front in 1 μm thick phosphorous-doped CVD oxide. This leads to 20 μm/hr. In our case, the doping and the thicknesses of the sacrificial oxide is higher, therefore we may expect slower rates. The thin sacrificial regions of the bearing are x- and y-sized so as to maintain approximately the same sacrificial thickness-to-etch length ratio, i.e. about 1 to 40. Hence all polysilicons structured over 1.5 μm PSG have maximum widths in the order of 40 μm, and the bushings size of 8 μm is 40 times the spacing layer thickness of 0.2 μm.

Fig. 4.23 shows an undercut rotor edge after 45 min of etching. Square and rectangular dummy test structures with increasing sizes are used to monitor and measure the underetch rate, as shown in Fig. 4.24. From these two figures, lateral etch rates of 0.33-0.5 μm/mn are measured, which is quite close to the results of Linder [lin1]. More extensive measurements are thus needed to further assess the incidences of doping and thickness on the etch rate.

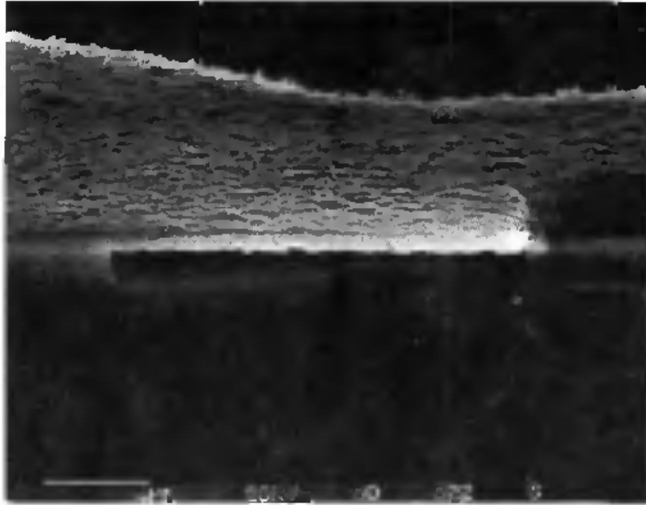

Fig. 4.23 Partially undercut rotor. The etch front in the PSG is visible at left.

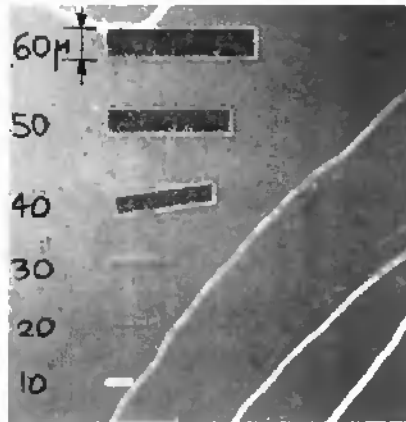

Fig. 4.24 Top view of polysilicon release test pads for the undercut evaluation, after 1 hour 20 mn of etching in 7:1 BHF.

4.2 Hybrid electroplated wobble motors [1]

4.2.1 General

Compared to the polysilicon motor process, this one allows the fabrication of ten times larger rotors (1 to 3 mm diameter) and their stators as listed in Table 2.2. It is named hybrid because of the combination of silicon technology, fine mechanics and assembly. Fig. 4.25 shows 32 motor chips (10 x 10 mm^2) on a 3" Si wafer.

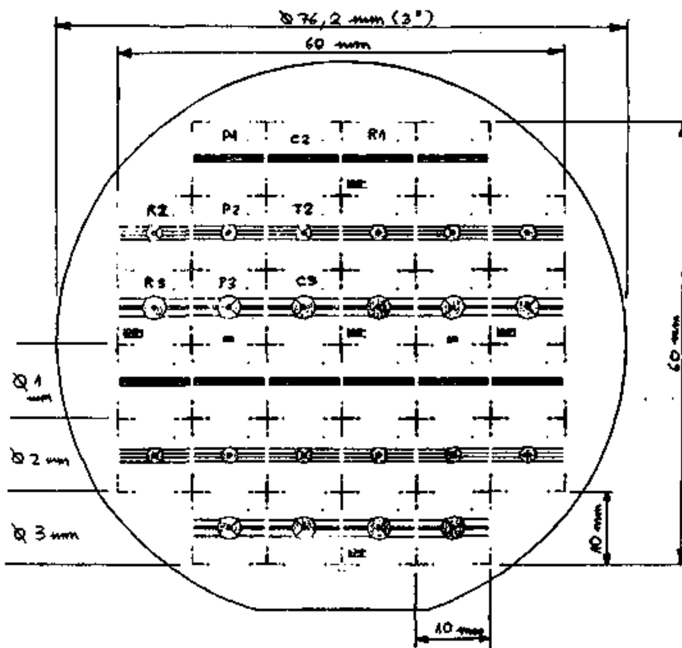

Fig. 4.25 Arrangement of the electroplated wobble motors on the 3" silicon wafer.

The stators are fabricated nearly in the same way as for the polysilicon micromotors whereas the rotors and the spacers are fabricated on another, separate wafer. The last are then released and individually assembled on the stator. In view of possibly performing in future wafer level assembly, each rotor is centered over its stator.

Motors with rigid rotors without the crank linkage (Fig. 2.21 c), so as motors with flexible gimbals rotors (Fig. 2.21 a, Fig. 4.5 left) coupled to a gear train have been realized. The former permits to better understand the free rotor behavior, whereas the latter

[1] Part of this work is published in [par5, par6]

demonstrates the capability for an electrostatic motor to drive a load. Both motors have quasi identical silicon-based rotors and stators, but different axle and guidance mounts. Hereafter, the complete devices will be described first. Then emphasis is given to the rotor and stator processes. Finally, the rotor electroplating photoresist mould is treated in detail.

4.2.2 *Rigid rotor motor*

Fig. 4.26 a shows a rigid rotor motor with a 3 mm diameter spoked rotor and a stator with polysilicon electrodes. The assembly is made manually. The chip is first glued to a PCB, to which the stators are wire bonded. For the aluminum stator, the wire bonding is directly made on the contact openings (Fig. 4.26 c). The axle (steel) is fixed to an overhanging bridge (aluminum), itself fixed to the PCB and to a base (brass). Axle and bridge are fabricated by conventional fine machining. The axle is 7 mm long and 0.5 mm in diameter, with one extremity machined to 90 µm in diameter and 250 µm in length. A microscope and vacuum probe tips mounted on a x-y-z micrometer-displaced stage help to place the rotor and spacer in the centered position. The axle is then lowered, its 90 µm diameter extremity fitted into the rotor hole (100 µm diameter) and pushed to clamp the spacer against the substrate (Fig. 4.26 b). The bridge fixing screw is then tightened. The spacer is overgrown with nickel on purpose, so as to form a half-closing hole of smaller diameter than the axle's extremity, and mounted upside-down so as to offer a gold-to-gold rolling contact to properly ground the rotor. The ground potential can then be easily applied either to the bridge (Fig. 4.26 a, top right) or to the conducting substrate with silver epoxy glue (EPO-TEK H20E).

4.2.3 *Flexible rotor motor coupled to a gear train*

A complete microreduction unit, consisting of an electrostatic wobble motor with the flexible gimbals rotor (Fig. 2.29), driving a pinion-and-gear train, has been fabricated (Fig. 4.27). Besides of output speed adaptation, these gears provide a test of the capability of such motor to drive a mechanical load. The inner ring of the rotor is fixed with conductive epoxy glue (EPO-TEK H20E) to the pinion axle, at the desired height. The rotor is grounded via the axle end, which pivots on the central metallization. The gear train unit has been fabricated by fine mechanics and assembled over the stator. The two axles (steel) are guided with synthetic ruby bearings. The bearing clearance is about 10 µm. The axle diameters are 160 and 100 µm. A frictional torque of 30 nNm (unlubricated) has been measured on one axle from spin-down tests of a brass disc having 8 mm diameter. The pinion and gear (brass) diameters are resp. 0.72 mm and 1.64 mm, leading to a gear train transmission factor of 2.3. The overall efficiency (gears and bearings) is around 94%. The teeth have a height of 115 µm, corresponding to a gear modulus of 51 µm (tooth height = 2.25 x modulus).

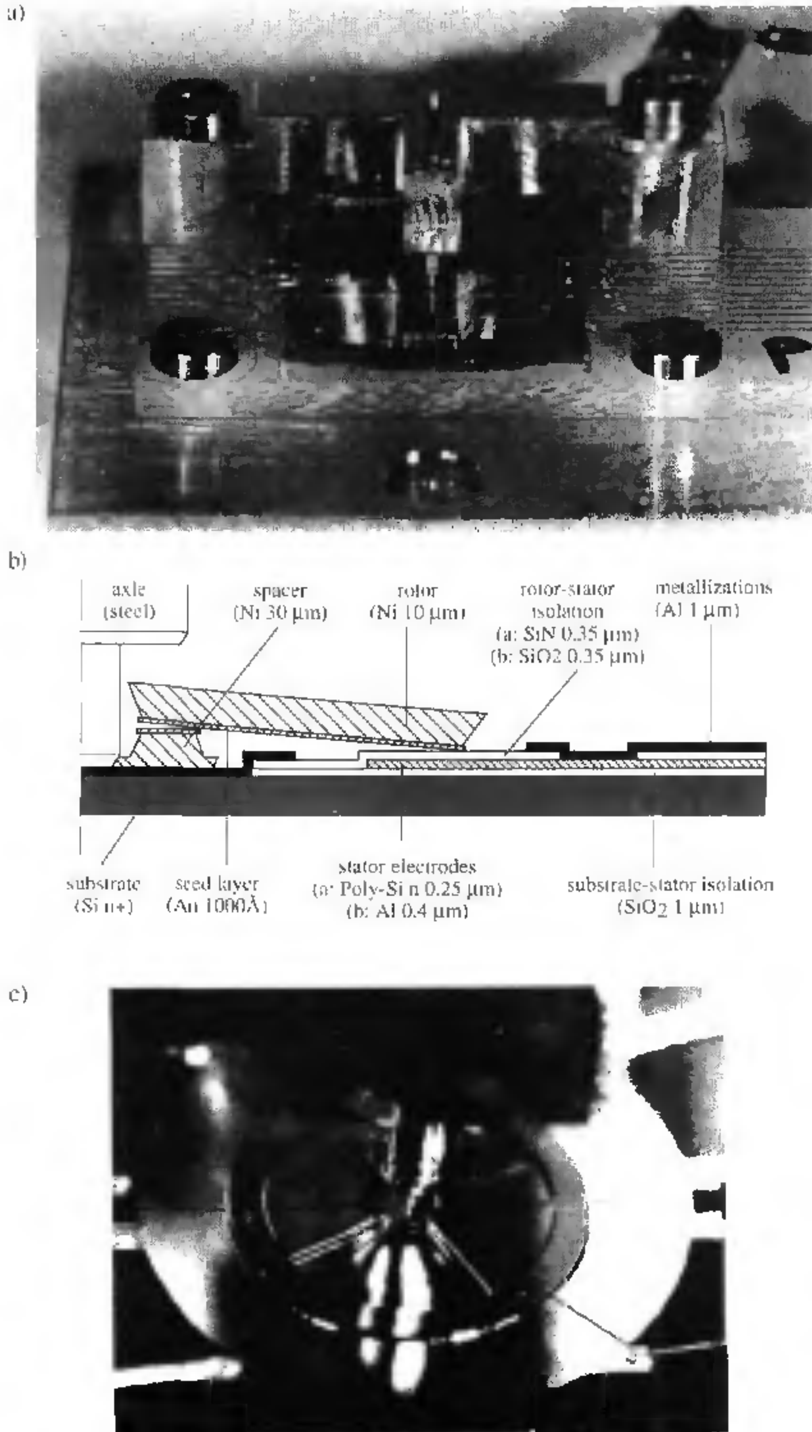

Fig. 4.26 Wobble motor with electroplated rigid rotor. a) Ensemble view (spoked rotor ø 3mm, poly stator), b) Half cross-section and c) Enlarged view (spoked rotor ø 2mm, alu stator).

a)

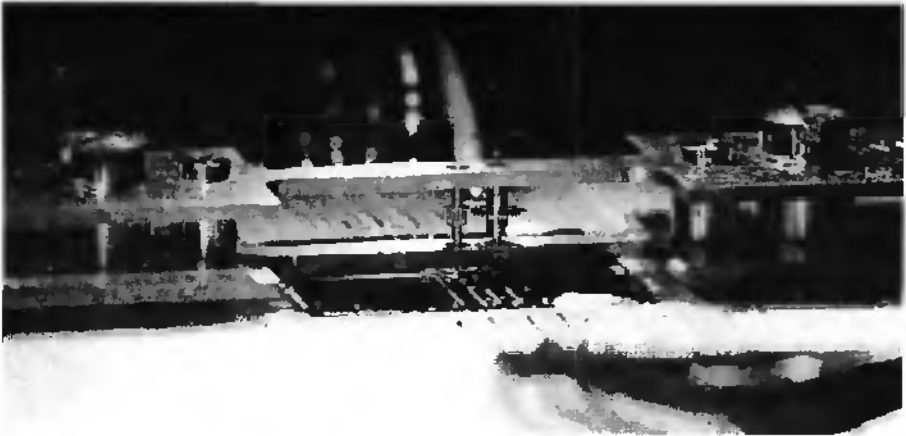

b)

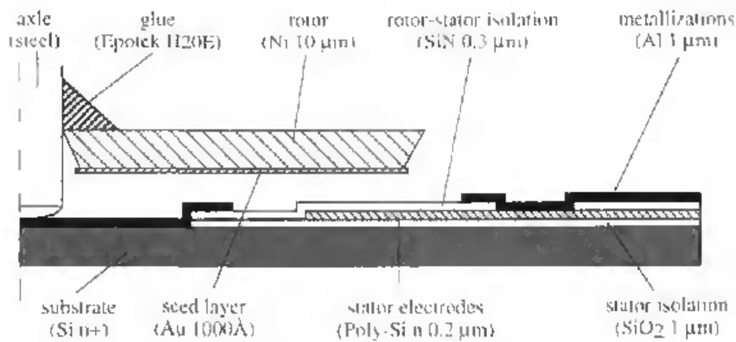

c)

Fig. 4.27 Wobble motor with electroplated flexible gimbals rotor coupled to a gear train. a) Ensemble view (chip 10 mm x 10 mm, pinion ø 0.72 mm, gear ø 1.64 mm, modulus 51.3 µm), b) Unmounted view showing the rotor (ø 2 mm), and c) Half cross-section.

4.2.4 Process

First, the Si wafers (ø 3", 380 µm, <100>, one-side polished, n-type, 4 Ωcm) are thermally oxidized to 1 µm thickness, for electrical isolation and etch stop during subsequent patterning (Figs. 4.26, 4.28 top). A Poly-Si layer of 2000 Å is deposited (LPCVD). A phosphorous-doped SiO_2 is deposited (CVD) and n-doping of the Poly-Si is performed with a 1100°C drive-in. After removal of the doping layer in BHF, the Poly-Si stators are defined with dry plasma etching down to the thermal oxide (mask 1). A thin SiN layer of 3500 Å is deposited (LPCVD) and openings are made for the contacts to the substrate and to the stators, first by a dry plasma etching of the SiN, followed by a wet BHF etching of the oxide (mask 2). Next, an aluminum layer of 1 µm is evaporated and defined to form the central metallization and the stator lanes (mask 3). Simpler stators having aluminum electrodes (3000 Å) instead of the Poly-Si, covered with a CVD SiO_2 layer of 3500 Å instead of the nitride have also been realized. The metallization step (mask 3) was skipped (Fig. 4.28 bottom).

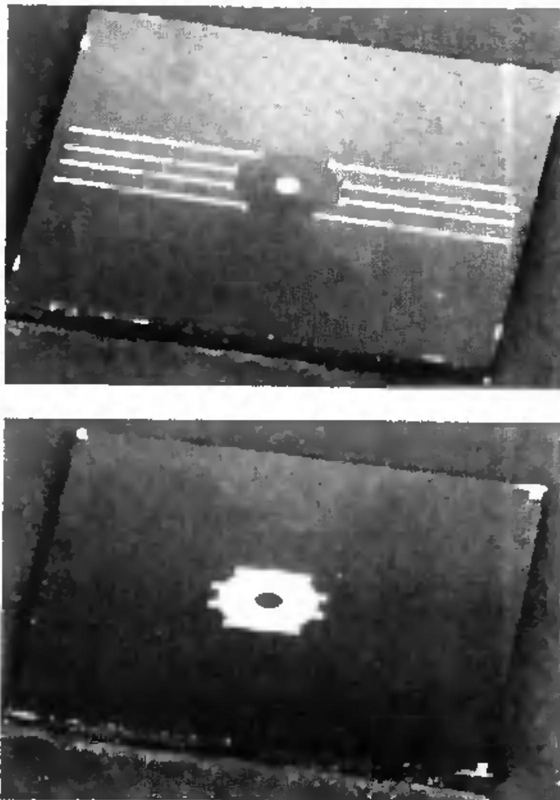

Fig. 4.28 Stator of the electrodeposited wobble motor (chip size 10 x 10 mm^2). Top: Poly stator, with 0.2 µm Poly-Si electrodes and 0.35 µm SiN isolation. Bottom: Alu stator, with 0.4 µm aluminum electrodes and 0.35 µm SiO_2 isolation.

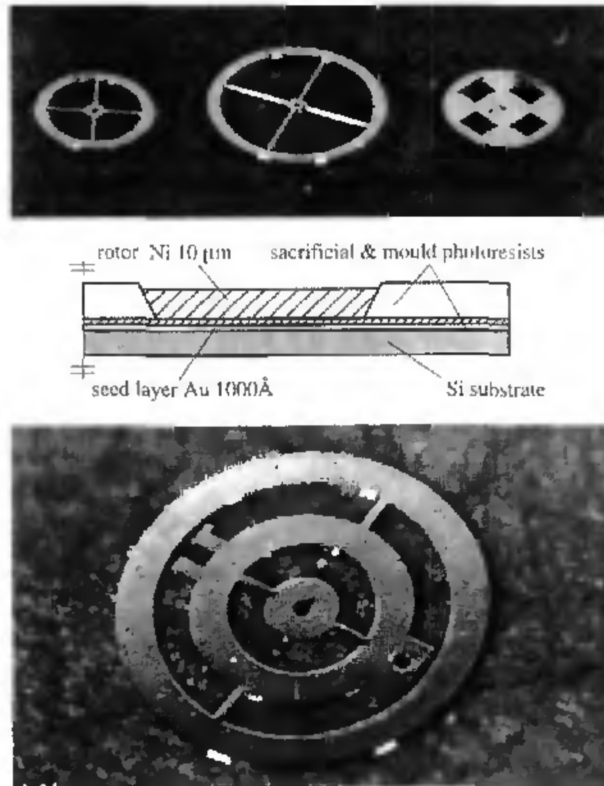

Fig. 4.29 Electroplated Nickel rotors (10 µm thick). Top: rigid rotors; spoked, ø 2 mm (left), ø 3 mm (middle), and half-opened, ø 2 mm (right). Middle: cross-section. Bottom: flexible gimbals rotor of 2 mm ø.

Afterwards, the rotor wafers are processed (Fig. 4.29). As for the stators, Si wafers are oxidized to 1 µm, to serve as electrical isolation during the subsequent electroplating. A sacrificial layer of 2 µm of positive photoresist is then spun (AZ 1400-27 from Hoechst ltd), over which a thin seed layer (or plating base) of 1000 Å of gold is evaporated. A thick positive photoresist (AZ 4562 from Hoechst ltd) up to 30 µm thick is deposited and patterned to form the rotor and spacer mould, as detailed in the next section. To enhance the plating base quality, an oxygen plasma is performed to clean the gold surface. These parts are then electroplated at the CSEM with up to 30 µm of pure nickel, with a 50°C nickel sulfate bath ("Nickal PC3" from Lea Ronal ltd). More details of the electroplating process are given in [gob]. For the structures release, the wafer is first dipped in acetone for 10' to remove the mould resist and to soften the sacrificial resist. The container is then submitted to 40 s of ultrasonic bath, which causes all structures to lift off from the support wafer. This operation reduces the 1000 Å thin gold layer into powder, whereas even the finest nickel structures remain intact. The wafer is then removed from the acetone. The bath is stirred and left free. During the liquid spin-down, the system tries to minimize its potential energy, causing the

heavier gold particles to cluster in the liquid rotation center, whereas the flat and lighter nickel structures remain stuck against the container's walls and bottom. The same phenomenon can be observed with small tea particles gathering in the center of a tea cup after stirring ! The gold clusters can then be easily removed by suction with a pipette. This operation is repeated until all the gold is removed from the acetone bath. Another possibility is to employ a magnet to separate the ferromagnetic nickel pieces from the non-ferromagnetic gold. In this case however, depending on the magnetic field strength, the nickel pieces risk to be permanently magnetized, since as-electroplated nickel is a hard magnetic material [guk3]. Afterwards, the bath is rinsed with fresh acetone and simultaneously the nickel parts are poured against a recuperation filter paper.

4.2.5 Electroplating mould

For the realization of the 10 to 30 µm-thick photoresist mould for the rotors and spacers, multiple coating of AZ 4562 positive photoresist from Hoechst ltd has been employed. Although vertical sidewalls are not crucial for the rotor functionality, some clues are given for their realization. Profound investigations of this interesting aspect are left for further research, as already exemplified by [beu, eng, goh]. Appropriate process parameters are listed to achieve an acceptable mould definition.

The wafers are first dehydrated at 85°C for 30 mn. Higher temperatures than 120°C cause bubbling of the already postbaked (120°C) underlying sacrificial photoresist. This unwanted phenomenon is due to the expansion of trapped nitrogen in the PR mass, formed during the polymerization. The resist thickness is specified at 6.2 µm for a 40 s, 4000 rpm single spin. A thicker film may be obtained at lower speeds or shorter spin times. However, we stated that 40 s spins at lower than 1800 rpm lead to unacceptable uniformity. On another side, shorter spin times may cause subsequent resist flow. We chose to spin at 3000 rpm for 40 s, leading to a measured resist thickness of 7.4 µm ± 0.4 µm S.D. A prebake of 35 mn at 85°C is then made. To obtain the wanted maximum thickness, the spin and prebake steps are simply repeated as many times as necessary.

An unwanted circular edge bead of resist result from surface tension effects and self-amplification induced by the multiple spin (Fig. 4.30 a). To promote the contact to the mask during exposure, hence high PR sidewall slopes [eng], the bead has to be removed. Daniau et al. perform this removal by cleaving the substrate [dan]. We tried two other methods. A Q-tip dipped in acetone can be applied against the wafer edge as a slow rotation is given to the spinner (Fig. 4.30 b). However, a secondary edge bead is formed due to the PR redissolution. In the second method, acetone is directly jetted against the high-speed turning wafer, e.g. with a syringe. The dissolution products are immediately ejected from the wafer edge, and no secondary bead is left (Fig. 4.30 c).

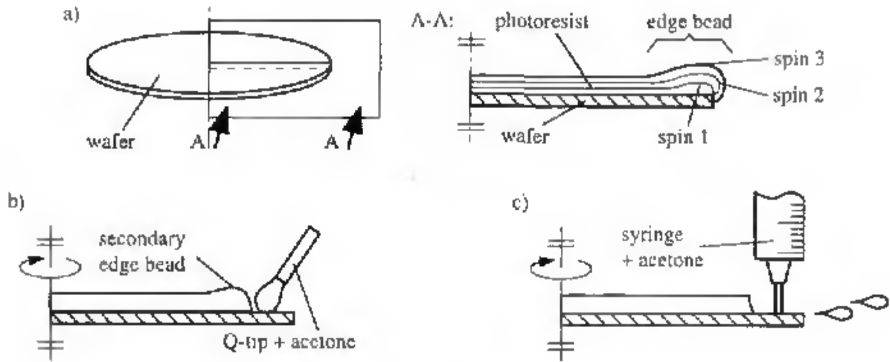

Fig. 4.30 Edge bead formed during multispin resist coating. a) Explanatory view, b) Bead removal with Q-tip dipped in acetone, with slow spinning, and c) Bead removal with acetone jetted by a syringe under high-speed spinning.

Exposure is performed with our standard UV mask aligner (Karl Suess), using a high pressure mercury lamp (1000 W). The i (365 nm), the h (405 nm) and the g (436 nm) lines in its spectrum contribute principally to the resist sensibilization. During illumination, the wafer is pressed against the mask by the weight of the wafer stage (contact mode). A strong bleaching of the resist is visible after exposure: during photopolymerisation, gaseous nitrogen forms and renders the exposed resist mass progressively opaque. The resist is then developed using AZ 351 Hoechst developer, diluted in four parts of DI water.

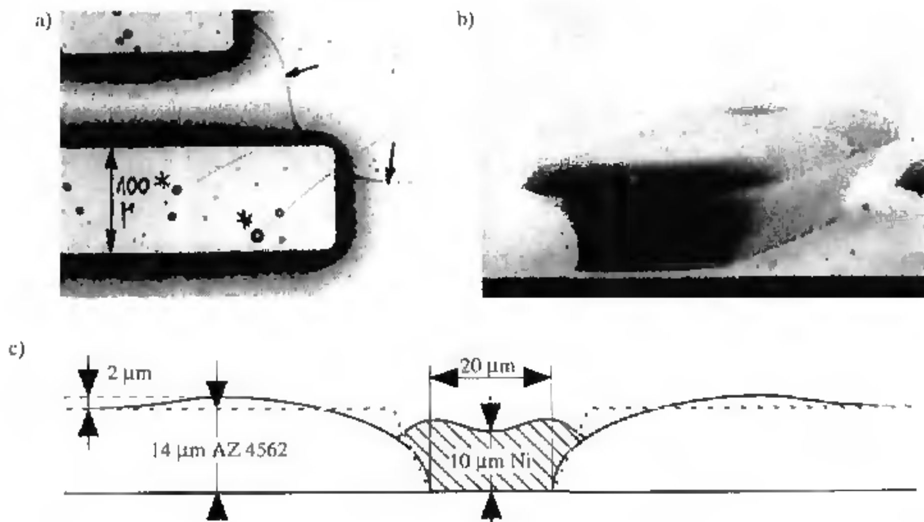

Fig. 4.31 Preliminary tests with two spins of AZ 4562 positive photoresist, postbaked at 120°C during 30 mn, and electroplated Nickel. a) Top view showing cracks in the resist (arrows) and bubbles on the nickel surface (*). b) Rectangular Ni pad released from the resist mould, and c) Cross-section (to scale); the dashed line is the resist shape before postbake.

A soft postbake is performed (typ. 60 mn at 60°C), because postbakes at temperatures near to these of the prebake or higher may cause significant mould defects. Fig. 4.31 shows the result of preliminary tests, where 10 µm of nickel where electroplated in a 14 µm thick resist mould. The resist was postbaked at 120°C prior to electroplating, causing the sidewalls to flatten and become convex, as if reflown (Figs. 4.31 a and c). Cracks also appear in the resist (Fig. 4.31 a). Engelmann et al. also underscore the importance of the postbake step, and mention as well that the postbake temperature should be below that of the prebake to prevent "flow and shrinkage of the structures" [eng].

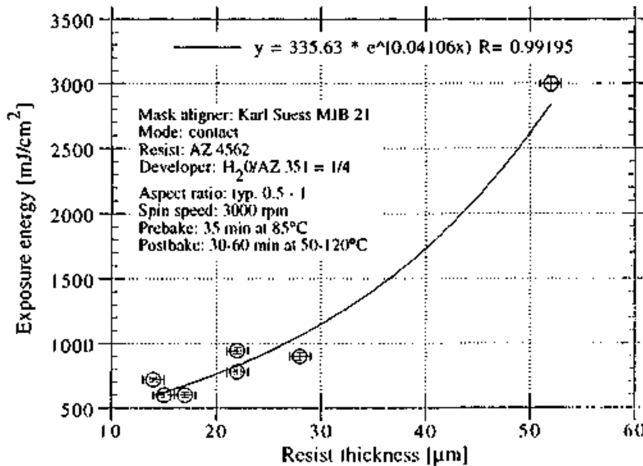

Fig. 4.32 Exposure energy as function of the resist thickness, for reflecting and non-reflecting substrates, with exponential fitting (line).

Resist thicknesses between 7 and 50 µm, coated over reflecting (gold, silver) or non-reflecting (SiO_2) layers have been patterned to assess the exposure and development parameters. The too important edge beads of the 50 µm samples are removed with the Q-tip and acetone method. A successful patterning consists in opening lines with typical aspect ratio (depth-to-width ratio) of 0.5 to 1. The corresponding exposure energies are given as a function of the resist thickness in Fig. 4.32. Due to optical absorption, one can expect that the needed energy varies exponentially with the resist thickness, considering a fixed, threshold energy needed at the structure bottom. Therefore the graph data is fitted with an exponential law. However, a lot of points are lacking in the range between 30 and 50 µm. From this data it is not possible to differentiate between reflecting and non-reflecting substrates. For the 50 µm samples, highly illuminated regions are not as well developed as dark regions: a thin crust of resist a few microns thick remains at the bottom, which cannot be removed by additional development. A possible explanation is that the long exposure time heats the resist portions up, initiating polymerization and/or reducing the photosensitivity. This phenomenon is stronger in higher illuminated regions, where the temperature is higher. Beside this exception,

all thicknesses have been acceptably developed within a total dip time of 3 mn in the 1:4 AZ 351:water solution.

SEMs of the rotors permit deductions about the mould (Fig. 4.33). Sidewall slopes of about 2 are visible, which is acceptable for our application. The soft postbake still causes some reflow, as indicated by the mould sidewalls convexity. A small sidewall dwelling of ± 1 µm is visible (enlarged area 1). The sidewalls have very smooth surfaces. Here, the nickel grew over the resist (both enlargements). This "mushrooming" effect is wanted for the spacers (sect. 4.2.2). As for the Poly-Si motors, circles are polygons with 48 edges (enlarged area 2).

Fig. 4.33 SEMs of an electroplated spoked rotor, viewed from the seed layer (Au) side (ø 2 mm, thickness 15 µm).

Chapter 5 - Testing

5.1 Drive electronics

5.1.1 Description

A 12-channel, ± 140 V bipolar drive electronics has been specially built for the open-loop actuation of the motors (Fig. 5.1). The excitation sequence is generated by a 5V switching logic unit (SWU), commanding a series of high-voltage operational amplifiers. The output square wave signal is swept sequentially across the motor electrodes or groups of electrodes (phases), to create a turning field at the stator. The rotor and all inactive stator electrodes are grounded.

All commutation possibilities represented in Fig. 5.2 can be satisfied using the 1-to-12 demultiplexer-based SWU, allowing the excitation pattern '..0100..', '..0010..', and so on, where a '0' indicates a grounded stator electrode, and a '1' an excited one. Resets at counts of 3, 6, 8 and 12, so as direction reversal are possible. Two polarity modes can be selected, either unipolar for counts up to 12, or bipolar for up to 6 counts. The pulse duration can be optionally adjusted to lower than the switching period T (pulse width enable mode), or left normal (pulse width disable mode).

To drive the wobble motors more smoothly and continuously, and avoid slipping during the switching, the contact force must be high. This is possible by introducing some time overlap in the switching between two adjacent electrodes. This can be done by lowering the drivers slew rate ("overlapped" mode), so that two successive pulses overlap by their rise and fall slopes. Another way consists in using a 12-bit shift register SWU in place of the demultiplexer SWU, enabling the generation of excitation patterns like '..001100..', '..000110..', and so on, or '..011100..', '..001110..', i.e. where more than one electrode is excited at a time with a shift of only one electrode.

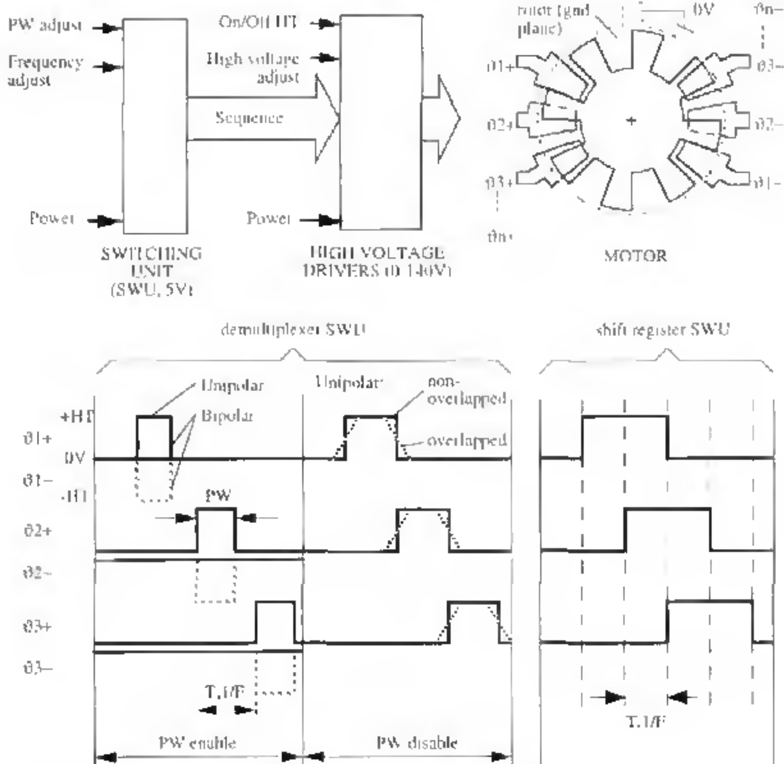

Fig. 5.1 Dedicated open-loop control electronics of the electrostatic micromotors. Top: 12" rack implementation with connected motor, bottom: operating principle.

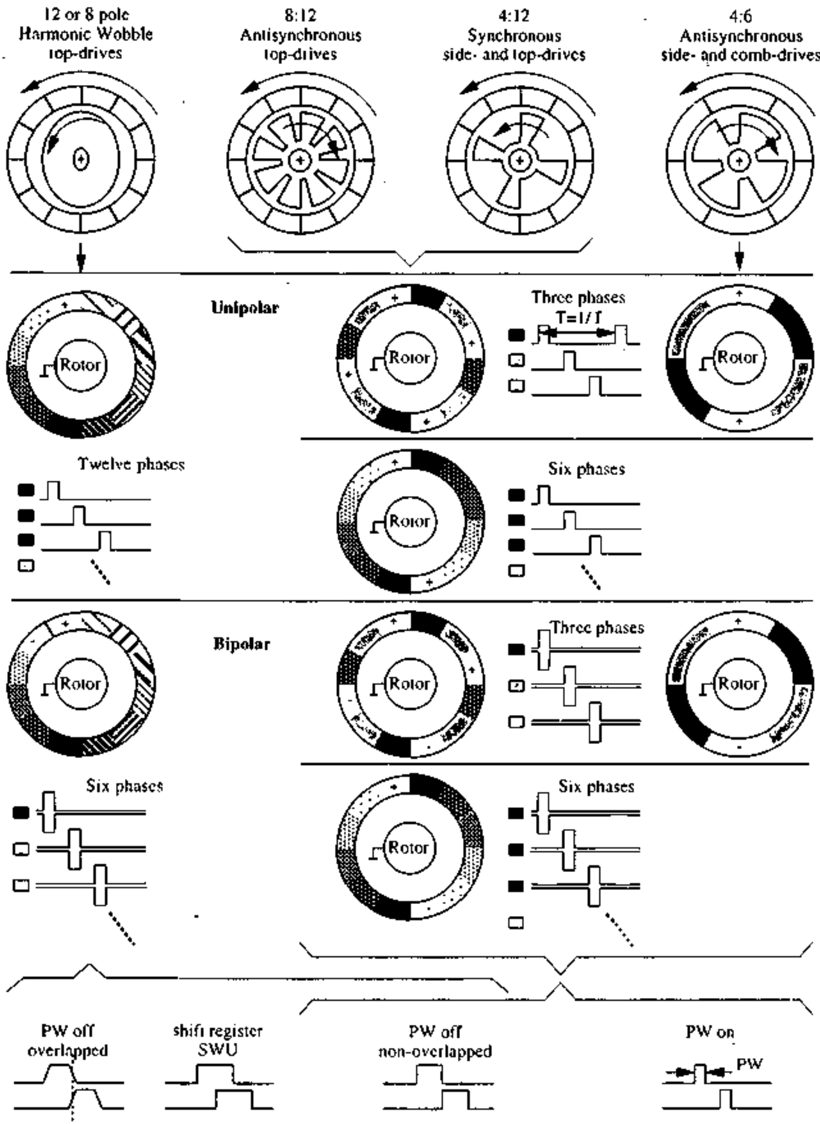

Fig. 5.2 Commutation modes for all constructed electrostatic micromotors.

5.1.2 *Determining parameters for the output drivers*

The output drive circuitry of the electronics has been sized according to a set of motor physical parameters, such as the gap voltage, the motor mechanical step response time and the parasitic and motor capacitances. Concerning the first of the three parameters, we have seen from sect. 2.1 that a micrometer-sized air gap is able to sustain voltages up to typ. 300 V

before breakdown. Nevertheless, considering the field non-uniformities (likely to appear along the rotor tooth edges) and the capabilities of most available high-voltage drivers, a reasonable voltage of ±100 V applied across our 1 μm air gaps is taken. The torque vs gap graph of Fig. 2.4 gives a theoretically achievable electrostatic torque of 30 nNm at voltages higher than 300 V (see Paschen curve, Fig. 2.3). In the worst case, we assume to have this torque at 300 V. This means that the torque at 100 V is 9 times lower than at 300 V and amounts to 3.3 nNm. This value is still higher than the electromagnetic achievable torque by a factor of approximately 5.

Secondly, the rise time of the signal (0 to 100 V) delivered by the output drivers should be much shorter than the motor mechanical step response time, to achieve acceptable square wave commutation. Among all, the 200 μm diameter 8:12 top-drive of Fig. 4.3 is logically expected to have the shorter response time, because of its higher static torque / inertia ratio.

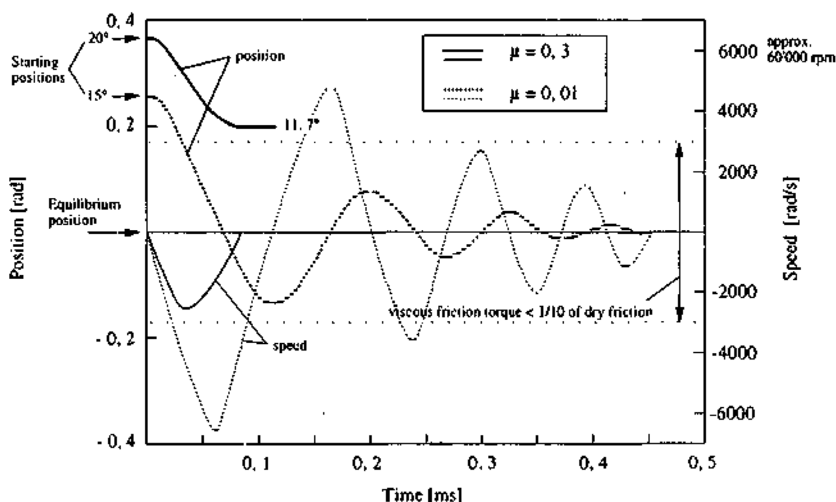

Fig. 5.3 Simulated mechanical step response of the 200 μm ø 8:12, top-drive electrostatic motor (Table 2.1, Fig. 4.3, [lin2]), with two opposite stator electrodes excited with 50 V and grounded rotor.

Fig. 5.3 shows the calculated dynamic response of the rotor to a step voltage of 50 V applied to two opposite stator electrodes, for two starting rotor positions and at two dry friction coefficients [lin2]. The rotor motion law (2nd Newton's law) around z is analytically solved taking only the air drag and the electrostatic excitation (motive and friction) torques into account [bar2]. These electrostatic position-dependent torques have been calculated in sect. 2.2.4. For the simulation of Fig. 5.3, the fringing fields are taken into account as explained in [par1]. Because the separation distance between the rotor disc and the stator plane is only 1 μm, the air drag torque is mainly due to the tangential viscous forces resulting

from the laminar air flow between these two surfaces. In particular, even the drag torque due to the penetration of the rotor blades in the air is negligible. Hence the air drag term is calculated by integration of these viscous forces over the rotor (bottom) surface and is proportional to the speed [par1, gab2, bar2].

From this simulation, we can see that the shorter mechanical response time, i.e. for $\mu = 0.01$, is roughly 50 µs, or one fourth of the oscillation period. For 100 V, the torque is 4 times higher since it scales as the voltage squared. The rotor can be considered as a rotating spring-inertia system, the spring being the electrostatic torque. Its oscillation period, hence its response time are roughly proportional to the square root of the inertia divided by the spring constant (the torque). Consequently, the response time at 100 V is about 2 times lower than at 50 V, hence of 25 µs. A rise time 1/10 th of this response time, i.e. 2.5 µs, is accepted for the drivers.

From the two last parameters, we can deduce a slew rate of ±40 V/µs (rise and fall slopes). The estimation of the current necessary to load and unload the stator electrodes at this rate implies the knowledge of the motor equivalent circuit. The 200 µm ø top-drive motor is again taken as a representative case. For one pair of opposite stator electrodes with the rotor in aligned position, the air gap capacitor C_a amounts to 3.3 fF [par1] and is paralleled by some 40 pF of parasitic capacitor formed by the metal lanes covering the grounded substrate and GND plane. In the case of the ten times bigger, millimeter-sized wobble motors, the working VC is multiplied by approx. 100, leading to C_a around 400 fF. Hence, the motor VCs are negligible compared to the parasitic substrate capacitances, 2 to 4 orders of magnitude bigger. A maximum rise/fall transient current of ±1.6 mA is needed to charge/discharge the 40 pF at the slew rate of ±40 V/µs.

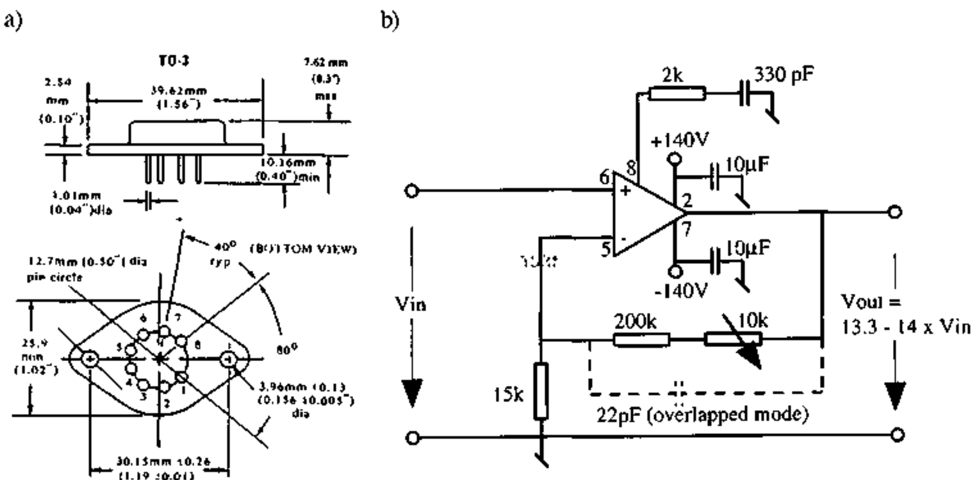

Fig. 5.4 High-voltage operational amplifier (model 3584 JM from Burr Brown) used in the output stage of the control electronics. a) General view, b) As mounted for our application.

The model 3584 JM operational amplifier from Burr-Brown has been selected for our application (Fig. 5.4). Some of its characteristics when mounted like in Fig. 5.4 b are listed in Table 5.1, together with the desired parameters.

Table 5.1 Output stage switching maximum ratings.

	output voltage (V)	slew rate, SR (V/µs)	current @ SR (mA)
desired (two poles)	± 100	± 40	± 1.6
Op Amp BB 3584 JM	± 140	± 150	± 15 - 25

The output current capabilities of the amplifier are much higher than needed, so that more than two electrodes can be driven at a time. This amplifier shuts itself automatically off when a case temperature of 150 °C is reached, in case of abnormal output current delivery like rotor-stator short-circuit. The choice of an operational amplifier rather than a high-voltage switch was also directed by the possibility to generate signals different than square waves.

5.1.3 Comments on efficiency

Let us illustrate the system efficiency by a few calculations. Under 100 V, the 8:12, 200 µm ø top-drive motor achieves a theoretical maximum speed of 2 x 10^5 rpm, with 12 steps/revolution and a step response time of 25 µs. Using eq. (2.17) with R = 100 µm, Ri = 60 µm, d = 1.5 µm and V = 100 V, an average step torque of roughly 50 pNm is obtained. Multiplying the speed by the torque leads to a maximum mechanical power of 1 µW, from which a (big) part is dissipated by friction. The charge and discharge cycles of the larger motor air gap VCs (400 fF) at ± 40 V/µs through typ. 10 Ω (wiring) cause only 50 pW of average dissipated power, against 5 µW when calculating with the 40 pF of parasitic. Consequently, the theoretical motor efficiency is hampered by the parasitic substrate capacitances. Moreover, the power dissipation of one BB3584 amplifier being typically 3 W, the overall electromechanical system described below, motor and control electronics, is far from being efficient.

High-voltage FETs may be used in place of the sophisticated op amps used in our test electronics, to enhance the system efficiency. The motor efficiency could be increased by lowering the parasitic capacitances (isolating substrate), by using a resonant circuit [tav2], or by implementation of a charge-coupled device architecture at the stator, so that charges can be transferred from one electrode to the adjacent one. Such systems enhancements are not treated further in this context, and remain suggestions for future work.

5.2 Test set-up

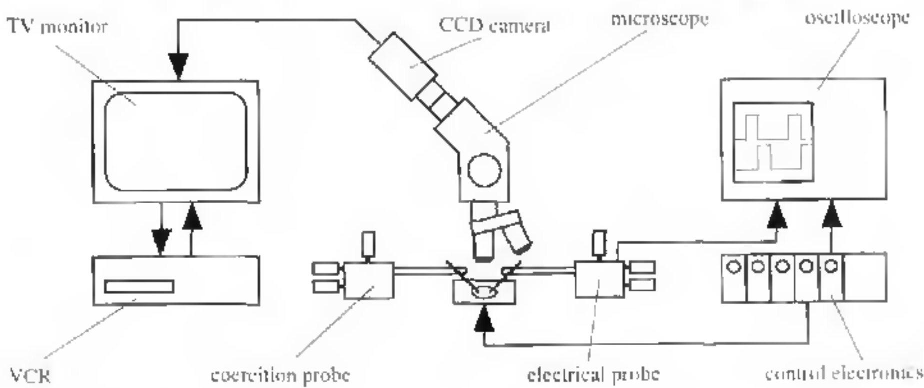

Fig. 5.5 Basic bench for the test of the electrostatic micromotors.

Both the polysilicon and the electroplated electrostatic motors have been electrically tested (Fig. 5.5) in normal ambient (20°C. 40-50 RH. grey room). An oblique vision with a binocular microscope is required for the electroplated motors, because of their top-hidden rotors. The integrated polysilicon motors can be observed in top-view with another microscope. The microscope image of the motor is displayed on a monitor using a CCD camera. A video cassette recorder (VCR) permits to record image sequences, for further processing. An oscilloscope is used to display the excitation sequences supplied by the control electronics, i.e. from the electronics itself or directly at the motor electrodes via an electrical microprobe. A floating-potential coercition probe mainly permits to check rotational freedom before electrical testing, besides of various other micromanipulation tasks.

5.3. Integrated polysilicon motors

5.3.1 Samples preparation

For the electrical testing, the motors on PCB (Fig. 4.11) are directly mounted on a test fixture (Fig. 5.6). Spring contact needles allow to simultaneously connect all PCB poles and clamp the PCB to the base plate. The GND plane and substrate are connected to ground. Only the demultiplexer SWU has been used for these tests (see electronics description). A cabled adaptation jumper, specific for a given motor and commutation scheme, is put between the cable coming from the electronics and the test fixture. The fixture is then brought under the microscope. Prior to electrical testing, a small coercition is exerted on the rotor with the microprobe to attest and ensure rotational freedom.

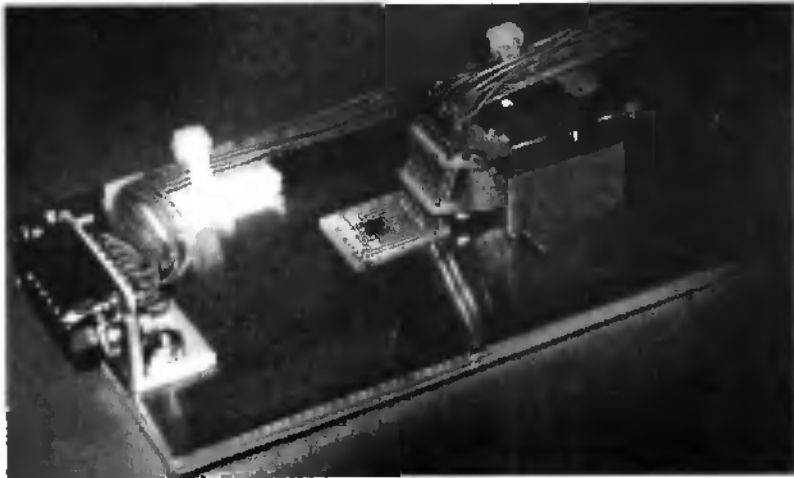

Fig. 5.6 Test fixture for the VC polysilicon motors.

5.3.2 Breakdown voltages of the devices

Electric breakdown of the substrate isolation rather than in the air gaps has been observed when typically 110 V biases were applied to the stator electrodes (Fig. 5.7). The stator lane-to-substrate isolation is composed of 3000 Å of thermal silicon dioxide and 2000 Å of silicon nitride. The field in each of these two dielectric capacitors (put in series) can be easily calculated as being equal to

$$E_1 = \frac{1}{(\varepsilon_1 d_2 / \varepsilon_2 d_1) + 1} \frac{V}{d_1} \quad (5.1)$$

where the indices 1 and 2 are related to each of the two layers. V denotes the applied voltage, ε the relative dielectric constant(s) and d the layer thickness(es). Introducing the above-mentioned thicknesses and relative dielectric constants of 3.9 and 6 [sze1] for resp. the oxide and the nitride into this equation, we obtain for a breakdown voltage of 110V fields strengths of 256 and 166 MV/m respectively in the oxide and in the nitride. These values are quite below the field strengths of typ. 1000 MV/m mentioned for these materials in the IC literature [sze]. Nevertheless, a lot of fabrication-induced local defaults could cause one of the layers to breakdown. Therefore these breakdown values should be considered carefully.

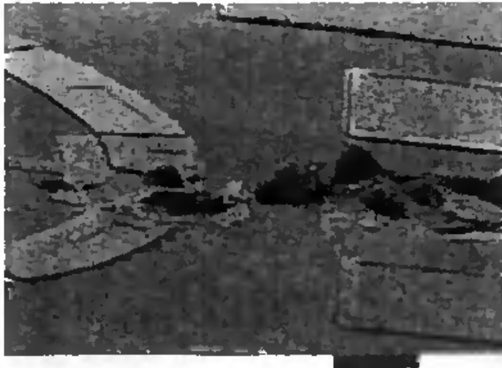

Fig. 5.7 Destruction of the stator electrode of a 4:12, 500 µm ø side-drive motor through stator-to-substrate isolation breakdown at 110 V DC.

It has been observed that voltages as high as 110 V never created breakdown in the 1.5 µm long air gaps of the top-drive motors. This does at least not infirm the Paschen's law (Fig. 2.3) and the torque will be close to the expected 3.3 nNm calculated in sect. 5.1.2.

5.3.3 Electrical actuation of side-, top- and comb-drive motors

A majority of the direct-drive motors (side-, top- and comb-drives) did not rotate even under electrical excitations of up to ±100 V, in all possible modes of excitation (mono- or bipolar, 3, 4, 6 phases). Rotor out-of-plane deformations of 1-5 µm like in Fig. 4.8 were observed (SEM) in most cases and were due to rotation-induced jamming of the bearing (see sect. 4.1.5). Such radially-oriented defaults from the ideal hole circle can be as low as 0.2 µm in amplitude to induce bearing failure, since the spacing layer is of that thickness.

Local defaults in the resist patterning were already identified to cause bearing failure (Fig. 4.22). But this is insufficient to explain the failure of most bearings. Fig. 5.8 shows an enlarged SEM of one dismounted bearing. The hole sidewall is quite rugged and reveals polysilicon grains of 100 to 500 nm in size. Their boundaries (in white; some are evidenced by broken lines) have probably been rendered visible by the action of the long release BHF

etching, causing even some small grains to be removed from their locations (arrow). The consequence to be drawn is that the surface roughness (peak-valley height difference, R_{max}) of this sidewall is expected to be roughly equal to the average grain size, i.e. of 300 nm.

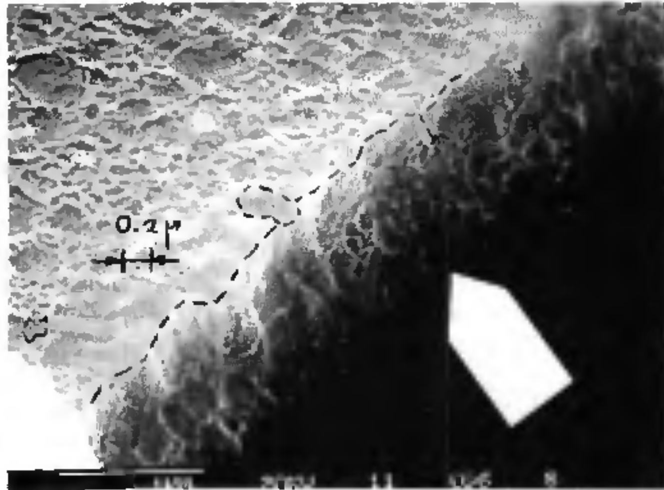

Fig. 5.8 SEM showing an enlargement of the rotor bearing hole sidewall. The edge and some polysilicon grains are evidenced by broken lines. Some grains have been detached from their locations (arrow).

The observed grain sizes correspond well with other studies. Polysilicon depositions at typically 250 mtorr and temperatures below 580°C lead to amorphous polysilicon, whereas higher deposition temperatures as in our case (600°C) lead to polycrystalline structuration and increasing grain sizes with temperature [gue2, lee, vat]. Vatel et al. evaluated average grain sizes of 180 and 250 nm for resp. 580 and 620°C deposited polysilicon layers using AFM, STM and TEM. Moreover, subsequent anneal cycles of large-grained polysilicon cause further grain growth [gue2]. It is likely that our large grains of 300 nm average size are responsible for blocking sidewall irregularities, since the spacing distance is lower (200 nm).

Attempts of mechanical run-in of the reluctant motors have been made. The rotors were rotated with the probe over 5 to 10 revolutions, then rinsed in solvents (acetone, isopropanol) to remove eventual shed bearing matter, and again coercition-rotated. No distinct improvement of the electric rotatability was noticed after this treatment. This is correlated by the fact that no wear particles were detected just after the coercition turns in the bearing vicinity.

Despite of this, a few electrical rotation sequences have been observed for some of the motors, and over a given angle range were the bearing was functional. It was sometimes even possible to pull the rotor tooth by adhesion against the probe tip over this range, attesting real

rotational freedom. Such adhesion forces, in the order of one micronewton[1], are explainable by liquid surface tension appearing between the adsorbed water at the probe and rotor tooth contacting surfaces [kan]. In general, a pulse width (PW mode) shorter than the commutation time led to better results in electrical rotation for these samples.

A 4:12, 500 µm ø top-drive motor, excited in bipolar, 12 phase, with PW = 20 µs at ± 80 to ±100V has been CCW-rotated electrically over a 7° range (Fig. 5.9). The starting (-21° w.r.t the rotor-stator centered position) and stopping (-14°) positions are both visible on the figure, attesting a shorter motor response time than the video camera shutter time (8 ms or 1/125 s). This actuation step was reproduced about ten times, the microprobe helping to place the rotor back in the start position each time. Intermediary rinsing in solvents, drying and re-coercition helped to maintain the bearing operational state within this 7° range. In starting position, the rotor blade is still some 1-2° away from the excited stator. This indicates that the fringing fields are of importance. It is not clear whether the rotor has been stopped by the bushings friction (as modeled), or by a sudden clamping by the rotor blades pulled downwards against the stator.

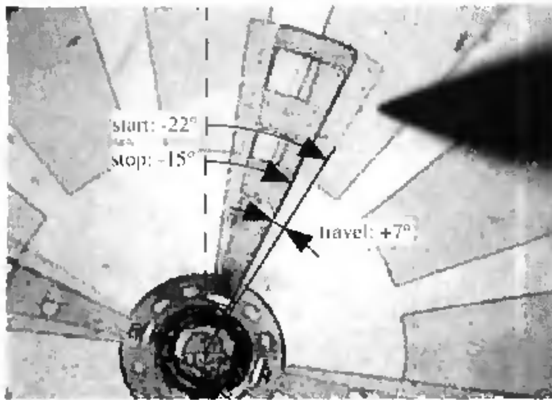

Fig. 5.9 Electrical CCW step of a 4:12, 500 µm ø top-drive motor excited in bipolar (± 80 - 100 V), six phase mode, and PW = 20 µs.

A 4:6, 540 µm ø comb-drive motor, excited in bipolar, 3 phase, with PW = 25 µs at ± 40V has been CCW-rotated once over a 19° range (Fig. 5.10). Here, the rotor started its electrical step while it was still pushed in CCW direction with the microprobe. Again, starting (-32°) and stopping (-13°) positions are visible here. This step could not be reproduced, even with run-in of the device as described above.

[1] The 500 µm ø rotor of the 4:12 top-drive motor (fig 5.9) has a weight of about 1.4 nN, i.e. 1 / 714 of a µN !

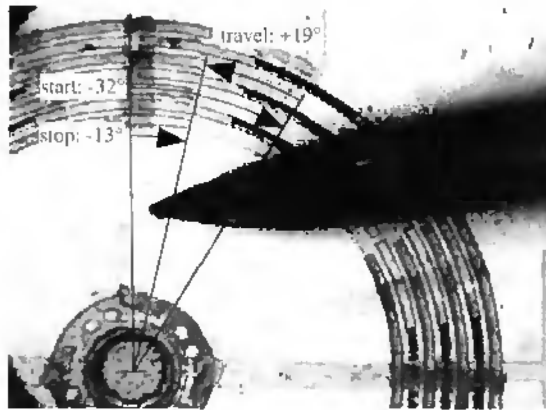

Fig. 5.10 Electrical CCW step of a 4:6, 540 µm ø comb-drive motor excited in bipolar (±40V), three phase mode, PW = 25 µs.

A 4:12, 500 µm ø side-drive motor, like the one of Fig. 4.2, excited in bipolar, 3 phase, with PW = 200 µs at ± 80V has been CW rotated over one and a half step (45°), under nitrogen levitation assist. The nitrogen flow was directed towards the motor center by means of a glass pipette (inner diameter 800 µm). Still, it is not exactly clear whether the air flow or the electrical excitation were mainly responsible for this unrepeated rotation. Sometimes, partially blocked side-drive motors showed radial wobble motions under electrical excitation, which led to wobble-induced rotation over a few degrees.

Attempts of motor run-in with the nitrogen flow directed on the rotor blades were also unsuccessful. In place of spinning the rotor, the flow caused the rotor blades to deform upwards and finally break, even for samples possessing a free bearing over a small angle portion.

5.3.4 Discussion on the bearing function

Bearing sidewall irregularities of more than 0.2 µm -the spacing layer thickness- evidently cause the bearing failure. A strong correlation seems to exist between the polysilicon bearing sidewall roughness and its grain size, but the phenomenon that revealed the grainy surface remains unexplained.

The coercition run-in over 5 to 10 revolutions is not effective to grind away the blocking irregularities. For this, higher speeds and higher number of turns are required to initiate a proper grinding wear state. But the most promising method to do this, the nitrogen (or air) blow is insufficient because of too high jamming of the bearing.

The solvents rinsing step seems to have some impact on the bearing functionality, as shown by successful electric re-actuation over a range of free rotation after such treatment. Either a blocking particle has been washed away, or the solvents have a lubricating effect. This last is the more plausible since no traces of wear particles have been found.

The bearing could be rendered operational by simply increasing the spacer thickness and by avoiding resist defaults. Its sidewall smoothness, hence its performance could be enhanced further by using fine-grained LPCVD polysilicon (deposited around 580°C) instead of large-grained. Nevertheless, the process mechanism revealing the grainy sidewall structure should be explained and avoided in further improvements. It is likely that the 1100°C drive-in provokes an unwanted increase of the grain size, so as to block the rotors. One possible way to solve this problem may be to perform the drive-in step before structuring the poly II.

5.3.5 Levitation effects in side-drive motors

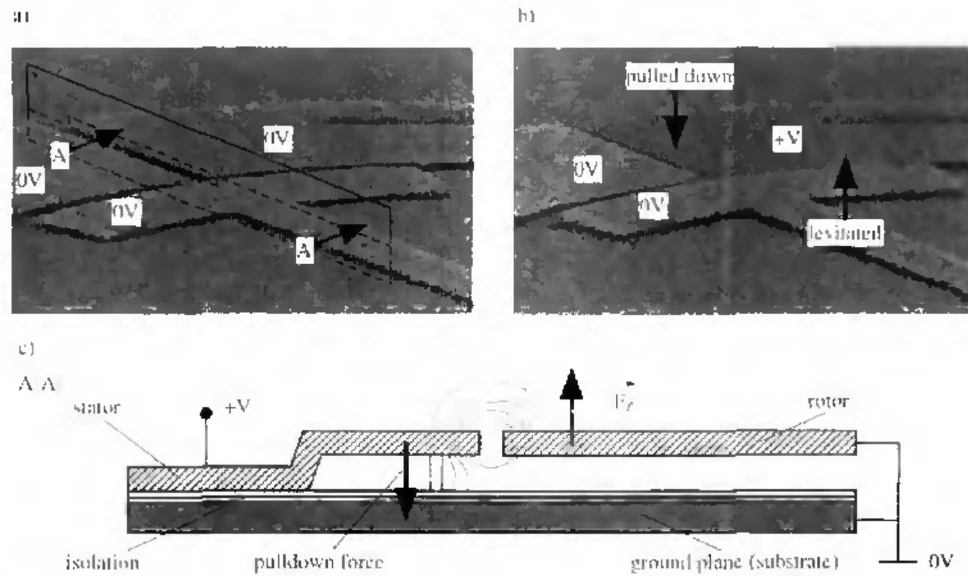

Fig. 5.11 Electrical levitation of one rotor blade of the side-drive motor of Fig. 4.2. a) Non-excited, b) Excited with 40 VDC bias: the rotor is lifted by about 0.5 µm, whereas the stator is pulled down until touching the substrate, and c) A-A cross-section.

Rotor levitation has been observed in most actuation trials of side-drive motors. Fig. 5.11 shows a detail SEM of the motor of Fig. 4.2. When the stator is excited with 40 VDC, its free end is attracted downwards against the GND plane, whereas the rotor blade is lifted up (Fig. 5.11 b) by about 0.5 micrometer. In this configuration, only fringing fields between rotor and stator over the air gap are present, the lower ones being screened by the GND plane. Consequently, the VC is higher when the rotor is lifted up from its horizontal alignment to the

stator. This effect has also been observed in electrostatic comb-structures [tan], and could be used to compensate, or at least reduce parasitic pull-down forces exerted at the rotor.

5.3.6 Electrical actuation of top- drive wobble motors

First, the 200 µm diameter, flexible-gimbals wobble motors (Fig. 4.5, left) have been excited in unipolar, 12-phase mode with up to 100 V, with and without signal overlapping, without success. Coercition of their rotors revealed blocked bearings. In some cases, the tiny torsion bars were broken under the coercition efforts. Some samples were then put in the SEM for observations. Voltages as low as 10 V are sufficient to create a visible wobbling motion of the outer ring, but no rotation.

Then the 200 µm diameter, asynchronous motors (Fig. 4.5, right) have also been excited with the same wobble commutation, without overlapping. A few continuous but irregular rotor turns were recorded for some samples (Fig. 5.12). The position versus time is measured from the video sequence. A closer view revealed the presence of wear particles along the rolling path. A red spark at the rotor edge, visible on the last video frame before stop, indicates that electrical breakdown forced here the rotor to a stop. This local breakdown of the nitride layer results probably from the action of some of the wear particles.

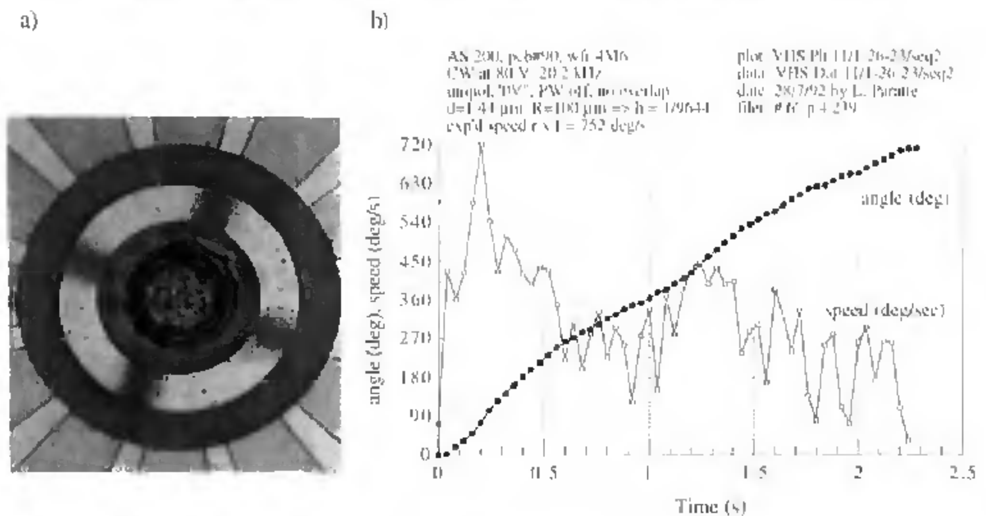

Fig. 5.12 Electrical rotation of a 200 µm ø asynchronous top-drive motor (# 90) excited in wobble mode (12 phase, unipolar, with overlap, '..00100..' pattern). a) Snapshot during rotation. b) Measured position and speed as function of time.

The data of the significant runs are given in Table 5.2. The expected output speeds are calculated by multiplying the excitation frequency by the harmonic reduction ratio (h). A harmonic reduction ratio of 1/9644 is obtained by using eq. (2.42) or (2.47) with α (the tilt

angle) = d/R, d = 1.44 μm (measured) and R = 100 μm. The motor # 5 was operated in CW and CCW directions, over a 0.01 turn range were the bearing was totally free. This is attested from its average speed, which is close to expected. The speeds of motors # 61 and 90 are quite irregular (Fig. 5.12 b) and are much lower in average than the expected, revealing again a bearing jamming. It is remarkable that the motors turned despite of this, indicating a rather high motor torque.

Table 5.2 Asynchronous 200 μm ø top-drive motors rotated in wobbling mode

motor #	61	90	5 (CCW)	5 (CW)
total number of turns	1.25	2	0.01	0.01
excitation voltage (V)	80	80	36	36
excitation frequency (Hz)	17'800	20'200	17.2	17.2
exp'd output speed (°/s)	666	752	0.64	0.64
meas'd output speed (°/s)	~ 200 ± 90*	~ 300 ± 120*	~ 0.85 ± 0.30*	~ 1.10 ± 0.40*
number of data points	~ 44	~ 57	10	7
* = S.D. (standard deviation)				

In the four runs, a slight time decrease of the speed is nevertheless observed, maybe due to a progressive blocking of the bearing by wear debris. Still, no significant amount of debris have been detected hence this hypothesis is not confirmed. The speed roughly oscillates with a period of about 30° (Fig. 5.12 b, from t = 1.6 to 2.2 s). This is probably due to the replication of stator electrodes pattern (electrode step = 30°) in the rotor, somewhat reduced by the PSG reflow (see fabrication and Fig. 5.13). When the rotor reaches its as-fabricated position, the intermediate stator valleys catch their rotor positive replica and the rotor slows down (Fig. 5.13 b). Elsewhere, the speed is normal in a rotor-stator shifted state, over a range of typ. 30° (Fig. 5.13 c).

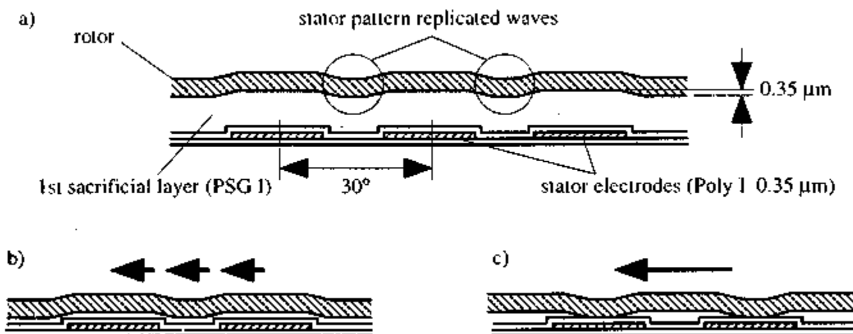

Fig. 5.13 Stator-pattern induced speed fluctuations of the rotor. a) The stator pattern is replicated to the rotor, despite of the PSG 1 planarization, b) Speed slowing when the rotor rim passes its as-fabricated position, and c) Normal speed.

5.4 Hybrid electroplated, rigid rotor wobble motors [1]

5.4.1 *Test samples and parameters*

The tested electroplated rigid-rotor wobble motors are the ones given in Fig. 4.26 (fabrication). We remind that the stators have either 0.25 μm thick LPCVD Poly-Si electrodes covered with 0.35 μm of LPCVD SiN ("poly stators"), or 0.40 μm thick evaporated aluminum electrodes covered with 0.35 μm of LTO-CVD SiO_2 ("alu stators"). The spacers and rotors are resp. 30 μm and 10 μm thick. Three types of rotors have been tested (Fig. 4.29), i.e. 2 mm ø rotors, either spoked ("R2") or having square holes ("T2"), and one spoked, 3 mm ø ("R3"). The motors are excited using only the shift register SWU (see electronics), in unipolar mode, generating the following square-wave excitation patterns:

-1/8 pattern: .. '00100000', '00010000', and so on,

-2/8 pattern: .. '00110000', '00011000', and so on,

where a '0' indicates a grounded electrode and a '1' an excited one. The maximum voltage was 90 V and the rotor is set to ground via the aluminum bridge and the spacer.

5.4.2 *General observations*

The following general observations concern any of the motors described above under any commutation scheme, unless specified. Typically, one observation is based on at least ten repeated tests per sample, on a minimum of two samples.

At low excitation frequency (1-5 Hz), the majority of the motors turn already at voltages as low as 20 V. At any frequency and voltages, the grounding of the rotor through the rolling gold-to-gold electrical contact between rotor and spacer plays a crucial role. On most non-operating motors, a high electrical resistance between the spacer and the axle was measured with microprobes, revealing a badly mounted axle. Motor operation was effectively recovered when re-constraining the axle against the spacer.

If the rotor ground contact is removed by unplugging the connection, the motor stops after a few minutes. This may indicate that either the rotor charges up and finally self-stops, or that this specific commutation scheme and/or applied voltage is inadequate for a floating rotor operation. In 50% of the cases, at low voltages, the rolling contact is lost probably because no sufficient electrostatic force presses the rotor against the grounded spacer. The hypothesis of rotor charge-up is consolidated by observing motor restarts when a very fine,

[1] Part of this work is published in {par4, par6}

grounded probe tip (length ~ 3 mm, ø 22 μm, tip radius 3 μm) was carefully approached to discharge the rotor without significant mechanical interfering. Frequent self-stops are also observed for motors with a too small bearing clearance, preventing the rotor to wobble freely around the axle.

At low frequency and at voltages comprised between 40 and 90 V, the poly stator motors stop after typically ten minutes. They restart when the voltage is increased, but stop again after a few minutes. This behavior can be repeated until reaching 90V. If the motor is stopped a few minutes with all electrodes grounded, normal operation is recovered. Alu stator motors can be operated distinctively longer than 10 minutes before self-stopping. Much longer non-stop operation times for both motor types are reached at higher frequencies, as shown in Table 5.3.

Table 5.3 Record of long-time runs of 2 mm ø electroplated wobble motors

motor #	1	2	3
stator - rotor type	poly - T2	alu - R2	alu - R2
voltage (V) - commutation	80 - 2/8	80 - 1/8	40 - 1/8
excitation frequency (Hz)	250[1]	100[1]	29
measured output speed (rpm)	13.5	5	1.7
expected output speed (rpm)	6.8	2.7	0.8
number of self-stops [2]	2	none	none
total operation time (hours) [3]	26	12	408

[1] maximum before mech. cutoff [2] without counting operator on-offs [3] not limited by motor failure

The expected output speeds are calculated in the same way as for the polysilicon-based wobble motors, i.e. by multiplying the excitation frequency by the harmonic reduction ratio (p). A harmonic reduction ratio of 1/5000 is obtained by using eq. (2.42) or (2.47) with α (the tilt angle) = d/R, d = 30 μm (spacer thickness) and R = 1000 μm. Curiously, the measured speed is always higher than the expected; this is analyzed later. The maximum achievable rotor speed of 5 rpm before cutoff (motor #2) may be at best compared to the calculated value of chapter 2, Table 2.2, of 10 rpm (1.05 rad/s). These values differ by a factor of two, but the present isolation material and thickness are different from the modelization as well. The comparison between theoretical and experimental data is explored in a further section.

5.4.3 RC charging of the insulator

It has been observed that : 1°) At low frequency, an always higher voltage is needed to keep the motors turning, 2°) Normal operation is restored when setting a few minutes all electrodes to ground, and 3°) "High" frequencies (a few tens of Hz) lead to significantly longer non-stop operation times. All three observations logically suggest that progressive charge accumulation of the isolation material takes place. Another hint in this direction is that the three effects mentioned hereabove are systematically less accentuated for dioxide-covered (alu) stators than for nitride-covered ones (poly), hence proving an isolation material-dependent behavior. Moreover, silicon - silicon nitride interfaces are also described as having a charge storage effect [sze2].

Anderson et al. [and] studied this problem of attachment/detachment of a conductive rotor over insulating material. They propose an elementary actuator model incorporating insulator surface charge accumulation mechanisms. Aside from charge generation through air gap breakdown or contact electrification (the ubiquitous free charges transfer between dissimilar materials rubbed together), the authors mention RC charging: "An applied electric field across the insulator causes small but finite currents that in turn produce surface charge. This charge tends to decay according to the RC time constant of the insulator. During attachment/detachment cycling, the processes of accumulation and decay compete, potentially resulting in a ratcheting effect that, cycle after cycle, increases the surface charge." They model this accumulation effect and demonstrate that the actuator, being switched synchronously, hence at its maximum speed, can be operated non-stop even with a certain amount of RC sticking, under certain insulator material and air gap conditions.

In our case, the mechanism of RC charging is evidenced by the fact that operation can be recovered by connecting all electrodes to ground for a while, attesting discharge current flow through the insulator. But the charges seem to accumulate only at low frequency, as shown by the rotor self-stopping after a few minutes, whereas they are (much) lower and remain constant at a higher frequency. Therefore, referring to Anderson et al., it seems that at frequencies near the mechanical cutoff, we fortunately operate in a stable, i.e. non self-stopping, attachment/detachment cycle, with still a certain amount of sticking.

In view of all the above statements, it seems then evident that the unwanted RC charging could be drastically reduced or eliminated when selecting an insulator with especially high electrical resistance, hence of high purity, and avoiding charge-storing interfaces like Si-SiN. This further implies careful electric characterization of candidate insulators. Another possibility includes the switching of high-frequency bursts instead of square waves to the electrodes, with the same isolation materials.

5.4.4 Wear

After a cumulated test time of 26 hours, the parts of motor # 1 of table 5.3 (poly - T2) have been observed with a microscope, at the wear locations (circled in Fig. 5.14). A 0.6 µm deep, 200 µm diameter groove results from the grinding of the spacer edge into the rotor (Fig. 5.15). This means that the gold layer of 0.1 µm has been pierced through, and that the electrical contact has moved from gold-gold towards nickel-nickel. This did not prevent the motor from turning.

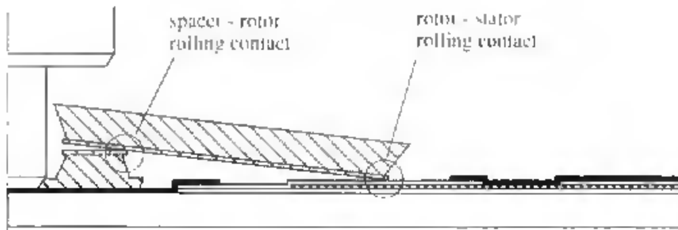

Fig. 5.14 Half electroplated wobble motor cross-section showing the locations subject to wear (circled).

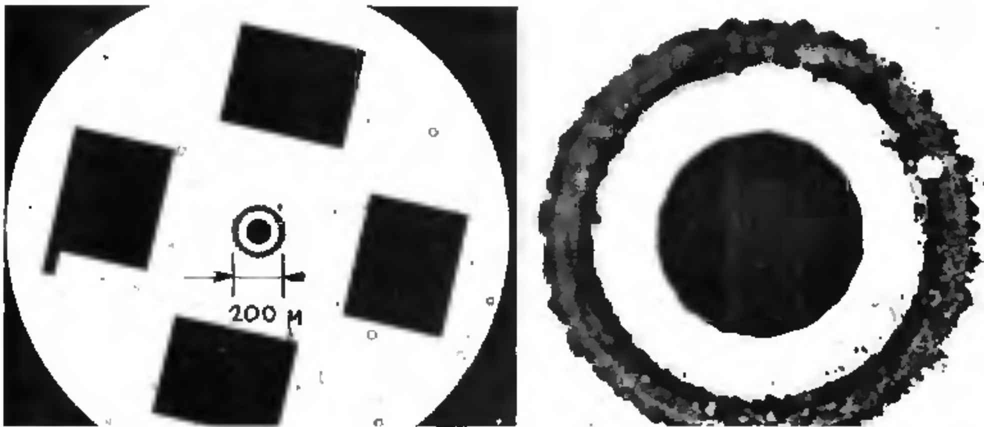

Fig. 5.15 Bottom view of a 2 mm ø electroplated WM after 26 hours of operation at 80 V (motor T2 # 1 in Table 5.3). Left: ensemble view. Right: enlargement showing the 200 µm ø wear groove, 0.6 µm deep, provoked by the spacer-rotor contact.

The rotor outer edge has been beveled through wear against the harder silicon nitride. The 48-edges polygon which formed the rotor edge (see Fig. 4.33) was transformed into a smooth, circular bevel strip by wear (Fig. 5.16), whereas no significant degradation of the 0.35 µm thick silicon nitride layer was observed. Only some gold particles of the rotor seed layer have been shed away and pressed onto the rolling path (Fig. 5.17). As can be seen, a larger gold particle, probably also squeezed between rotor and stator, provoked a local

breakdown of the nitride layer, which borders have been blackened. Even if this event may have provoked one of the two self-stops mentioned in Table 5.3, the motor could be operated further.

Fig. 5.16 Enlarged view of the rotor edge of Fig. 5.15, left. Three of the 48 edges forming the rotor circle are visible. The edge has been beveled through the rolling against the stator.

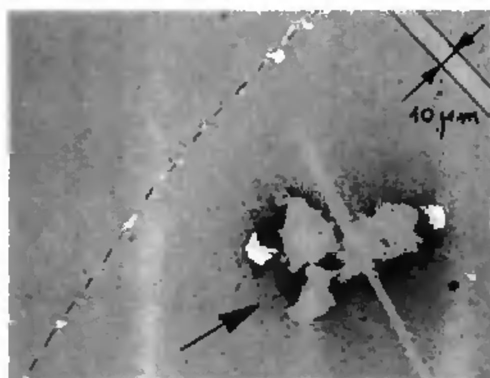

Fig. 5.17 Enlarged view of the stator surface (motor T2 # 1 in Table 5.3). Gold particles are visible along the rotor-stator rolling path (broken line). Two adjacent electrodes are separated by 10 μm as shown. A gold particle has provoked a local piercing of the nitride layer (arrow).

This wear state is positive for many reasons. Above all, no significant changes in the reduction ratio were observed. The nickel-nickel rotor-spacer rolling contact seems to be stable enough to provide the necessary electrical contact over quite long times of operation (408 hours). If the stator insulation material would wear out faster than the rotors rim rather than the other way (our case), the motor lifetime would be strongly reduced.

5.4.5 Speed measurements

The output speed (ω_z) of a 3 mm ø, spoked rotor motor with a poly stator has been measured as a function of the excitation frequency, with a 1/8 commutation and at 50 V (Fig. 5.18). The speed measurements are made by analysis of recorded video images. To compensate for isolation charge-up effects at low frequencies, the motor is grounded a few minutes between each measurements. The reduction ratio is quite independent of the frequency. A least squares linear fit of the experimental points gives an inverse of the reduction ratio, 1/h, of 1490 ± 176 S.D. This value is still far from the expected value of 1/h = 5000, obtained by calculating with d = 29 µm and R = 1500 µm. A closer value of 2272 ± 197 of measure error is found by measuring the tilt angle via microscope focalization of the tilted rotor. Still, this value does not match the one found by speed measurements.

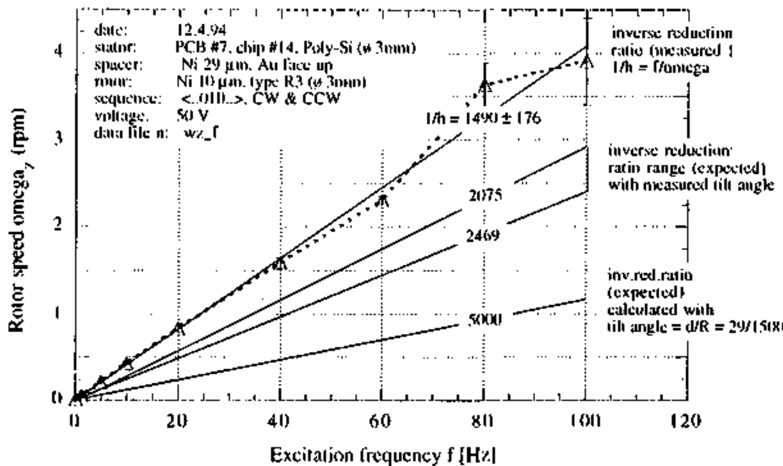

Fig. 5.18 Measured output speed as a function of the excitation frequency for a 3 mm ø wobble motor (type R3).

The differences between measured and expected output speeds, as shown in Table 5.3 and in the speed versus frequency graph of Fig. 5.18, could be due to a rotor slip, which amount is moreover independent from the excitation frequency, hence occurring during one step. This is plausible from the graph of Fig. 2.24, since a 45° step begins with a higher motive than adherence torque. However, to attest this, a full dynamic simulation of the rotor step advance, namely in function of the friction coefficient would be necessary.

5.4.6 Torque measurement by spring deformation

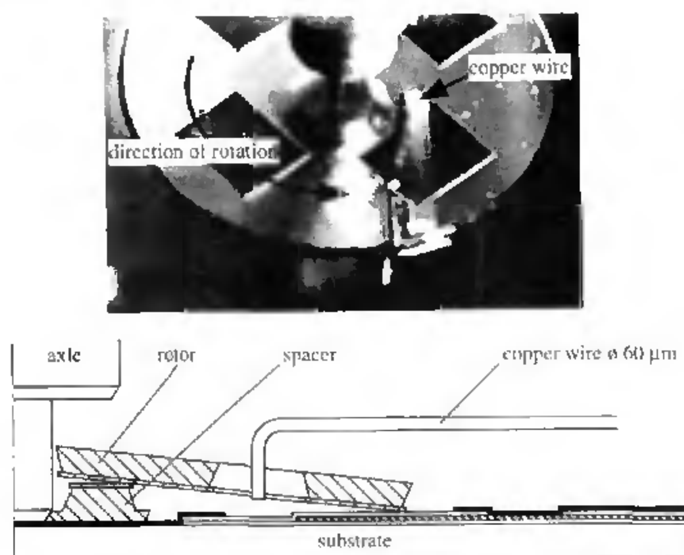

Fig. 5.19 Torque measurement using a calibrated spring lever. The CCW rotating rotor (T2, ø 2 mm) drives the lever in lateral flexion.

The torque of motor #1 of Table 5.3 has been measured by deformation of a force calibrated spring (Fig. 5.19). The spring is a copper wire of 60 µm diameter, deformed in flexion when introduced in the rotating rotor, until the rotor stops. The value of the delivered torque is measured knowing the wire lateral flexion spring constant and the level arm at the rotor (here, approx. 0.5 mm). The spring constant for this wire is measured using a precision balance (Mettler AE 240) and is equal to 2.14×10^{-5} N/mm. With the motor # 1 operated in the conditions of Table 5.3, a deflexion of 1 mm is measured (average over 10 runs). This corresponds to a torque of 1.07×10^{-8} Nm or 11 nNm. The calculated average motive torque for this motor amounts to 0.46 µNm using the same formulae as for the motors of Table 2.2, but with $V = 80$ V, $\mu = 0.5$, $\varepsilon_r = 3.9$, $\theta = 45°$, $d = 30$ µm, $R = 1$ mm, $R_i = 0.8$ mm and $d_i = 0.35$ µm. The calculated value is hence 50 times higher than the measured. The reason for such a low experimental value is certainly that the wobbling movement is disturbed by large vertical forces exerted by the wire. We can thus conclude that this measure is not representative. Non-contact methods are certainly more promising.

5.4.7 Torque measurement by optical detection and parameter extraction

Introduction

This non-contact method basically consists in measuring optically the mechanical step response φ(t) of the motor (see Fig. 2.25), and in fitting this experimental data to a theoretical model so as to extract the parameters of interest, i.e. mainly the average output torque. This is carried out hereafter for the motor #2 of Table 5.3, having an alu stator and a R2 (spoked) rotor, excited with the 1/8 commutation and at voltages comprised between 20 and 60 V, with the following input parameters: $R = 1$ mm, $R_i = 0.8$ mm, $\mu = 0.5$, $d = 30$ µm, $\theta = 45°$, $d_i = 0.35$ µm, $\varepsilon_r = 3.9$ (SiO_2), $t = 10$ µm and $\rho = 8900$ kg/m^3 (nickel).

Experimental set-up

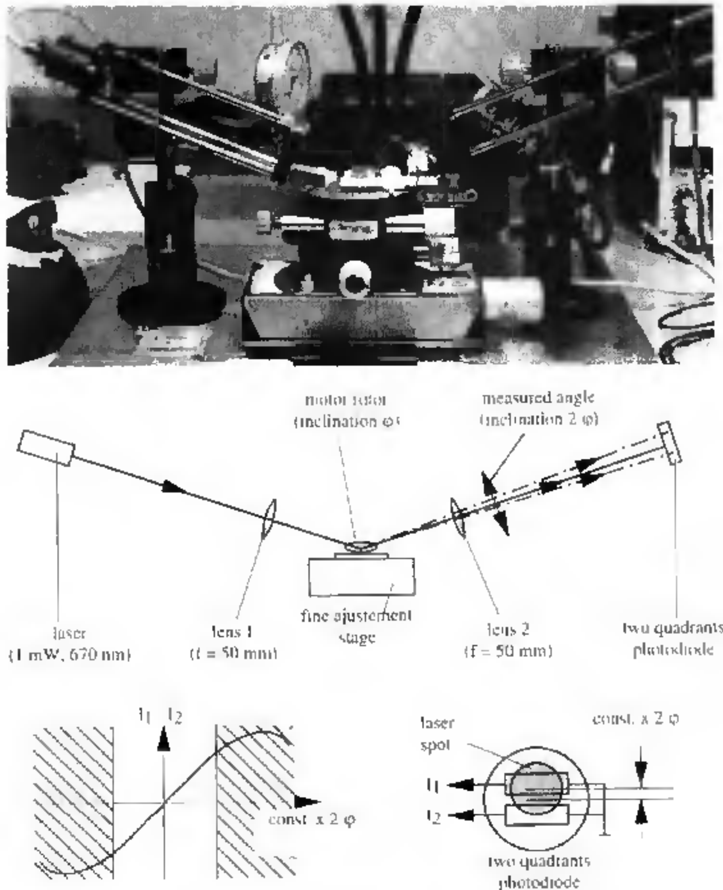

Fig. 5.20 Optical bench for the measurement of the motor mechanical step response.

First, an optical bench has been set-up for the measurement of the mechanical step response φ (t) (Fig. 5.20). A laser beam (670 nm, 1mW, type LM 670-E.09.V.M from Quadriga GmbH) is focused on the rotor rim, reflected by it and recollimated to hit a two-quadrant photodetector (BPX 48 silicon diodes from Siemens). Both diodes of the detector deliver currents in function of the spot position, so that their difference I_1-I_2 is proportional to the spot position, itself being proportional to twice the rotor tilt angle over a range limited by the shadowed zones in the I vs φ graph (Fig. 5.20 bottom). The current difference is converted to a voltage difference by a dedicated circuit using operational amplifiers (circuit bandwidth: 300 kHz). The motor is fine positioned w.r.t. the optics in the yaw, pitch and height coordinates by means of micrometer screw-driven stages, so that the delivered signal over one rotor step stays in the linear differential current range of the photodetector. The response signal is then triggered with the excitation and displayed on an oscilloscope. Fig. 5.21 shows the response of the motor to a 20 V step voltage.

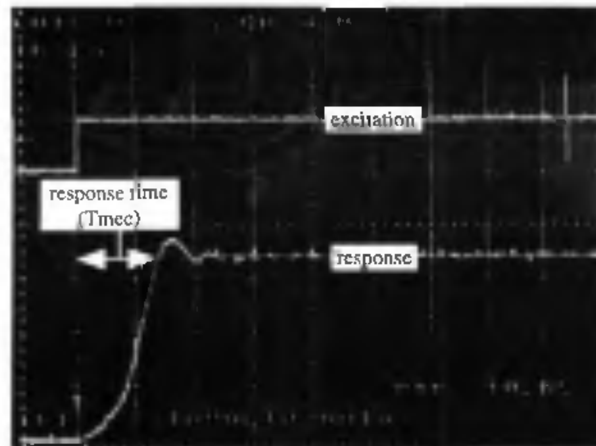

Fig. 5.21 Measured rotor step response (φ (t)) for a low frequency excitation (1 Hz) and 20 V, for the motor described in the introduction. Horizontal axis: time (2 ms/div), vertical axis: excitation and response signals. This last is proportional to the rotor inclination (or tilt) angle (2 V/div).

Determination of the parameters to be fitted

The step response is then simulated using the ESMOTOR program (see 2.3.6) with V = 20 V and f = 7.2 x 10^{-14} Nms. The result (Fig. 5.22) is a much less damped oscillation than the measured (Fig. 5.21), indicating a strong mismatch between experiment and theory.

What is then incorrect, the model or its parameters ? In fact, we can still keep the model and try to adjust some parameters so as to fit experimental points (which should be more numerous than the parameters). If the model is wrong, the points won't fit with a good correlation. The dynamic model is the 2nd Newton's law around the y'-axis, the differential eq. (2.59) with the explicit torque values:

$$I_{y'} \frac{\partial^2 \varphi}{\partial t^2} = -f \frac{\partial \varphi}{\partial t} + V^2 m_{my'}(\varphi), \qquad (5.2),$$

where $m_{my'}(\varphi)$ is the motive torque around the rocking axis normalized w.r.t. the voltage squared. The inertia and the voltage are precise and well-controlled values, whereas the normalized motive torque and the damping factor are subject to changes. The damping factor is likely to be much different than modeled, considering its very questionable evaluation (Fig. 2.27) and possible unknown effects like squeeze film. Concerning the electrostatic torque, we can suppose that its distribution w.r.t. the contact point coordinate is well calculated, but its absolute value should be multiplied by a correction factor, c^2, between 0 and 1, to take into account the parasitic RC charging effects, as explained hereafter.

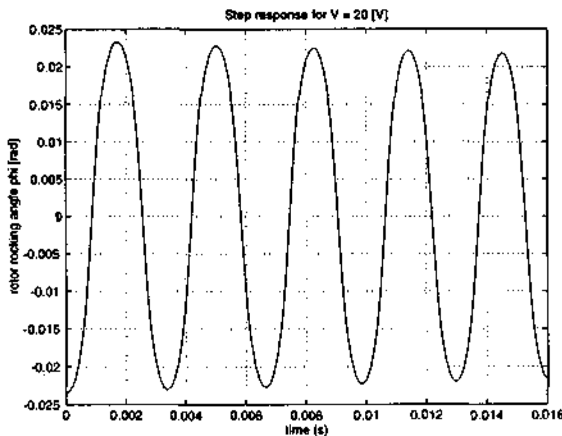

Fig. 5.22 Calculated rotor step response with the same motor parameters as for the measure of Fig. 5.21 (see introduction). Horizontal axis is 2 ms/div as in Fig. 5.21.

We deduced that the amount of parasitic charge on the insulator surface remains constant, otherwise the rotor would be stopped. Still, this electric charge being distributed uniformly over each of the stator electrodes, it decreases the apparent motor torque produced by the excited electrodes. The rate of RC charging, hence the amount of charges, are logically expected to be proportional to the voltage. Therefore, we introduce a correction factor of the apparent voltage, which squared value is the correction factor of the torque. The second member of the above differential equation writes then $(cV)^2 m_{my'}(\varphi)$, with c taking a value between 0 and 1.

As a consequence, the two parameters to be fitted with experimental data are c and f. If the fitting is successful, these values directly yield the experimental torque and damping factor.

Fitting procedure and extracted torque

The ideal would be to fit directly experimental $\varphi(t)$ points, like in [tav2]. But such measured responses vary so much step after step, so that it is nearly impossible to produce an acceptable averaged graph easily. We choose to rather measure from each $\varphi(t)$ graph the response time, T_{mec} (Fig. 5.21), and to fit this variable versus the excitation voltage. This is justified since in highly damped motions, this response time strongly depends on the voltage. The motor is thus excited at various voltages (20, 24, 30, 32, 40, 60 V), at low frequency (1 Hz) with about 20 steps per voltage. The oscilloscope image is recorded with a video camera to VCR. Selected video frames are then transferred from the VCR to a computer using a video image processing software. The response times are then measured graphically on the computer image, and averaged. Table 5.4 gives the measurements results.

Table 5.4 Measured response times as function of the voltage (motor # 3 of Table 5.3).

Voltage (V)	Number of samples	T_{mec} (ms)	± S.D. (ms)
20	12	3.13	0.36
24	10	2.09	0.31
30	7	1.30	0.12
32	19	1.39	0.19
40	6	0.99	0.15
60	8	0.58	0.09

A fitting routine has been added to the ESMOTOR simulation program, to allow iterative fitting of the differential equation coefficients c and f to the measured values of Table 5.4, starting from initial values. One iteration consists of the following steps:

1) Compute the $\varphi(t)$ step responses for all 6 voltages by solving the differential equation,
2) Extract the 6 T_{mec} times from these graphs,
3) Calculate the least squares difference with the experimental T_{mec} times,
4) Evaluate the differences with c and v values of precedent iteration
5) Stop the iterations if this difference is lower than a user-fixed error
6) Change the c and f parameters to minimize this difference (simplex algorithm).

The result is shown in Fig. 5.23, after a total of 134 iterations and with start values of $c = 0.6$ and $f = 1.3 \times 10^{-10}$ Nms. Final values of $c = 0.6473$ and $f = 1.455 \times 10^{-10}$ Nms are found for this motor. This further implies that the real motive torque is 42% (c^2) lower than

expected, i.e. that the average motive torque at 80 V of excitation is 0.2 μNm instead of the 0.46 μNm expected. The damping factor is about four order of magnitude higher than expected, with the above mentioned value instead of the calculated 7.2 x 10^{-14} Nms (Table 2.2). From this last observation, its seems that the effects due to the substrate proximity (squeeze film effects) which where neglected in the model of Fig. 2.26, reveal in fact to be of prime importance.

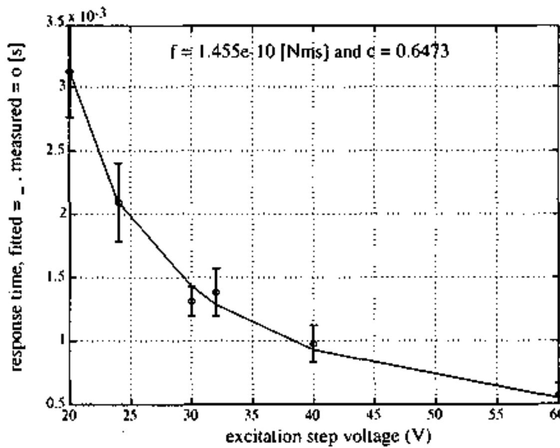

Fig. 5.23 Fitted experimental response times of Table 5.4, as function of the excitation voltage (motor # 3 of Table 5.3).

5.5 Hybrid electroplated, flexible rotor wobble motor coupled to a gear train [1]

5.5.1 *Test sample and parameters*

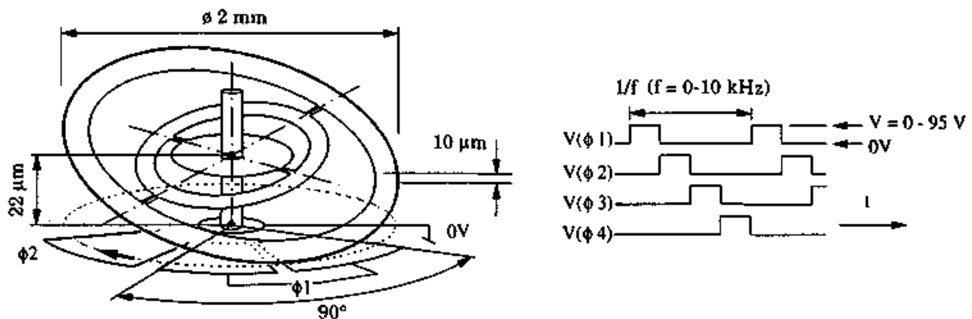

Fig. 5.24 Testing scheme and description of the flexible rotor WM. The 1/4 commutation pattern is illustrated here.

The electroplated flexible rotor WM coupled to a gear train (Fig. 4.27) was tested with the demultiplexer SWU (Fig. 5.1), with 1/8 and 1/4 commutation patterns, in unipolar mode, as for the rigid rotor motors (see sect. 5.4.1) with up to 95 V (Fig. 5.24). The 1/4 patterns go like '11000000', 00110000', etc. where a '0' indicates a grounded electrode and a '1' an excited. The stator has 0.25 µm LPCVD Poly-Si electrodes covered with 0.35 µm of LPCVD SiN ("poly stator"). The open gap length is 20 µm. The rotor has 2 mm diameter and is 10 µm thick (Fig. 4.29). The rotor is grounded by the central stator metallization via the substrate.

5.5.2 *Tests without lubrication*

In the first tests, the gears and bearings were not oil-lubricated. With the 1/8 commutation, no wobbling is observed even under 95 V. The 1/4 commutation reveals more successful. At low excitation speeds, the vertical wobbling motion of the rotor is observed up from 90 V. A lateral unwanted wobbling of the rotor axle, due to the bearing clearance (about 10 µm) is also observed. These two wobblings generate inverse propulsion torques (Fig. 5.25). This is well illustrated by irregular rotation in both directions for excitation speeds from 0 to around 800 Hz. At about 1 kHz, the wanted rotation overcomes the unwanted, and the rotor drives the gear train at the average speed of 12 rpm (at pinion). The rotation is quite

---

[1] Part of this work is published in [par5]

irregular, because of the apparently too stiff torsion bars that do not allow the rotor to fully wobble. The speed figure fits well with the one calculated from the excitation speed and from the rotor geometry. The rotation obtained around 1 kHz excitation speed tends to show that the elastic rotor acts as a resonator with a tuning frequency of about 1 kHz at 90 V excitation.

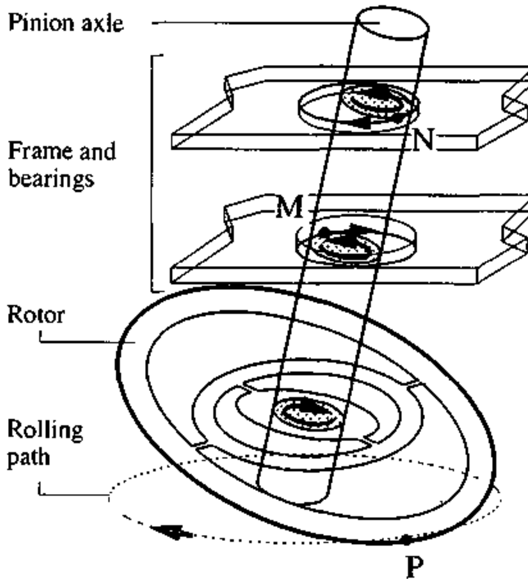

Fig. 5.25 Mechanism of antagonistic wobble torques generated by the rotor (contact point P) and by the lateral wobbling in the bearings (contact points M and N).

5.5.3 Tests with lubrication

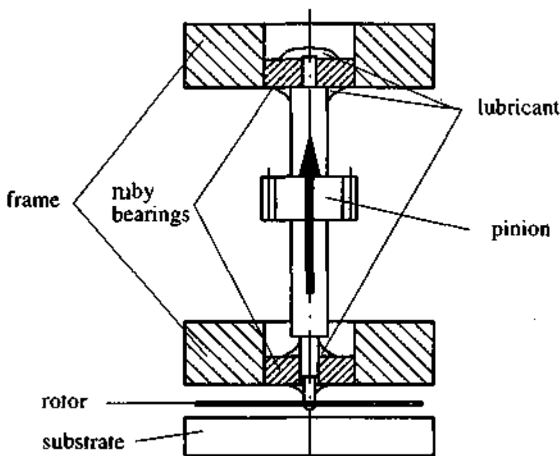

Fig. 5.26 Scale view of the lubricated rotor stage. The rotor axle is lifted upwards by the meniscus forces of the liquid lubricant.

The bearings were then oil-lubricated (Synt-A-Lube oil). This caused the rotor axle to be pulled away from the stator several tens of µm, because of meniscus forces at the top bearing (Fig. 5.26). A probe needle was used to push the rotor axle down, but this hindered electrical rotation. In this pulled-up position the rotor could be electrostatically excited at rocking eigenfrequencies around the x and y torsion bars. The vertical rocking peak-to-peak amplitude at the wobbling ring edge could be measured under binocular (Fig. 5.27).

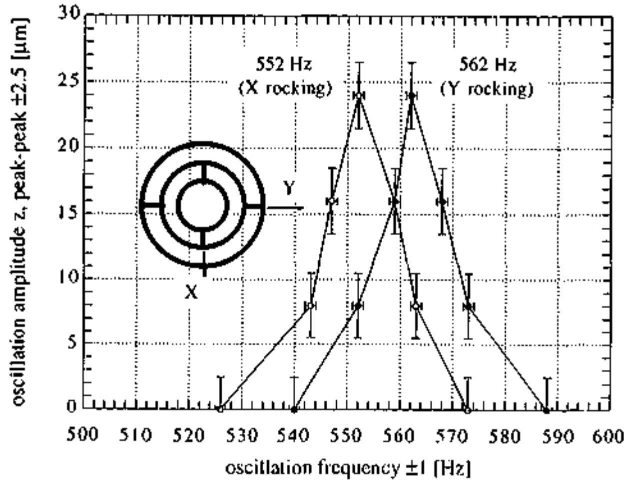

Fig. 5.27 Rotor rocking eigenfrequencies around the x and y torsion bars of the gimbals.

Two different eigenfrequencies of resp. 552 and 562 Hz, corresponding to the x and y rocking motions around the torsion bars have been measured. Deviations in the torsion bar dimensions, in particular the thickness, could produce such difference. While x-rocking, both the outer and the intermediate rings move, whereas in case of y-rocking, only the outer wobbling ring moves. The calculated frequency difference due to inertia between these two modes is only of 0.3%. Hence, the air drag probably produces the frequency difference.

Resonating the structure in these modes could be further used to extract the rotor material parameters. The fitting with a dynamic model of eigenfrequencies measured under vacuum could yield the values of the specific mass and the Young's modulus.

5.5.4 Rotor electromechanical static displacement measurements

In order to better understand the unit testing described above, a static test has been performed. A rotor with the same dimensions (10 µm thick) has been simply glued to a stator with conducting epoxy, at the same open gap length of 20 µm (Fig. 5.28). Thus the rotor is only able to tilt. The vertical displacement of the rotor has been measured at the rotor extremity, as a function of the applied DC voltage on one stator electrode (width = 45°). The displacement is measured optically with a confocal microscope (UBM-Microfocus®). The

results are shown in Fig. 5.28. A pull-in voltage of 91 V and a pull-out voltage of 40.2 V are measured. This last value is much higher than the calculated 6 V (sect. 2.3.7), indicating that the torsion bars may be in reality much stiffer. Reconsidering the bar dimensions (200 x 50 x 10 μm^3), one may calculate a closer value to the measured one by considering a plate rather than a bar under torsion for the spring force model.

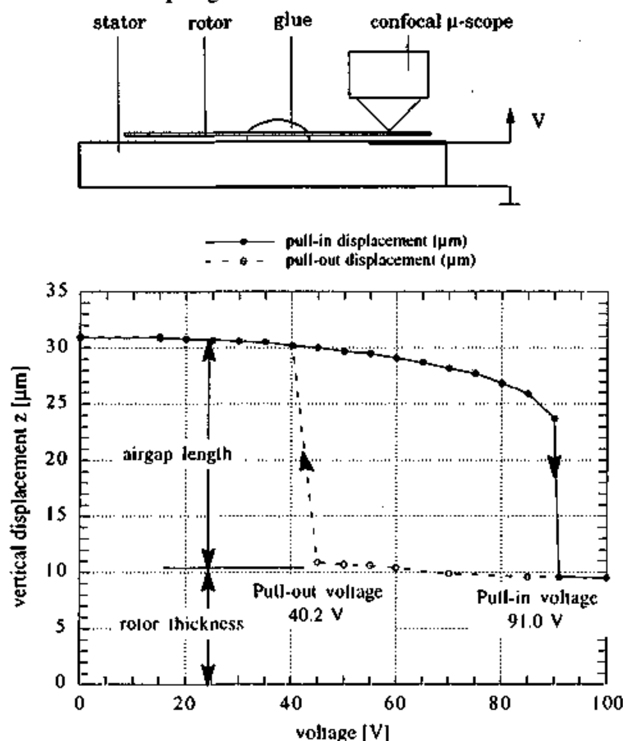

Fig. 5.28 Rotor static voltage vs. displacement measurement.

5.5.5 *Discussion*

For the first time, an micromachined electrostatic micromotor drove a mechanical load. In the rotation test at low frequencies (1Hz), an electrode having 90° of width excited at 90 V is needed to obtain the rotor tilt and wobbling, whereas in the case of the static test, the rotor pull-in is already obtained at the same voltage for only 45° excited electrode width. The commutation scheme is of importance. Rotation is only obtained around a given excitation frequency (1 kHz), indicating that wobbling inertial effects of the rotor add to the resulting contact force. The stiffness of the torsion bars seems still too high and consequently the rotor should be redimensioned. Unwanted lateral wobbling at the bearings, generating opposite propulsion torque is observed when there is some bearing clearance. This effect should be considered in case of a redesign.

Chapter 6 - Conclusions

The goal of this thesis was the design, fabrication and testing of practical electrostatic rotary micromotors. Using silicon processing techniques for their fabrication is one possibility. In contrast to other transducers, electrostatic micromotors do not (yet) represent important market sizes. Therefore this work is still exploratory and is also intended to give some basements for future ideas of applications. Some of the interesting observations and conclusions of each chapter are regrouped hereafter.

6.1 Motivations

There are growing needs and interests towards handling of very small objects with high precision (biomedicine, genetics, surgery, etc.). In this respect, human-size micromanipulators are far from being effective. When high precision is required, microobjects should be moved around by manipulators of the same size. Micromachining of silicon - derived directly from IC production techniques - is just the appropriate tool for the fabrication of mechanical devices down to a hundred of microns, with a micron or better of precision. These arguments, besides of low consumption and low production costs, justify the needs for *microactuators*.

6.2 Scaling laws

Numerous aspects of micromachining of electrostatically driven rotary micromotors have been studied. Scaling laws based on the maximum voltage before breakdown (Paschen law) for the electrostatic, and on the maximum coil temperature for the magnetic are used to extrapolate the electromechanical behavior of respectively electrostatic and magnetic motors of centimeter sizes down to hundreds of micrometers, a scale factor of 1/100.

It comes out that electrostatic forces scale *theoretically* better than magnetic for micrometer-sized air gaps. After Fig. 2.4, if the rotor size is 100 times the air gap length, the scaling laws predicts that an electrostatic micromotor with 2.5 µm air gaps and an outer diameter of 250 µm could deliver up to 30 nNm against only 0.7 nNm for a magnetic motor of same dimensions. Similar torques are delivered by motors of both principles if they have 7 µm long gaps (rotor diameter 0.7 mm). To still keep acceptable magnetic torques, the size of the coil must not be reduced, as exemplified by wristwatch Lavet motors (Fig. 2.2). This

implies that magnetic micromotors cannot be built as compact as electrostatic ones, unless superconductive coils are used. The maximum torque would then be limited by the magnetic saturation level in the gaps.

6.3 Modelling

Polysilicon surface-micromachined integrated micromotors have been analytically modelled. Variable capacitance, synchronous stepper side- and top-drive motors are compared. One major problem is that the forces intended to align rotor to stator teeth also provoke large unwanted reaction forces at the bearings, because the bearing play of these motors is still important compared to the rotor diameter. In fact, the bearing clearance, the rotor size and the surface roughnesses should be scaled homothetically from well operating miniature motors. However, it is still difficult to build precise bearings for rotors of hundreds of micrometers in diameter. Electric levitation and frictional studies are then adequate to solve the problem. The former adds more complexity to the motor, hence the latter remains.

Side-drive VC micromotors are successful, because of counterbalancing side-pull forces that reduce the friction, if the bearing play is minimum [tav2]. The top-drive motor construction proposed in this work, where the rotor is simply situated over stator electrodes embedded in the substrate, is taking a large advantage of the planar polysilicon process.

Maximum net torque figures over one step for 200 μm diameter rotors and 1.5 μm long air gaps and 100 V excitation voltage (much lower than the theoretical breakdown for this gap after Paschen's curve) are of 0.2 nNm for side-drive motors against 0.015 nNm for top-drive motors (Fig. 2.16). Despite of its higher torque, the top-drive motor needs a much lower friction coefficient to be operated continuously than the side-drive (Fig. 2.14). The side-drive torque can be increased by adding supplementary gaps, as exemplified by the proposed comb architecture (sect. 2.2.6).

These calculated torque figures are still far below the theoretically achievable ones cited above for two reasons. First, breakdown voltages in practical motors are much less than the ones predicted by the Paschen curve, because of local field concentration in the vicinity of sharp corners. Second, low power, high frequency (~200 kHz) and high voltage (~500 V) switching ICs are not very common components. Low-power, high-voltage (75 V) CMOS circuitries are currently studied for these applications [dec].

Vertically wobbling micromotors have been designed and modelled. These take advantage of friction and planar processing. Both flexible and rigid rotor motors are investigated. The calculations for 200 μm diameter, flexible rotor polysilicon motors give an average torque estimation of 48 nNm under only 75 V, at relatively low speeds of a hundred of rpm (Table 2.2). Larger rigid rotor motors of 1, 2 and 3 mm diameter are also simulated in

view of wristwatch applications, where typically some one microwatt is needed to reliably drive the seconds hand of a wristwatch. The calculated maximum torque and speed for a 2 mm diameter rotor are respectively 1 μNm and 10 rpm under 75 V excitation, which corresponds to a power of 1 μW. A low pull-in voltage of 6 V is calculated for a 2 mm diameter flexible gimbals rotor, intended to be mounted on a miniature gear train.

6.4 Friction

The chances for a top-drive motor to turn are directly dependent upon friction. Therefore, the dry static and dynamic friction coefficients of polysilicon on itself, polysilicon on silicon nitride, nitride on itself and molybdenum bisulfide (MoS_2) on itself (solid lubricant for space applications) have been measured with a plate-on-disc macroscopic method. The samples had the same surface aspect than the later fabricated polysilicon motors. The test apparent contact pressures were around 45 kPa, which is about the same value as at the bushings of the 200 μm top-drive motor excited with 100 V.

Some of the measures were insignificant because the sharp edges of the plate samples ground into the disc surface. The dynamic coefficient values lie between 0.22 and 0.55, which is a very wide range. The average values for polysilicon on itself (0.28 ± 0.09) are surprisingly lower than the values of polysilicon on nitride (0.35 ± 0.12), which are in turn lower than nitride against itself (0.50 ± 0.09). This last result is not surprising. Hot-pressed silicon nitride has a high coefficient in gases containing water (ambient air) and a tendency for tribological welding: a third compound is formed by tribochemical reaction, which increases the coefficient [fis]. This combination should therefore be avoided.

The native oxide at the polysilicon surfaces, as well as adsorbed water may be responsible for a lower friction coefficient of polysilicon on itself. But concerning wear, this material combination should be avoided.

The MoS_2 samples exhibited quite high values (0.29 ± 0.03) because of the ambient humidity. To control the humidity would increase the motor complexity too far. Other solid lubricants look more promising in terms of coefficient and wear, like carbon chain monolayers (C_{22}) who have coefficient values against themselves as low as 0.1 and are already characterized over long sliding distances [zar].

Hence, polysilicon on nitride seems to be the best combination for the polysilicon motor bushings. A better evaluation of the worn surfaces (SEM), a much larger number of runs and long-life tests are still needed to improve such observations. To avoid grinding problems of the Tribometer test, a round ended silicon pin should be used instead of a chip.

6.5 Fabrication

Polysilicon surface micromachining has revealed satisfactory for the fabrication of the modelled side-drive, top-drive, comb-drive and wobble motors. Reflow of sacrificial layers has been characterized and used to improve critical step coverage, namely for the comb-drive motor (Fig. 4.18). The bearing was very critical to processing defaults (Fig. 4.22).

Electroplated rigid rotor wobble motors have been successfully assembled on silicon stators. The assembly feasibility of conventional machined and micromachined, silicon-based parts into a hybrid motor has been demonstrated. However, this solution is no more viable for the production of a large amount of pieces. A fully integrated, millimeter size version would be a better solution.

The flexible rotor version which was mounted on a miniature gear train proved very difficult to be assembled by hand, especially for gluing the rotor to the pinion axle. The size of the conventionally machined gear train is still much bigger than the volume occupied by the rotor. Therefore, here again, an integrated version comprising all elements (rotor, stator, pinion, output axle, bridge) is of interest.

In case of a higher integration level for the electroplated motors, a multilevel electroplating technology with vertical sidewalls and thicknesses per level ranging up to 100 μm would be ideal. Some decisive steps in this direction have already been taken by using dry film resist [lor]. Processes using the positive spin-on resist of the present work (AZ 4562) have been studied to obtain vertical sidewalls [beu].

6.6 Testing

For some of the polysilicon motors samples, destructive breakdown of the stator-to-ground plane isolation (3000 Å of SiO_2 and 2000 Å of SiN) was observed rather than in the 1.5 μm long air gaps. The applied voltage was 110 V, which corresponds to breakdown fields of 256 and 166 MV/m respectively in the oxide and nitride, which are far below the usual strengths of 1000 MV/m reported in [sze1]. Local defaults of processing may be imputed.

Most of the polysilicon motor bearings where jammed, preventing any further investigations in electrical actuation. The most probable cause has been identified as a polysilicon grain growth during the 1100°C drive-in. The grain size observed on SEMs of the bearing hole (Fig. 5.8) is estimated to lie between 100 and 500 nm, which also corresponds to the observed roughness. The lateral bearing play being equal to 200 nm, it is then clear that the bearing will jam as soon as rotated. The error was to perform the 1100°C drive-in *after* structuring the bearing hole instead of the reverse way.

Even with half-blocked bearings, some of the 200 μm diameter wobble motors could be electrically rotated, indicating the very strong torques of this design (Fig. 5.12).

The electroplated rigid rotor wobble motors have been rotated much more successfully, over quite long periods of time (maximum of 408 hours, Table 5.3). The observed rotation at speeds around 10 rpm is very regular. The contact of the rotor to ground reveals essential for proper operation. The motors worked more regularly when driven at frequencies near to their mechanical cutoff and at 90 V, with a 2/8 commutation. At low frequency, the operation time was only a few minutes. Progressive RC charging of the rotor-stator separation oxide is identified as the most probable cause for motor self-stops at low frequencies. This unwanted polarization could be drastically reduced or eliminated if a very pure insulator is used, or by pulsing high-frequency bursts instead of square-waves to the electrodes.

The measured harmonic reduction ratio is quite independent of the excitation frequency. However, the calculated value is different by nearly a factor of two (Fig. 5.18). The difference could be explained by rotor slip over one step. Mechanical measurements of the torque by deformation of a lever spring are irrelevant, because the vertical wobbling motion is disrupted. Therefore, the developed optical measurements of the step response with parameter extraction is a more suitable method. The average motive torque at 80 V of excitation is 0.2 μNm instead of the 0.46 μNm calculated, for a 2 mm diameter spoked rotor. The oscillation damping factor is about four orders of magnitude higher than expected, indicating a strong influence of squeeze film effects. The difference between calculated and fitted torques could be explained by the RC charging.

Finally, the flexible rotor coupled to a gear train demonstrated for the first time the ability of an electrostatic micromotor to drive a (micro) load.

6.7 Final words

The motor process compatibility with a control circuit, one ubiquitous goal of the integration of a transducer, seems better suited to the electroplating than to the polysilicon process, for two reasons. First, electroplating does not require significantly high processing temperatures susceptible to influence the circuit parameters. Second, LPCVD polysilicon-based micromotors cannot be easily connected directly to a micromechanism because of too small sizes.

Harmonic wobble micromotors reveal to be more successful than synchronous, direct-drive stepper motors. Friction is used instead of being eliminated, which is not a very natural reflex in rotary mechanics. The combination of electrostatic attraction and friction-based

mechanics is very interesting for high torque and low speed applications. High speed and low torques still need good lubricants and very precise bearings.

The vertically wobbling, 2 mm diameter rotor motors seem to be good candidates for watch applications. Their speed, which is steady, is directly proportional to the applied frequency. The wear conditions are favorable and the motors can be operated in ambient air, as tested. To further assess the wear issue, in case of watch applications, long-time tests (over years !) should be performed. In future, a speed control system should be added, maybe by using capacitive readout of the position. The ground contact should be applied to the rotor with a flexible brush to insure a 100% functionality.

References

abb M. Abbasi, T. Johansson and R.A. Normann, *Silicon-carbide-enhanced thermomigration*, J. Appl. Phys. 72 (5), 1 sept. 1992, pp.1846-1851.

and K.M. Anderson and J.E. Colgate, *A model of the attachment/detachment cycle of electrostatic micro actuators*, DSC-Vol.32, Micromechanical Sensors, Actuators and Systems, ASME, 1991, pp. 255-268.

arm W.E. Armstrong and D.L. Tolliver, *A scanning electron microscope investigation of glass flow in MOS integrated circuit fabrication*, Journal of the electrochemical society vol. 121, 2, 1974, pp. 307-310.

arq Ph. Arquint, B. Bechler, A. Cogoli, N.F. de Rooij, V. Gass, F.K. Gmuender, M.-T. Ivorra, S. Jeanneret, G. Lorenzi, P.-A. Maeusli, B. van der Schoot and I. Walter, *Microsystem technology for biological experiments in space; development of a miniature bioreactor*, Proc. IEEE 7th Int. Conf. on Solid-State Sensors and Actuators (Transducers'93), Yokohama, Japan, June 7-10, 1993, pp. 921-923.

aue W. Auer and G. Ruff, *A high resolution stepper motor*, Proc. 1st Eur. Space Mechanisms and Tribology Symp. (ESA SP-196), Neuchâtel, Switzerland, Oct. 12-14, 1983, pp. 193-196.

bar1 S.F. Bart, T.A. Lober, R.T. Howe, J.H. Lang and M.F. Schlecht, *Design considerations for micromachined electric actuators*, Sensors and Actuators, 14, 1988, pp. 269-292.

bar2 S.F. Bart, M. Mehregany, L.S. Tavrow and J.H. Lang, *Electric Micromotor Dynamics*, IEEE Transactions on electron devices, vol.39, no.3, march 1992, pp. 566-575.

beu C. Beuret, G.-A. Racine, J. Gobet, R. Luthier and N.F. de Rooij, *Micro fabrication of 3D multidirectional inclined structures by UV lithography and electroplating*, Proc. IEEE 7th Ann. Int. Workshop on Micro Electro Mech. Syst. (MEMS'94), Oiso, Japan, Jan. 25-28, 1994, pp.81-85.

bor E. Bornand, L. Paratte, G.-A. Racine et N.F. de Rooij, *Micromoteurs électrostatiques: développements récents et perspectives d'utilisation en horlogerie*, Actes du IVe Congrès Européen de Chronométrie (CEC'92), Lausanne, CH, 29-30 oct. 1992, pp. 45-48.

bra V.V. Brailovskii, N.M. Fushtei, A.R. Shelyag and O.T. Tkachenko, *Measurement of mechanical displacements by a capacitance sensor*, Izmeritel'naya Tekhnika 4, april 1988, pp. 20-21.

bre K.-H. Brenner, M. Kufner, S. Kufner, J. Moisel, A. Müller, S. Sinzinger, M. Testorf, J. Göttert and J. Mohr, *Application of three-dimensional micro-optical components formed by lithography, electroforming and plastic molding*, Applied Optics, vol. 32, no. 32, 10 nov. 1993, pp. 6464-6469.

dak T.W. Dakin, G. Luxa, G. Oppermann, J. Vigreux, G. Wind and H. Winkelnkemper, *Breakdown of gases in uniform fields - Paschen curves for nitrogen, air and sulfur hexafluoride*, Electra 32, 1974, pp. 61-82.

dan W. Daniau and S. Ballandras, *Metallic microdevices fabricated by deep-etch UV lithography*, Materials Science and Engineering, A 160, 1993, pp. L5-L8.

dec M. Declerc, M. Schubert and F. Clément, *5V to 75V CMOS output interface circuits*, Int. Solid-State Circuits Conference, vol. 36, 1993.

duf R. Duffait et P. Minotti, *Moteur piézo-électrique: perspectives de miniaturisation*, Actes du IVe Congrès Européen de Chronométrie (CEC'92), Lausanne, CH, 29-30 oct. 1992, pp. 49-52.

eng G. Engelmann, O. Ehrmann, J. Simon, H. Reichl, *Fabrication of high depth-to-width aspect ratio microstructures*, Proc. IEEE 5th Ann. Int. Workshop on Micro Electro Mech. Syst. (MEMS'92), Travemünde, Germany, feb. 4-7, 1992, pp. 93-98.

fan L.-S. Fan, Y.-C. Tai and R.S. Muller, *Integrated movable micromechanical structures for sensors and actuators*, IEEE Trans. on electron devices, vol. 35, no 6, 1988, pp. 724-730.

fav P. Favrat, L. Paratte, H. Ballan, M. Declerc and N.F. de Rooij, *A 1.5 V supplied, CMOS ASIC for the actuation of an electrostatic micromotor*, Proc. IEEE 9th Ann. Int. Workshop on Micro Electro Mechanical Systems (MEMS'96), San Diego, California, USA, February 11-15, 1996, pp. 25-31.

fis T.E. Fischer and H. Tomizawa, *Interaction of tribochemistry and microfracture in the friction and wear of silicon nitride*, Wear, 105, 1985, pp. 29-45.

fra A. B. Frazier and M.G. Allen, *Metallic microstructures fabricated using photosensitive polyimide electroplating molds*, J. Microelectromech. Syst., vol.2, no.2, June 1993, pp. 87-94.

gab1 K.J. Gabriel and W.S.N. Trimmer, *Micro-electrostatic motor*, European patent no 0 265 118 A1, filed 7th oct 1987.

gab2 K.J. Gabriel, F. Behi, R. Mahadevan, *In situ friction and wear measurements in integrated polysilicon mechanisms*, Sensors and Actuators, A21-A23, 1990, pp. 184-188.

gob J. Gobet, F. Cardot, J. Bergqvist and F. Rudolf, *Electrodeposition of 3D microstructures on silicon*, J. Micromech. Microeng. 3, 1993, pp. 123-130.

guc0 H. Guckel, D.K. Showers, D.W. Burns, C.R. Rutigliano and C.G. Nesler, *Deposition techniques and properties of strain compensated LPCVD silicon nitride films*, Proc. IEEE Conf. on Solid State Sensors and Actuators, Hilton Head Island, South Carolina, June, 1986.

guc1 H. Guckel, D.W. Burns, H.A.C. Tilmans, D.W. DeRoo and C.R. Rutigliano, *Mechanical properties of fine grained polysilicon: the repeatability issue*, Proc. IEEE Conf. on Solid State Sensors and Actuators, Hilton Head Island, South Carolina, June, 1988, pp. 96-99.

guc2 H. Guckel, J.J. Sniegowsky and T.R. Christenson, *Advances in processing techniques for silicon micromechanical devices with smooth surfaces*, Proc. IEEE 2nd Ann. Int. Workshop on Micro Electro Mech. Syst. (MEMS'89), Salt lake City, Utah, feb. 20-22, 1989, pp. 71-75.

guc3 H. Guckel, T.R. Christenson, K.J. Skrobis, J. Klein and M. Karnowsky, *Design and testing of planar magnetic micromotors fabricated by deep x-ray lithography and electroplating*, Proc. IEEE 7th Int. Conf. on Solid-State Sensors and Actuators (Transducers'93), Yokohama, Japan, June 7-10, 1993, pp. 76-79.

guc4 H. Guckel, T.R. Christenson and K.J. Skrobis, *Metal micromechanisms via deep x-ray lithography, electroplating and assembly*, J. Micromech. Microeng. 2, 1992, pp. 225-228.

haz G. Hazelrigg, *Small machines, large opportunities: a report on the emerging field of microdynamics*, NSF report of the workshop on Microelectromechanical systems research, 1987-1988, 30 pages.

hos H. Hosaka, H. Kuwano, and K. Yanagisawa, *Electromagnetic microrelays: concepts and fundamental characteristics*, Sensors and Actuators A. 40, 1994, pp. 41-47.

how R.T. Howe, R.S. Muller, K.J. Gabriel and W.S.N. Trimmer, *Silicon micromechanics: sensors and actuators on a chip*, IEEE Spectrum, July 1990, pp. 29-35.

ish H. Ishigaki, I. Kawaguchi, M. Iwasa and Y. Toibana, *Friction and wear of hot pressed silicon nitride and other ceramics*, Journal of tribology, vol. 108, 1986, pp. 514-521.

jac S.C. Jacobsen, R.H. Price, J.E. Wood, T.H. Rytting and M. Rafaelof, *The wobble motor: an electrostatic, planetary-armature microactuator*, Proc. IEEE 2nd Ann. Int. Workshop on Micro Electro Mech. Syst. (MEMS'89), Salt lake City, Utah, feb. 20-22, 1989, pp. 17-24.

jef O. Jefimenko, *Franklin's electric motors*, AJP vol. 39, oct. 1971, pp. 1139-1140.

juf M. Jufer, *Transducteurs électromécaniques*, Traité d'électricité de l'Ecole Polytechnique Fédérale de Lausanne, vol. IX, © 1979 éditions Giorgi, Switzerland.

kan R. Kaneko, *Microtribology related to MEMS - Concept, Measurements, Applications*, Proc. IEEE 4th Ann. Int. Workshop on Micro Electro Mech. Syst. (MEMS'91), Nara, Japan, jan. 30 - feb. 2, 1991, pp. 1-8.

kasp M. Kasper, *Electrostatic motors*, Proc. 2nd Int. Congress on Technology Transfer (Actuator'90), June 21-22, Bremen, Germany, 1990, pp. 195-198.

kasu M. Kasuga, T. Satoh, J. Hirotomi and M. Kawata, *Development of ultrasonic motor and application to silent alarm analog quartz watch*, Actes du IVe Congrès Européen de Chronométrie (CEC'92), Lausanne, CH, 29-30 oct. 1992, pp. 53-56.

kur W. Kurz, J. P. Mercier, G. Zambelli, *Introduction à la science des matériaux*, Traité des matériaux, vol. 1, Presses Polytechniques et Universitaires Romandes, 2e édition, © 1991 Lausanne, Switzerland.

lee E.-G. Lee and S.-K. Rha, *A study of the morphology and microstructure of LPCVD polysilicon*, J. Mat. Sc. vol. 2, 1993, pp. 6279-6284.

ler Ph. Lerch, B. Romanovicz, Ph. Renaud, L.Paratte and N.F. de Rooij, *Numerical simulations of planar electrostatic wobble motors*, Sensors and Actuators A, 46-47, 1995, pp. 640-644.

lin1 C. Linder, *Electromechanical polysilicon structures and micromachining processes for sensors and actuator applications*, PhD Thesis, May 1993, University of Neuchâtel, Switzerland, 106 pages.

lin2 C. Linder, L. Paratte, M.-A. Grétillat, V.P. Jaecklin and N.F. de Rooij, *Surface micromachining*, J. Micromech. Microeng. 2, 1992, pp. 122-132.

lor H. Lorenz, L. Paratte, R. Luthier, N.F. de Rooij and Ph. Renaud, *Low-cost technology for multilayer electroplated parts using laminated dry film resist*, Proc. IEEE 8th. Int. Conf. on Solid-State Sensors and Actuators, and Eurosensors IX, (Transducers'95, Eurosensors IX), Stockholm, Sweden, June 25-29, 1995, pp. 569-572.

mat D. Mathieson, B. J. Robertson, U. Beerschwinger, S.J. Yang, R.L. Reuben, A.J. Addlesee, J. Spencer and R.A. Lawes, *Micro torque measurements for a prototype turbine*, J. Micromech. Microeng. 4, 1994, pp. 129-139.

meh1 M. Mehregany, K.J. Gabriel, W.S.N. Trimmer, *Integrated fabrication of polysilicon mechanisms*, IEEE trans. on electron devices, vol. 35, no. 6, 1988, pp. 719-723.

meh2 M. Mehregany, S.F. Bart, L.S. Tavrow, J.H. Lang, S.D. Senturia and M.F. Schlecht, *A study of three microfabricated variable capacitance motors*, Sensors and Actuators A, 21-23, 1990, pp. 173-179.

meh3 M. Mehregany, P. Nagarkar, S.D. Senturia and J.H. Lang, *Operation of microfabricated harmonic and ordinary side-drive motors*, Proc. IEEE 3rd Ann. Int. Workshop on Micro Electro Mech. Syst. (MEMS'90), Napa Valley, California, feb. 11-14, 1990, pp. 1-8.

meh4 M. Mehregany, S.D. Senturia and J.H. Lang, *Friction and wear in microfabricated harmonic side-drive motors*, Proc. IEEE Conf. on Solid State Sensors and Actuators, Hilton Head Island, South Carolina, June 4-7, 1990, pp. 17-22.

mik Y. Mikuriya, K. Matsuzaki, T Matsuo, *Fabrication and evaluation of micromotors*, IARP'92 Conf., Karlsruhe, Germany, 1992.

mos2 *Microslide ® - Revêtement lubrifiant de MoS_2*, Specification sheets, Vilab AG, Bern, and CSEM S.A., Neuchâtel, Switzerland.

mul R.S. Muller, L.-S. Fan and Y.-C. Tai, *Micromechanical elements and methods for their fabrication*, US patent # 4 740 410, filed 28th may 1987.

nat H.C. Nathanson, W.E. Newell, R.A. Wickstrom and J.R. Davis jnr, The resonant gate transistor, IEEE trans. on electron devices, vol. 14, no. 3, march 1967.

par1 L. Paratte, G.-A. Racine and N.F. de Rooij, *Design of an integrated electrostatic stepper motor with axial field*, Sensors and Actuators A, 25-27, 1991, pp. 597-603.

par2 L. Paratte, G.-A. Racine, N.F. de Rooij and E. Bornand, *A novel comb-drive electrostatic stepper motor*, Proc. IEEE 6th Int. Conf. on Solid-State Sensors and Actuators (Transducers'91), San Francisco, California, June 23-27, 1991, pp. 886-889.

par3 L. Paratte, G.-A. Racine, N.F. de Rooij and E. Bornand, *A rigid ring electrostatic harmonic wobble motor with axial field*, Proc. IEEE 6th Int. Conf. on Solid-State Sensors and Actuators (Transducers'91), San Francisco, California, June 23-27, 1991, pp. 890-893.

par4 L. Paratte and N.F. de Rooij, *Electrodeposited electrostatic wobble motors on silicon for wristwatch applications*, Proc. IEEE 7th Int. Conf. on Solid-State Sensors and Actuators (Transducers'93), Yokohama, Japan, June 7-10, 1993, pp. 4-5.

par5 L. Paratte, H. Lorenz, R. Luthier, R. Clavel and N.F. de Rooij, *Miniature gear reduction unit driven by a silicon electrostatic wobble motor*, Proc. IEEE 7th Ann. Int. Workshop on Micro Electro Mech. Syst. (MEMS'94), Oiso, Japan, Jan. 25-28, 1994, pp. 119-123.

par6 L. Paratte and N.F. de Rooij, *Electrodeposited electrostatic rigid-rotor wobble motors on silicon*, Sensors and Actuators A, 43, 1994, pp. 371-377.

par7 L. Paratte, *Electrostatic micromotor*, US patent # 5 191 251, inventor: L. Paratte, assignee: Asulab S.A. (CH), filed March 2, 1993.

pas F. Paschen, *Ueber die zum Funkenuebergang in luft, Wasserstoff und Kohlensaeure bei verschiedenen erforderliche Potentialdifferenz*, Ann. Phys., 37, 1889, pp. 69-96.

rac G.-A. Racine, R. Luthier and N.F. de Rooij, *Hybrid ultrasonic micromachined motors*, Proc. IEEE 6th Ann. Int. Workshop on Micro Electro Mech. Syst. (MEMS'93), Fort Lauderdale, Florida, Feb.7-10, 1993, pp. 128-132.

roa R.J. Roark and W.C. Young, *Formulas for Stress and Strain*, Engineering Mechanics Series, ed. MacGraw-Hill, ©1976, 5th edition 1986.

ros J. Rossel, *Physique générale*, Bibliothèque scientifique vol 36, éd. du Griffon, Neuchâtel, CH, © 1960, 3ème édition 1970.

sek E. I. Sekimoto, H. Yoshihara and T. Ohkubo, *Silicon nitride single-layer X-ray mask*, J. Vac. Sci. Technol., 21, 1982, pp. 1017-1021.

siv D. Sivoukhine, *Cours de Physique Générale - Mécanique*, éd. MIR, Moscou, 1982, tome.I, pp. 250-251.

sze1 S.M. Sze, *Semiconductor Devices - Physics and Technology*, ed. John Wiley & Sons, ©1985.

sze2 S.M. Sze, *VLSI Technology*, ed. Mc Graw-Hill, © 1988, 2nd edition.

tai1 Y.-C. Tai, L.-S. Fan and R.S. Muller, *IC-processed micro-motors: design, technology and testing*, Proc. IEEE 2nd Ann. Int. Workshop on Micro Electro Mech. Syst. (MEMS'89), Salt lake City, Utah, feb. 20-22, 1989, pp. 1-6.

tai2 Y.-C. Tai and R.S. Muller, *Frictional study of IC-processed micromotors*, Sensors and Actuators, A21-A23, 1990, pp. 180-183.

tan W.C. Tang, M.G. Lim and R.T. Howe, *Electrostatically balanced comb drive for controlled levitation*, Proc. IEEE Conf. on Solid State Sensors and Actuators, Hilton Head Island, South Carolina, June 4-7, 1990, pp. 23-27.

tav1 L.S. Tavrow, S.F. Bart, J.H. Lang and M.F. Schlecht, *A LOCOS process for an electrostatic microfabricated motor*, Sensors and Actuators, A21-A23, 1990, pp. 893-898.

tav2 L. Tavrow, *A LOCOS-Based Microfabricated Radial-Gap Electric Motor*, PhD Thesis, Feb. 1991, © Massachusetts Institute of Technology 1991, USA, 204 pages.

tri1 W.S.N. Trimmer and K.J. Gabriel, *Design considerations for a practical electrostatic micromotor*, Sensors and Actuators, 11, 1987, pp. 189-206.

tri2 W.S.N. Trimmer, *Microrobots and micromechanical systems*, Sensors and Actuators, 19, 1989, pp. 267-287.

vat O. Vatel, Ph. Dumas, F. Chollet, F. Salvan and E. Andre, *Roughness assessment of polysilicon using power spectral density*, Jpn. J. Appl. Phys. Vol. 32, 1993, pp. 5671-5674.

vui R. Vuilleumier, A.-E. Perret, F. Porret and P. Weiss, *Novel electromechanical microshutter display device*, Proc. 4th Display Research Conf, Eurodisplay'84, sept. 18-20, 1984, Paris, F, pp. 41-44.

zar H. Zarrad, P. Cléchet, M. Belin, C. Martelet et N. Jaffrezic-Renault, *The use of long chain molecules for the lubrication of micromechanisms*, Digest of the MicroMechanics Europe Workshop (MME'93), Sept. 7-8, 1993, Neuchâtel, Switzerland, pp. 189-193.

Acknowledgments

I want to express my best thanks to all the nice persons who contributed to this challenging and motivating work:

- Prof. N. F. de Rooij, for offering me the privilege to explore this innovative subject in the frame of a thesis, and for his continuous encouragement and interest,
- Dr. G.-A. Racine, for getting me started in the technology jungle, for his substantial help along the whole project, for his patience to listen to all my complains, for inviting me to a Raclette evening full of laughter,
- Dr. E. Saurer, Dr. R. Luthier from Asulab S.A.; Dr. R. Vuilleumier, Dr. J. Gobet from CSEM; Prof. R. Clavel, Prof. Ph. Renaud, Dr. Ph. Lerch, B. Romanowicz from the Institute of Microtechnology of the EPFL, for helpful collaboration, enthusiastic and constructive discussions and for sharing time in the indispensable work meetings,
- Prof. M. Declerc, P. Favrat and H. Ballan from the Electronics Laboratories of the EPFL (EPFL-LEG/EL), for the excellent and fruitful collaboration after this thesis, for the integration of their miniature CMOS ASIC aside of the Nickel wobble motor [fav], a work still ongoing,
- Dr. E. Bornand from Asulab S.A., for his guidance and devotion, for kindly agreeing to be co-examiner of the thesis, for lots of supper evenings with tasty wines, and for his friendship,
- G. Mondin, J.-D. Cretin from Microsens S.A.; B. Vaucher from the Microcomputing Laboratory of the EPFL for assistance and help in small routine details that typically make things important,
- R. Froidevaux and R. Frossard from Asulab S.A.; J.-J. Born from ETA S.A., who, with a unique mixture of enthusiasm and watchmaker skills, constructed the minute gear reduction unit of the flexible rotor wobble motor,
- M. Maillat from the Tribology lab of CSEM S.A., for assistance in the friction measurements, and for putting the necessary equipment at our disposal,
- B. Krebs and F. Jan from Photronics S.A., for the masks fabrication and help in this field,
- Dr. Ch. Linder, for showing freely everything he knew about surface micromachining of silicon, whenever I asked for, and for sharing curry dinners,
- Dr. L.-S. Fan from IBM Almaden, USA, and Prof. H. Hügli (IMT) who kindly accepted to be co-examiners of the thesis,
- Dr. Ph. Arquint, for the unforgettable moments and discussions we had in the office, namely the squetches planning,

- S. Jenny, S. Jeanneret and P.-A. Clerc for their constant disposability and zero-default technical help, and to make me understand how some technically impossible things I proposed could nevertheless become reality under certain conditions,

- S. Pochon, for her friendship, the coffee chats and, of course, for the wire bonding,

- Dr. J. Beiner from the technical school in Le Locle, for giving me a decisive push in maths,

- C. Marxer, for helping me to set up the optical torque measurement system, and for helpful discussions and debates about permanent polarization,

- H. Lorenz from the EPFL, for his excellent collaboration and disposability during the last four years, and for sharing spine-chilling downhill runs on snowboards,

- All present and past colleagues and friends of the IMT, for the help and for all good moments shared at the institute, in the labs, in the corridors, on squash courts, in all possible places.

This work was supported by the Committee for the Promotion for Applied Scientific Research, Switzerland (CERS), and by the Swiss Partnership for Micromechanics on Silicon (M^2S^2).

Biography

Lionel Paratte was born in February 28, 1963, in Biel, Switzerland. He received his M.Sc. degree in microtechnology in 1987 from the Swiss Federal Institute of Technology in Lausanne, Switzerland (EPFL). His master work dealt with the installation of a computerized measurement set-up for pH- Ion Sensitive Field-Effect Transistors (pH-ISFETs), at the Sensors, Actuators and Microsystems Laboratory of the Institute of Microtechnology (IMT, group of Prof. de Rooij) of the University of Neuchâtel, Switzerland.

From 1987 to 1989, he was employed by the European Space Agency Technical Center (ESTEC) in the Netherlands, in the Space Mechanisms Section. There he worked on the development of electrically motorized satellite mechanisms, the design and testing of a mechanical end effector engineering model for fixation of experiments racks aboard Spacelab, and breadboard testing of magnetic suspensions for gyroscopes and flywheels. General activities also comprised tribology and electronics.

In 1989, he joined the group of Prof. de Rooij at the IMT of the University of Neuchâtel, as teaching and research assistant for the conception and development of electrostatic micromotors based on silicon technology. In close collaboration with Asulab S.A., the R&D laboratories of the SMH group, he invented and patented the electrostatic, vertically wobbling micromotor (1993), and participated to the emergence of microlithographic fabrication of metallic microparts on silicon ("poor man's LIGA"). He was also involved in microfabrication teaching courses given to industry, organized by the Swiss Foundation for Microtechnology Research (FSRM).